2nd of 3 files

Chapters 5 to 7

STUDIES OF THE MAGNETIC PROPERTIES AND MICROSTRUCTURES OF TWO RARE EARTH-TRANSITION METAL TYPE MAGNETIC ALLOYS

By
Tony Bailey

A thesis submitted for the degree of
Doctor of Philosophy

Department of Metallurgy and Materials,
Faculty of Science and Engineering,
University of Birmingham.
August 1985

CHAPTER FIVE

PERMANENT MAGNETS BASED ON AN ALLOY OF Nd-Fe-B

5.1 Introduction

The development of magnet alloys with magnetic properties equal to, or greater than the Sm-Co-type magnets, and using cheaper alloy components is an area of intense research. The announcement by Sumitomo Special Metals Co. in Japan of an alloy based on Nd-Fe-B with improved magnetic properties, has paved the way for more research and part of the present investigation has been spurred on by this development.

This chapter discusses the development of this alloy, the crystal structure and the magnetic properties. A short section is also included on the production of sintered magnets from Nd-Fe-B.

5.2 The Development of Alloys Based on Nd-Fe-B

Robinson (ref. 79) has looked at the general historical development of the permanent magnet alloys based on Nd-Fe-B. As discussed earlier, previously the materials that had the highest values of coercivity and energy product were compounds based on Sm-Co. However, any volume use of Sm-Co-type magnets has been limited by the relatively high price of Sm and Co when compared with the ferrite magnets.

The addition of rare earths to transition metals such as iron or cobalt can increase the magnetocrystalline anisotropy energy without unacceptably reducing the high magnetization through dilution of the magnetic moments of the transition metal.

Early studies had shown that the magnetic properties of binary neodymium-iron compounds were rather unimpressive (ref. 80). However, Croat (ref. 81) described experiments on melt spun amorphous neodymium-iron materials which had intrinsic coercivities of about 7.5 KOe.

With no long range crystal structure and hence no anisotropy, amorphous materials would not seem candidates for high performance permanent magnets. However, amorphous materials provide a starting point from which to prepare crystalline materials or metastable phases composed of very fine crystallites or grains by subsequent annealing after melt spinning.

Croat's interpretation of his results (ref. 81) was that at the correct quenching rate a magnetically active phase formed and the coercivity reached an optimum value. The particle size of the fine crystallites or clusters making up the phase was matched to the single domain size optimum. At too high a quenching rate, the magnetic properties deteriorated due to the small size of the grains.

Work by Potocky et al (ref. 82) showed the influence of a few per cent rare earth additives to iron-boron amorphous alloys. The rare earth additions altered the coercive force, Curie

temperature and amorphous-crystalline transition. Chaban et al (ref. 83) investigated the RE-Fe-B ternary compounds (RE = Sm, Gd or Nd) their results show that at 600°C a number of stable phases existed. The phases were identified as $RE_3Fe_{16}B$, $REFe_4B_4$ and RE_2FeB_3, but there were no studies undertaken of the crystal structure and the magnetic properties. The isothermal section at 400°C and 600°C produced by these workers is shown in fig. 5.1.

Stadelmaier et al (ref. 84) investigated alloys of Fe-Pr-B, Fe-La-B and Fe-Nd-B; a stable phase was found to exist with the composition $Fe_{21}RE_3B$ (RE = rare earth) with another, unidentified phase. The crystal structure was shown to be tetragonal with an easy c-axis direction and high magnetocrystalline anisotropy. Most important was the suggestion that permanent magnets could be made from these alloys by conventional powder metallurgy and sintering techniques used in the production of "1:5" and "2:17"-type permanent magnets. In addition to this, Hadjipanayis et al (ref. 85) investigated the magnetic properties of rapidly quenched Fe-RE-M alloys (RE = La, Y, Pr, Nd, Gd and M = B, Si, Al, Ga, Ge) over a wide composition range. Again, the best magnetic properties were obtained on samples containing Pr and Nd.

The development of the Nd-Fe-B alloys finally came to a head when Sumitomo Special Metals Co. of Osaka, Japan revealed that it had produced by conventional powder metallurgical techniques, magnets from a compound based on Nd-Fe and called "Neomax". Sagawa et al (ref. 86) then published results on the new alloy. It had a composition based on $Nd_{15}Fe_{77}B_8$ and had an easy c-axis uniaxial anisotropy and an energy product of over

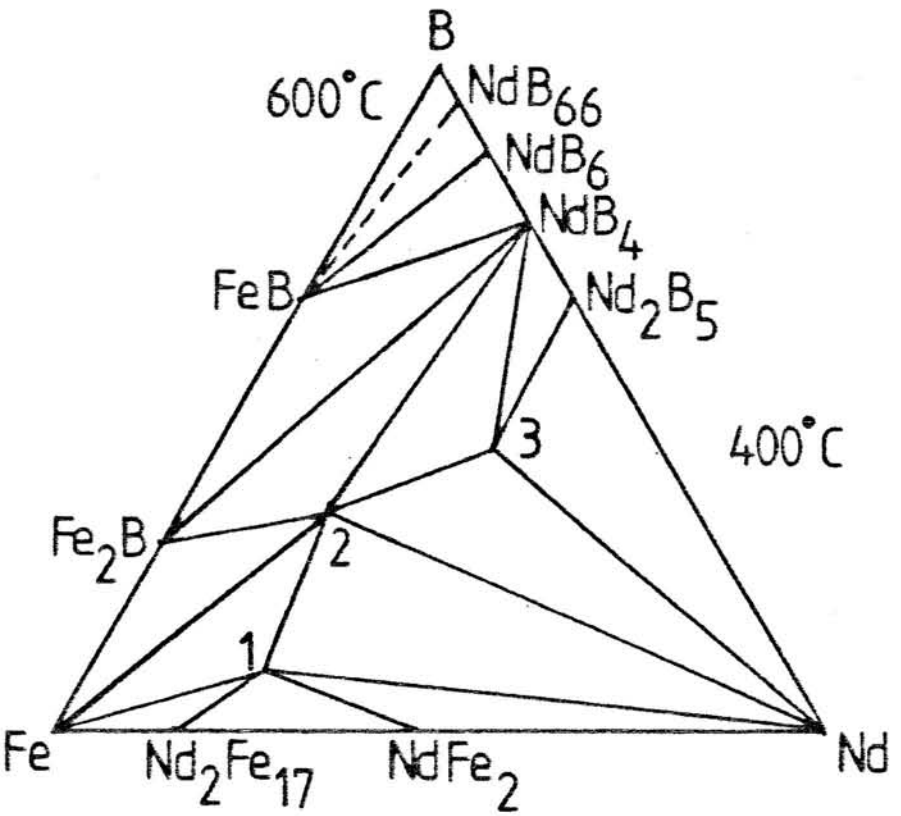

1 $Nd_3Fe_{16}B$

2 $NdFe_4B_4$

3 Nd_2FeB_3

Fig. 5.1 Isothermal section at 400°C and 600°C for the Nd-Fe-B system.

36 MGOe. This high value was attributed to the observation that the magnets were made via a powder metallurgy route and so they were anisotropic and the grains had been oriented in a magnetic field during pressing.

The main limitation of the Nd-Fe-B alloy is the low Curie temperature (about 310^{o}C), however this can be raised by the addition of several percent cobalt (ref. 86).

5.3 The Crystal Structure of Alloys Based on Nd-Fe-B

The structure of alloys based on RE-Fe-B (RE = La, Nd, Pr) has been investigated by Stadelmaier et al (ref. 84). It was considered that the magnetic phase was close to the $Fe_{21}RE_3B$ or $Fe_{47}RE_7B_2$ compositions and had a tetragonal structure with an easy c-axis alignment.

Herbst et al (ref. 87) determined the crystal structure of a $Nd_2Fe_{14}B$ ternary phase which was considered responsible for the magnetic properties and their results are shown in fig. 5.2. There are four $Nd_2Fe_{14}B$ units (68 atoms) per unit cell, from fig. 5.2 it can be seen that all the Nd and B atoms, but only four of the 56 iron atoms reside in the Z = 0 and Z = 0.5 planes. Between these, the other Fe atoms form folded, yet fully connected hexagonal nets. As shown in fig. 5.3, the B atoms occupy the centres of trigonal prisms formed by the three nearest iron atoms above and the three below the basal (Z = 0.5) plane.

The present investigation has shown the main phase in a bulk $Nd_{15}Fe_{77}B_8$ alloy to be tetragonal by X-ray diffraction and

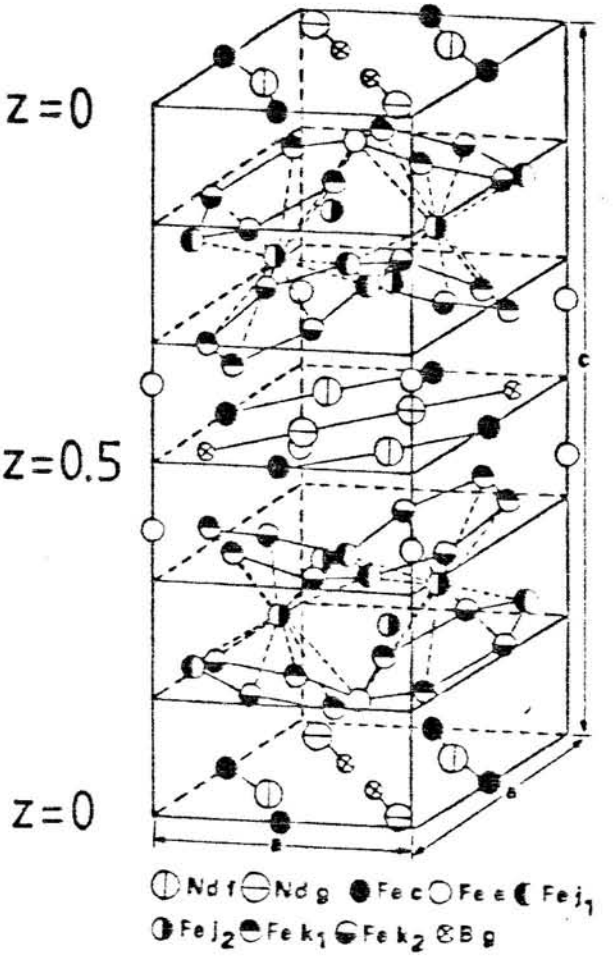

Fig. 5.2 Unit cell of $Nd_2Fe_{14}B$.

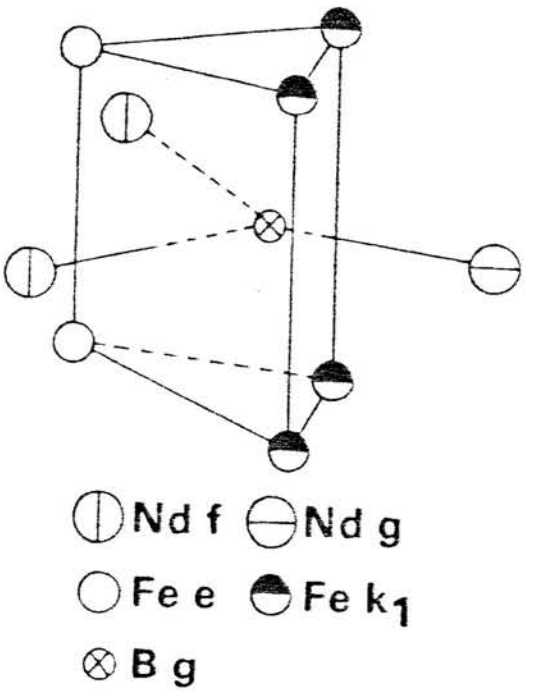

Fig. 5.3 Trigonal prism containing a boron atom in the $Nd_2Fe_{14}B$ structure.

having the composition $Nd_2Fe_{14}B$ using EDAX analysis (refs. 88,89).

5.4 The Metallurgy of the Alloys Based on Nd-Fe-B

It has been reported (ref. 90) that at 900°C the following phases were observed: $Fe_{14}Nd_2B$, γ-Fe, $Fe_{17}Nd_2$, Fe_4NdB_4 and Nd-rich liquid. The phase $Nd_3Fe_{16}B$ observed by Chaban et al (ref. 83) may well be more accurately defined as the $Nd_2Fe_{14}B$ composition. At the sintering temperature a Nd-rich liquid phase exists with the $Nd_2Fe_{14}B$ phase and the Nd-rich phase is nucleated at the grain boundaries or particle surfaces (ref. 90).

In the "as-cast" structure for alloys having greater than 15 at.% Nd and less than 6 at.% B, the phases $Nd_2Fe_{14}B$ and Nd + Fe occur, (ref. 90), it is possible that an "as-sintered" alloy consists of $Nd_2Fe_{14}B$ and a Nd-rich phase consisting of more than one phase. Ormerod (ref. 91) mentioned that an "as-sintered" Nd-Fe-B alloy consisted of:

1. Hard major tetragonal phase with 27 wt.% Nd
2. A grain boundary Nd-rich phase with 80 wt.% Nd
3. A B rich phase with 38 wt.% Nd.

The $Nd_2Fe_{14}B$ phase is reported (ref. 90) to crystallize from the melt in platelet form with rapid basal plane growth and the grains being columnar in form. The Nd-rich phase is observed as being soft due to "pull out" on polishing and a "ledge" structure is observed in unetched specimens (refs. 90,92). Stadelmaier (ref. 90) has shown the overall composition of the Nd rich phase to be about 70 at.% Nd with little B, and the

X-ray diffraction pattern is that of "double" hexagonal α-Nd.

5.5 Origin of Ferromagnetism in Nd-Fe-B

Herbst et al (ref. 87) studied an alloy of the composition $Nd_2Fe_{14}B$ using powder neutron diffraction. They determined that the moment arrangement is ferromagnetic with all Nd and Fe moments parallel to the c-axis of the tetragonal cell. Sellmyer et al (ref. 93) also reported that the net Nd moment is parallel to the Fe moments using thermomagnetic analysis. It was also considered that as Gd and Y showed only low coercivities with Fe and B then the hard magnetic properties are intimately connected with the strong magnetocrystalline anisotropy of the light rare earths (La, Pr, Nd).

Sagawa et al (ref. 86) reported that the B atoms may expand the Fe-Fe interatomic distances and/or increase the number of Fe-Fe nearest neighbours leading to high Curie temperatures compared with Nd-Fe binary compounds. Alternatively, the B atoms act to stabilize the tetragonal phase.

5.6 Coercivity Mechanisms in the Nd-Fe-B Alloys

Croat (ref. 81) investigated melt-spun Nd-Fe alloys and concluded that the maximum coercivity value of 7.45 KOe was due to the quenched alloy consisting of fine crystallites or clusters whose average particle size can be matched to the single-domain optimum. This was concluded from a correlation between the quench rate and coercivity as shown in fig. 5.4.

Croat et al (ref. 94,95) reported studies on Nd-Fe-B and

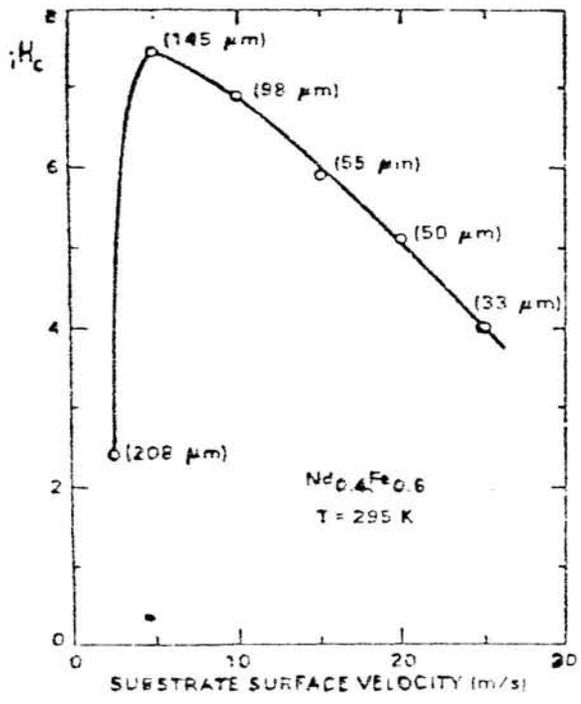

Fig. 5.4 Plot of $_iH_c$ versus melt spinning substrate velocity for a Nd-Fe alloy.

Pr-Fe-B melt-spun alloys. X-ray analysis showed roughly spherical crystallites of an equilibrium Nd-Fe-B intermetallic phase, with a grain size near to the estimated single-domain range.

Stadelmaier et al (ref. 90) reported that the Nd-rich phase present with a ϕ phase (ϕ = $Fe_{16}Nd_3B$, $Fe_{14}Nd_2B$ or $Fe_{21}Nd_3B$) was necessary for the high coercivities and the amount of Nd had to be greater than 12 at.% for this phase to occur. Their investigation also concluded that a major contribution to the coercivity was due to a single domain particle size and a lesser contribution to inclusions or defects.

This present investigation has shown that there may be some domain pinning coupled with a domain nucleation process (ref. 89) as indicated by a rise in microhardness values and a rise in intrinsic coercivity with isothermal ageing time. This process is more pronounced in the "2:17"-type alloys and has been proposed as being due to the pinning of dislocations and domain walls by coherent precipitates (refs. 66,96). Sagawa et al (ref. 86) also suggested that due to the rectangular form of the second quadrant hysteresis loop, a domain pinning mechanism was possible.

It is clear that as regards the coercivity mechanism in these alloys, more work is required at the present time, particularly in electron microscope work to study whether any coherent precipitate phases occur as in the "2:17"-type alloys.

5.7 The Effects of Alloy Composition on the Magnetic Properties of Nd-Fe-B

Sagawa et al (ref. 86) have studied the effects of boron and neodymium additions on the magnetic properties of $Nd_{15}B_xFe_{85-x}$ and $Nd_xB_8Fe_{92-x}$ alloys respectively. Their results are shown in figs. 5.5 and 5.6. After a post sintering heat treatment the coercivity was raised and the optimum magnetic properties were obtained for an alloy in the composition range 6-8 at.% B and 14-15 at.% Nd. The low melting point Nd-rich phase that occurs at this composition increases the density values due to a liquid phase sintering process. The investigation also reported that additions of 10-20 at.% Co reduce the temperature coefficient of B_r while small additions of the heavy rare earths can improve the temperature coefficient of the coercivity.

5.8 The Effects of Heat Treatment on the Magnetic Properties of Nd-Fe-B

Sagawa et al (ref. 86) have reported the effects of sintering temperature on the magnetic properties of Nd-Fe-B alloy. A wide sintering temperature range is possible to achieve the optimum magnetic properties (about 1080°C to 1140°C) this has been attributed to the presence of the low melting point Nd-rich phase occurring at grain boundaries; their results are shown in fig. 5.7.

In addition, the effects of a post sintering annealing temperature on the magnetic properties has been investigated (ref. 86) and the results are shown in fig. 5.8. This enhancement

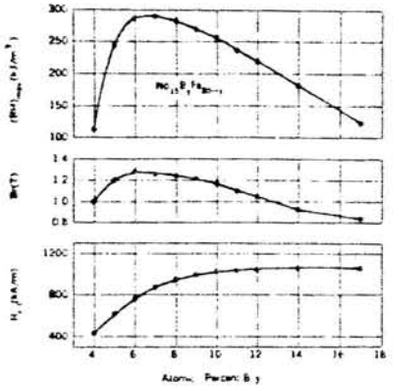

Fig. 5.5 Plots of magnetic properties versus at.% B in $Nd_{15}B_xFe_{85-x}$.

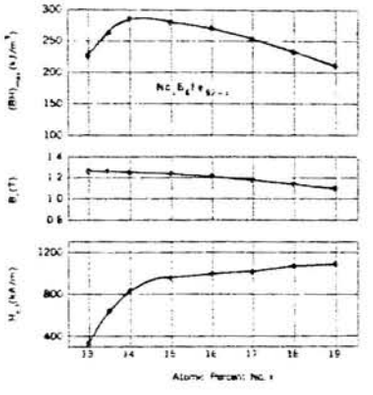

Fig. 5.6 Plots of magnetic properties versus at.% Nd in $Nd_xB_8Fe_{92-x}$.

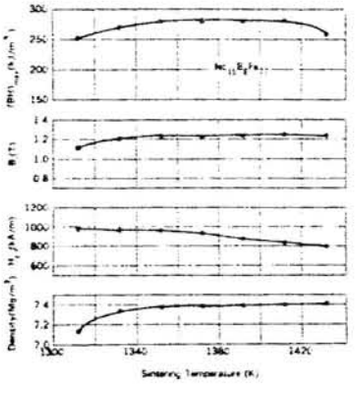

Fig. 5.7 Plots of magnetic properties versus sintering temperature for $Nd_{15}Fe_{77}B_8$.

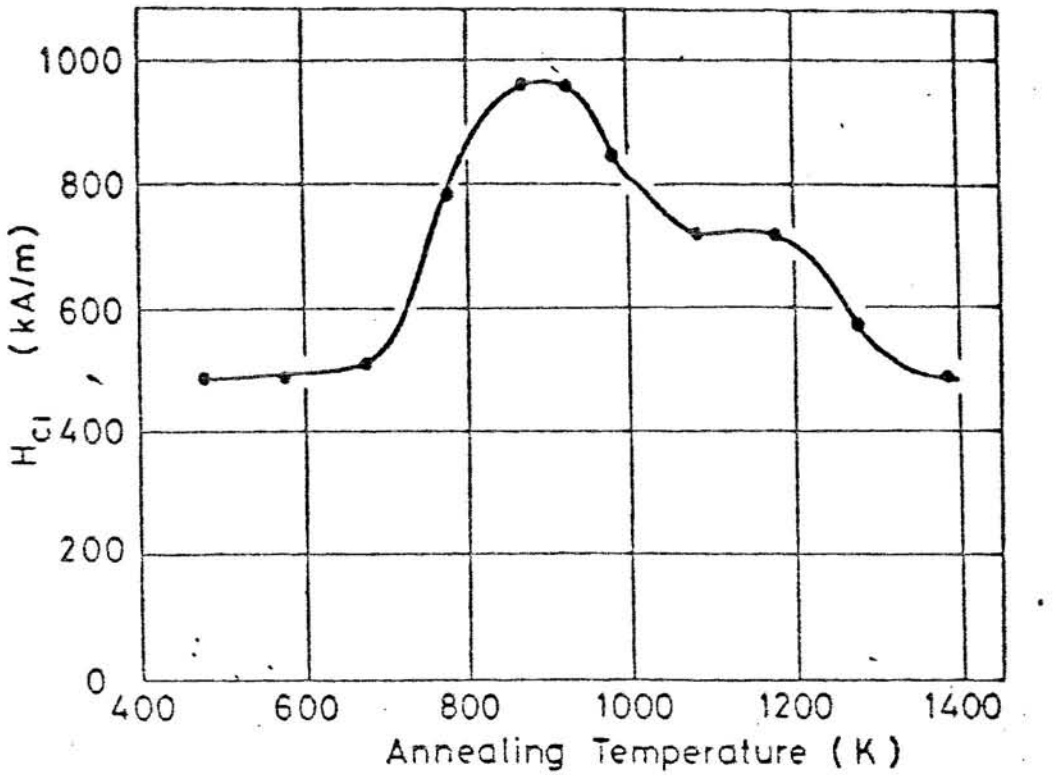

Fig. 5.8 Variation of $_{i}H_{c}$ with temperature of post sintering heat treatment for a $Nd_{15}Fe_{77}B_{8}$ magnet.

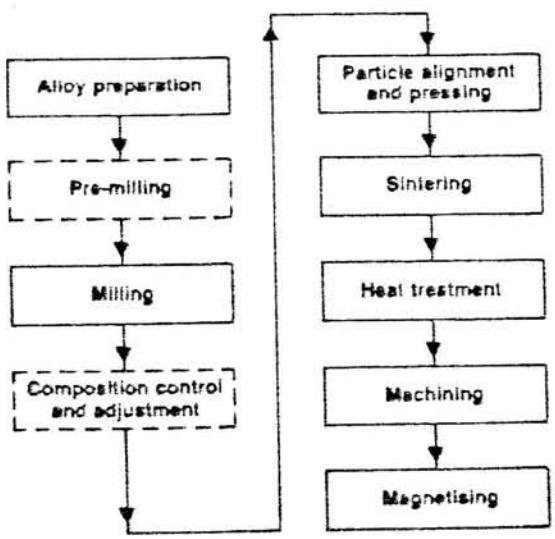

Fig. 5.9 General process steps for the production of sintered rare earth permanent magnets.

of the coercivity by annealing has been related (ref. 86) to the melting of the Nd-rich phase at the annealing temperature.

The present work has shown an increase in coercivity values with isothermal ageing time (ref. 89) and this may be related to the formation of coherent precipitates which pin domain walls as well as pinning dislocations (ref. 97).

5.9 The Powder Metallurgical Processing of Nd-Fe-B Magnets

The processing of Nd-Fe-B PM alloys can be carried out by a powder metallurgical process similar to that used for the RE-Co-TM alloys as discussed in Section 4.4.2 and is outlined in fig. 5.9. The difficulty in processing Nd-Fe-B alloys is that of oxygen pickup and this is shown in fig. 5.10 (ref. 91), where it can be seen that Nd alloy is more reactive than the Sm alloy.

A possible way of reducing oxygen pickup during ball milling is the use of a hydrogen decrepitation (HD) process to produce powder that is fine enough to use in the green compact production stage or that can be subsequently ball milled for a shorter term after a HD process. This investigation has shown that sintered magnets can be produced that have quite high intrinsic coercivities (ref. 98).

Early work has also shown that melt-spun material can be used to produce permanent magnets (ref. 81). General Motors have patented a melt-spun produced magnet using a hot pressing technique (see Chapter 8).

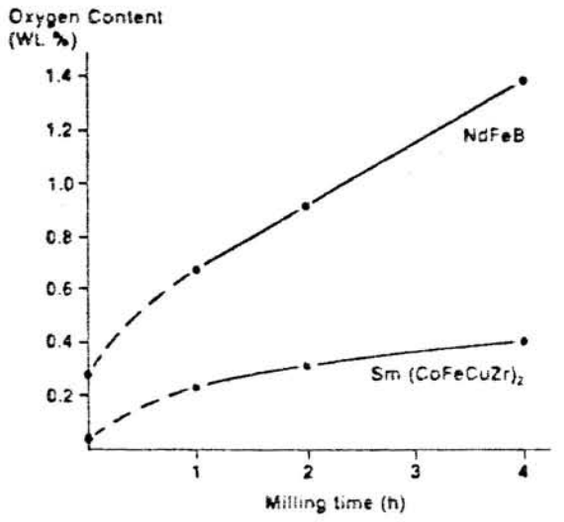

Fig. 5.10 The effect of milling time on oxygen pickup of Nd-Fe-B and $Sm(CoCuFeZr)_Z$ alloys.

5.10 Future Developments in NdFeB Permanent Magnet Materials

Ormerod (ref. 91) has indicated that an energy product of 55 MGOe should be achievable under production conditions for the Nd-Fe-B alloys.

The temperature related disadvantages can be alleviated by substituting some cobalt for iron to increase the Curie temperature. Increases in the intrinsic coercivity can be obtained by the addition of certain heavy rare earths such as Tb, Dy, or Ho (ref. 99).

The Nd-rich grain boundary eutectic phase results in some corrosion and oxidation problems, these may be solved by the addition of Co or a heavy rare earth to form a Nd-RE rich compound instead of the Nd-rich intergranular phase.

CHAPTER SIX

APPARATUS AND EXPERIMENTAL WORK

6.1 Introduction

6.1.1 Choice of Alloy Compositions

The $Sm(Co,Cu,Fe,Zr)_z$-type alloy is obtainable in a number of alloy compositions, each with different magnetic and temperature related properties. The composition chosen for this investigation is a commercial alloy used by TDK of Japan and has been featured in the literature (see for example refs. 65,69); the results from this work will add to the existing information on this alloy.

The Nd-Fe-B alloy composition chosen is the one initially announced by Sumitomo Special Metals and the one used in the general investigation by Sagawa et al (ref. 86).

6.1.2 The $Sm(Co,Cu,Fe,Zr)_z$ and Nd-Fe-B Compositions

The two alloy compositions are given in table 6.1; the amounts are given as weight % and then substitution (atomic %) compositions. The weight % values were obtained by wet chemical analyses, gravimetric analyses and atomic absorption spectroscopy.

6.1.3 Production of the Bulk Alloys

The alloys used were supplied by Rare Earth Products (A Division

TABLE 6.1 The Alloy Compositions

Alloy Type	Composition	
	weight %	substitutional
	Sm Co Cu Fe Zr	
$Sm(Co,Cu,Fe,Zr)_z$	25.5 bal 8 15 3	$Sm(Co_{0.66}Cu_{0.10}Fe_{0.22}Zr_{0.02})_{7.37}$
	Nd Fe B	
Nd-Fe-B	33.2 bal 1.3	$Nd_{15}Fe_{77}B_8$

of Johnson Matthey). "As cast" ingots of the material were prepared by adding the component metals to an alumina crucible, in such an order that the reactive metal with a lower melting point was placed at the top of the crucible so that a low melting point phase would form with the other components on heating.

The crucible was then placed in an induction coil inside a Balzers induction furnace, shown schematically in fig. 6.1. The furnace chamber was evacuated to a pressure of 10^{-3} torr and then back-filled with argon to a pressure of 100 torr before melting. The induction coil was water cooled via a vacuum tight arrangement and bolted on a pivoted lead-in for current and cooling water.

The total melting period, from room temperature to pouring took about 15 minutes and induction stirring ensured good homogeneity. Any Sm or Nd loss by evaporation or oxidation was allowed for by adding between 1 and 4 wt.% additional Sm or Nd to the crucible before being placed in the induction coil. After the melting operation, the melt was poured into a water-cooled copper mould, positioned inside the chamber near to the pouring lip of the crucible. The ingot was then allowed to cool for ½ hour before removal.

6.2 Bulk Alloy Studies

6.2.1 Studies on the $Sm(Co,Cu,Fe,Zr)_z$ Bulk Alloy

A piece of the "as-cast" bulk material was prepared for optical metallography and scanning electron microscope (SEM) studies as detailed in Section 6.11 and 6.12 respectively.

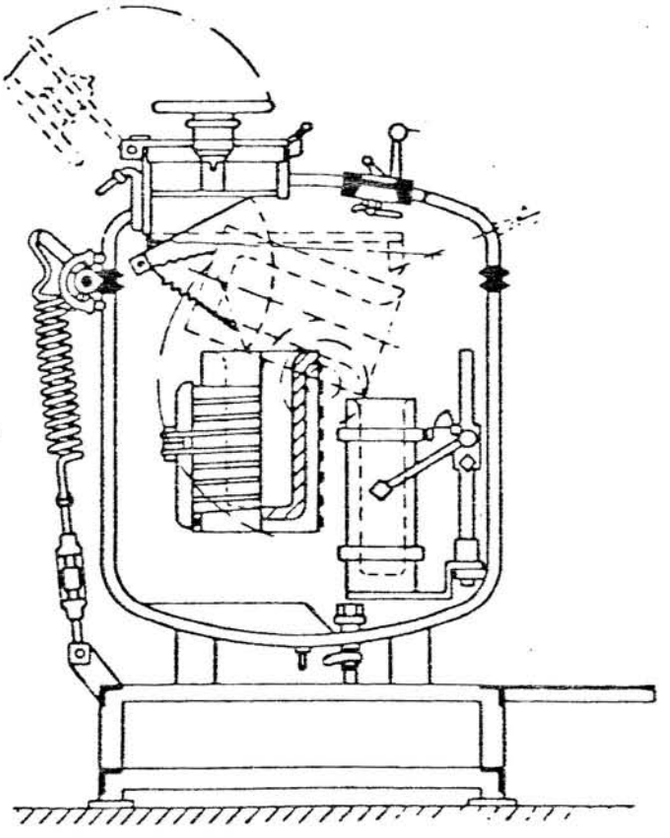

Fig. 6.1. Balzers induction vacuum furnace with rammed ceramic crucible that can be tilted for pouring into mould.

A piece of the bulk material was heat treated as follows: solid solution treated at 1170°C for one hour and then quenched in liquid argon; this specimen was prepared for optical metallography studies. Another piece of the bulk material was also solid solution treated at 1170°C for one hour and then quenched, but was then isothermally aged at 800°C for over 70 hours in ½ and one hour steps.

After each ageing step on the bulk sample the microhardness and relative resistivity were measured as detailed in Sections 6.9 and 6.10 respectively. The specimen was then prepared for optical metallography. In view of the earlier studies by Kianvash (refs. 70, 100) on alloys of similar compositions (z = 7.55 and 8.92) further detailed metallographic studies of the bulk alloy were not undertaken.

6.2.2 Studies on the Nd-Fe-B Bulk Alloy

A piece of the "as cast" material was prepared for optical metallography and SEM studies as detailed in Sections 6.11 and 6.12.

Pieces of the bulk material were also treated as follows:

(i) solid solution treated at 1100°C for one hour and then quenched in liquid argon

(ii) solid solution treated at 1100°C for one hour and then furnace cooled to room temperature

(iii) as specimen (i) but subsequently isothermally aged for up to 100 hours at 600°C

(iv) as specimen (ii) but subsequently isothermally aged for up to 100 hours at 600°C

(v) as specimen (i) but subsequently isothermally aged for up to 100 hours at 660°C.

The heat treatment preparation and procedure is detailed in Section 6.5. Specimens (iii), (iv) and (v) were each tested for their microhardness values after each ageing step. The microhardness measuring procedure is detailed in Section 6.9. All the specimens were prepared for optical metallography and SEM studies after the heat treatments.

6.3 Production of "Green" Compacts From the Bulk Alloys

6.3.1 Production of "Green" Compacts From the $Sm(Co,Cu,Fe,Zr)_z$ Alloy

A 'green' compact is the term used to describe powder that has been pressed in a die and then removed from the die. The method of production of the "green" compacts from the bulk 2:17-type alloy was developed from the procedures used in the literature (see for example refs. 65,75). The main consideration was that the conditions of each production step were maintained as consistently as possible to avoid the appearance of any anomalous results when the heat treated green compacts were investigated further.

6.3.1.a Crushing of the Bulk Alloy

The bulk alloy was supplied in a broken ingot form, consisting of lumps of about 2 cm average diameter. The surfaces of the

particles were inspected and any slag or discolouration was removed by filing or using 150 grit abrasive paper. The lumps were placed between two steel plates and then crushed by placing the plates and lumps in a "R & I L-30" 30 tonne hydraulic press. This process reduced the particle size to between 0.5 and 4 mm.

6.3.1.b Milling of the Bulk Alloy

The crushed particles were then placed in an air tight stainless steel cylinder with an inlet/outlet valve. 6.34 mm diameter stainless steel balls were added, so that the ratio of balls to material was 1:1 (by volume) and the total volume of balls and crushed particles was approximately 100 cm^3.

Zhu et al (ref. 101) used toluene as a wet ball milling medium; two low water solubility solvents were each used in an attempt at wet ball milling. The solvents were 1,1,1 trichloroethane and hexane; this produced sintered permanent magnets with negligible magnetic properties due possibly to a reaction between the Sm and the solvents. Dry ball milling under purified argon was therefore attempted and this produced magnet samples with much improved magnetic properties. The procedure for ball milling under argon is as shown below:

i. pump out the air in the stainless steel cylinder to about 10^{-2} torr

ii. add purified argon to a pressure of about 2 atmospheres

iii. seal the valve on the cylinder.

The cylinder was placed in a "Grantham" vibratory ball mill apparatus

and milled for one hour; the length of time was adequate to produce powder of approximately 5-10 μ diameter. The cylinder was then opened in air and the powder removed, brushed through a 38 μ sieve and placed in a vacuum desiccator. The length of time the powder was exposed to air was less than 5 minutes.

6.3.1.c Aligning and Pressing the Milled Alloy

The amount of powder used to produce the compact had to be of a weight such that the sintered specimen was long enough for magnetic measurements; this is discussed in Section 6.8.2.ii.

2.25 g of powder was found to be the optimum and this was placed in a die which is shown in fig. 6.2; the die end pieces ensured a closed magnetic circuit on aligning, while the non-magnetic Nimonic alloy avoided any extraneous flux lines misaligning the powder. The die inner surfaces had been previously lightly sprayed with "Gallenkamp" fluorocarbon lubricant so that the green compact could be easily removed after aligning and pressing.

The die and powder were placed between the poles of a "Newport" high current-low voltage electromagnet. A maximum field of 7.5 KOe was applied to the powder through the die end pieces. For improved alignment of the powder during pressing, a field of about 15 to 20 KOe would be desirable. One pole of the electromagnet was then unclamped and the powder was pressed to a pressure of 1.5 tonnes/cm^2; the apparatus is shown in fig. 6.3. The field was then switched off and the green compact was removed by removing the flat die end piece and pressing down on the long die end piece using the "R & I L-30" press. The pressing pressure of 1.5 T/cm^2 used ensured that

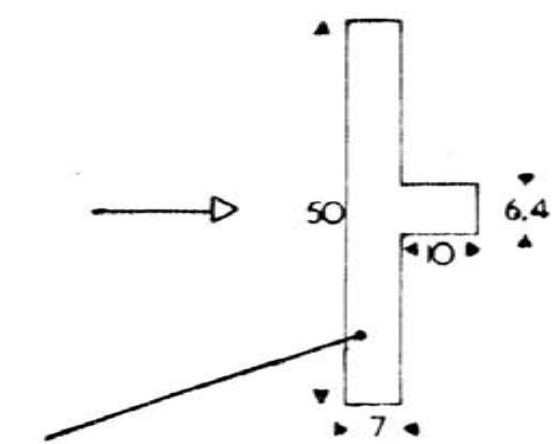

EN30B

Heat treated steel

end piece

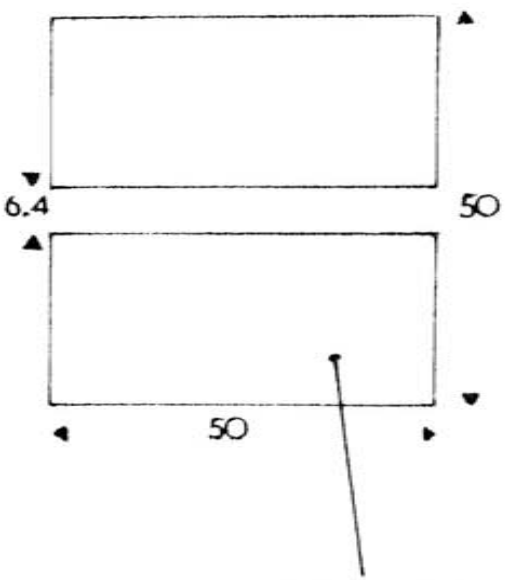

Heat treated

Nimonic 80A

Die Cylinder

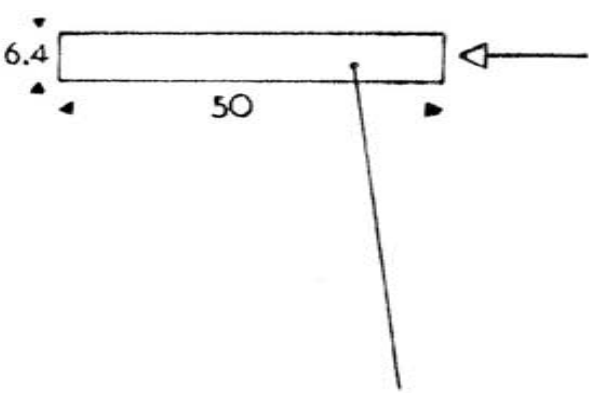

H.S.S. tool steel

die end rod.

Fig. 6.2 Die construction and Die materials (all measurements in mm).

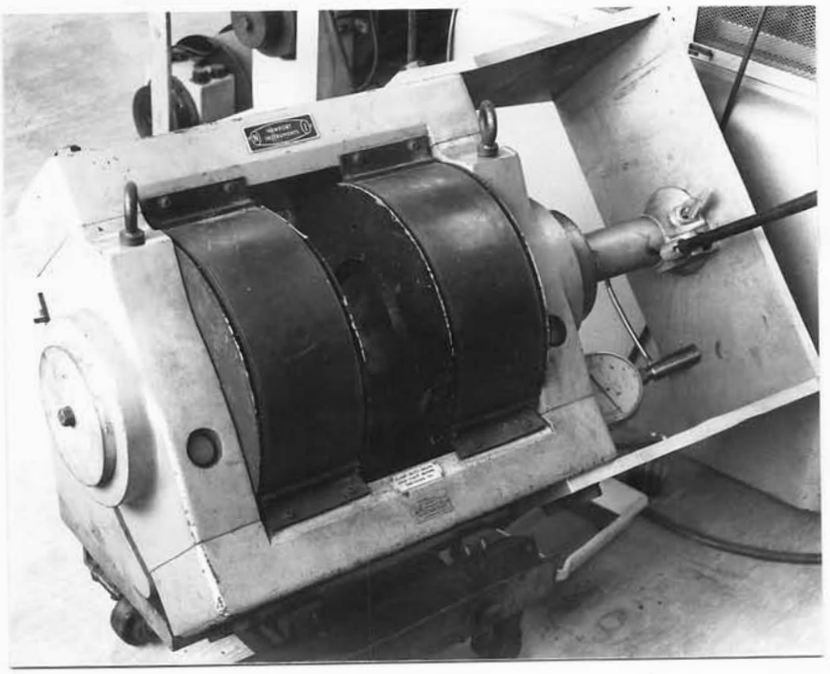

Fig. 6.3 Photograph of the aligning and pressing rig.

the green compact did not break on extrusion.

The green compact produced had little mechanical strength but held its shape when left unsupported and the compact was approximately 60% dense.

The compact was then placed in a tantalum foil "sleeve" and put in a vacuum system ready for heat treatment.

6.3.2 Production of "Green Compacts" from the Nd-Fe-B Alloy

The stages in the production of a "compact" from the Nd-Fe-B alloy were almost identical to those used for the 2:17-type alloy. The differences are listed below:

i. the material was ball milled under 1,1,1 tricholorethane, as dry ball milling caused the powder to be compacted on the stainless steel cylinder walls and removal was difficult. The solvent also had no deleterious effect on the magnetic properties unlike the 2:17 alloy. After milling for one hour the slurry was washed through a 150 μ sieve using 1,1,1 trichloroethane. The particle size produced was in the range 5-10 μ. The powder was vacuum dried in a vacuum desiccator for one hour at room temperature and the dried powder stored in a vacuum.

ii. 2.15 g of material were placed in the die prior to aligning and pressing.

iii. the powder was pressed to 2 T/cm^2.

iv. before heat treatment, any solvent residue was removed by heating the green compact to about 250^{o}C while under

a vacuum of about 3×10^{-6} torr for about $\frac{1}{2}$ hour. This procedure avoided the possibility of contamination of the compact during heat treatment.

6.4 The Use of Hydrogen Decrepitation as a Means of Powder Production

6.4.1 Introduction

Kianvash (ref. 100) and King (ref. 102) have used and investigated hydrogen decrepitation (HD) as a method of powder production. The process involves hydrogen entering into the metal lattice and forming a brittle metal hydride from which fine powders can be formed from this "hydrogen embrittlement" effect.

One of the advantages of this process is that of producing clean surfaces on the powder particles which are then in a suitable condition for stabilisation by either plastic or metal coating. In addition it has been reported that (ref. 103) the HD process resulted in less deformation during powder production than grinding resulting in a greater number of coherent precipitates in the $Sm(Co,Cu,Fe,Zr)_z$ alloy and hence giving a higher coercivity.

The investigation has also shown that the HD process can be applied to the Nd-Fe-B type alloy (ref. 98) to produce powder for sintered magnet production.

6.4.2 Use of the HD Process to Produce Powder from the $Sm(Co,Cu,Fe,Zr)_z$ Alloy

The procedure for producing powdered material via the HD process was the same as that used by Kianvash (ref. 100). The "as-received"

broken ingot alloy was placed in a small chamber with a copper O-ring seal, capable of holding up to 1000 atms. of hydrogen at up to 400°C; the chamber is shown in fig. 6.4.

A small hand operated hydraulic pump with pneumatic interface was used for the high pressure hydrogenation of the specimen; a schematic diagram of this system is shown in fig. 6.5.

The procedure for pressurising the alloy in the system is given in Appendix A. The system was pressurised to about 200 atms. at 200°C for about 12 hours. This brought about an optimum decrepitation treatment. After the HD process the material was removed from the chamber and ball milled as described in Section 6.3.1, and a green compact was produced as described in Section 6.3.1.

Before heat treatment, the green compact was heated to about 250°C in a vacuum of about 3×10^{-6} torr for about one hour. This stage was necessary as straightforward sintering of the green compact produced from HD and milled material caused the green compact to break up under the action of the escaping hydrogen.

6.4.3 Use of the HD Process to Produce Powder from the Nd-Fe-B Alloy

The apparatus used for producing powdered Nd-Fe-B material was the same as in Section 6.4.1. The Nd-Fe-B alloy was hydrogenated using two different hydrogen pressures, to investigate the effects on the magnetic properties. The two procedures are described below:

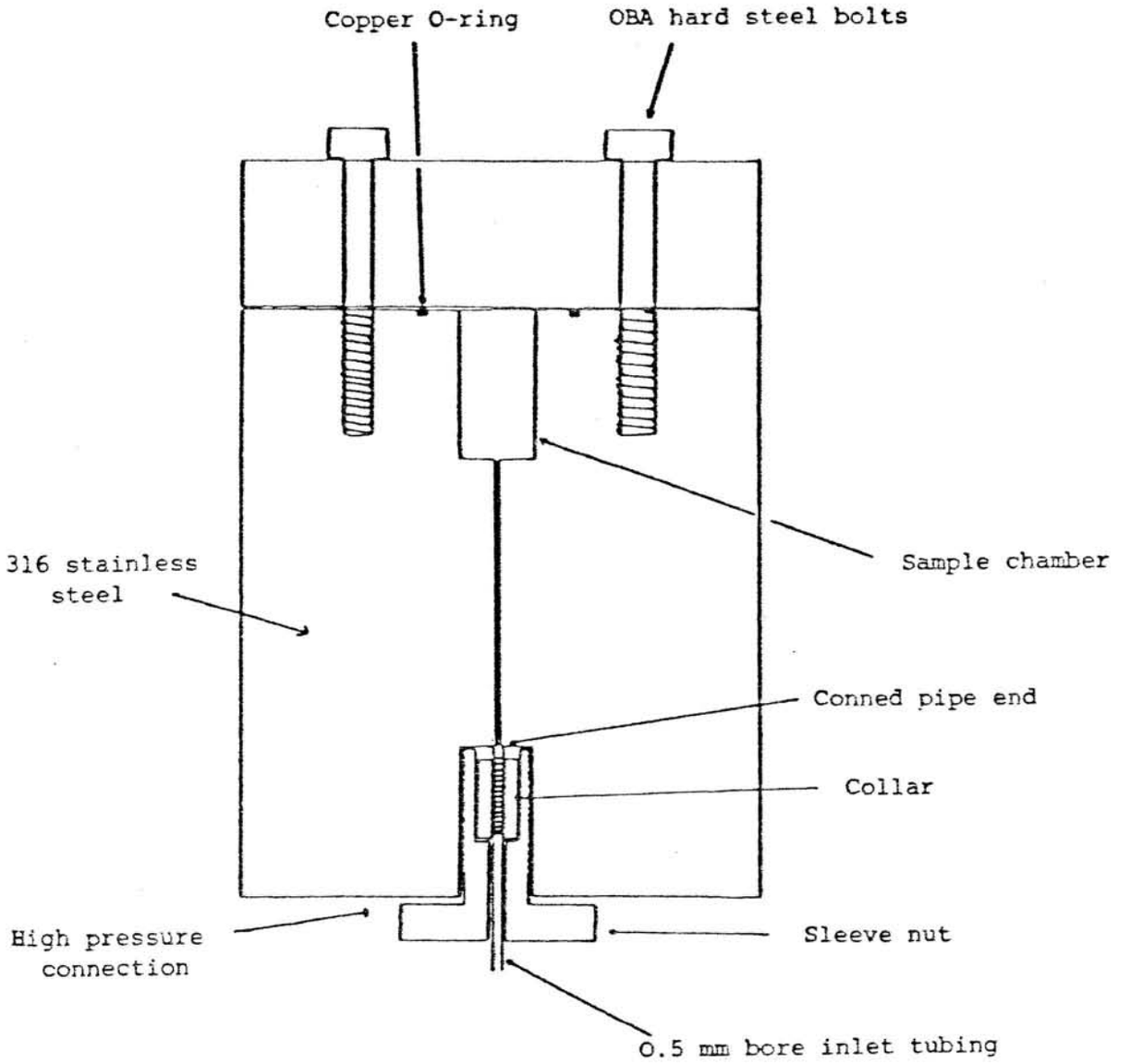

Fig. 6.4 0-400°C high pressure hydrogenation chamber.

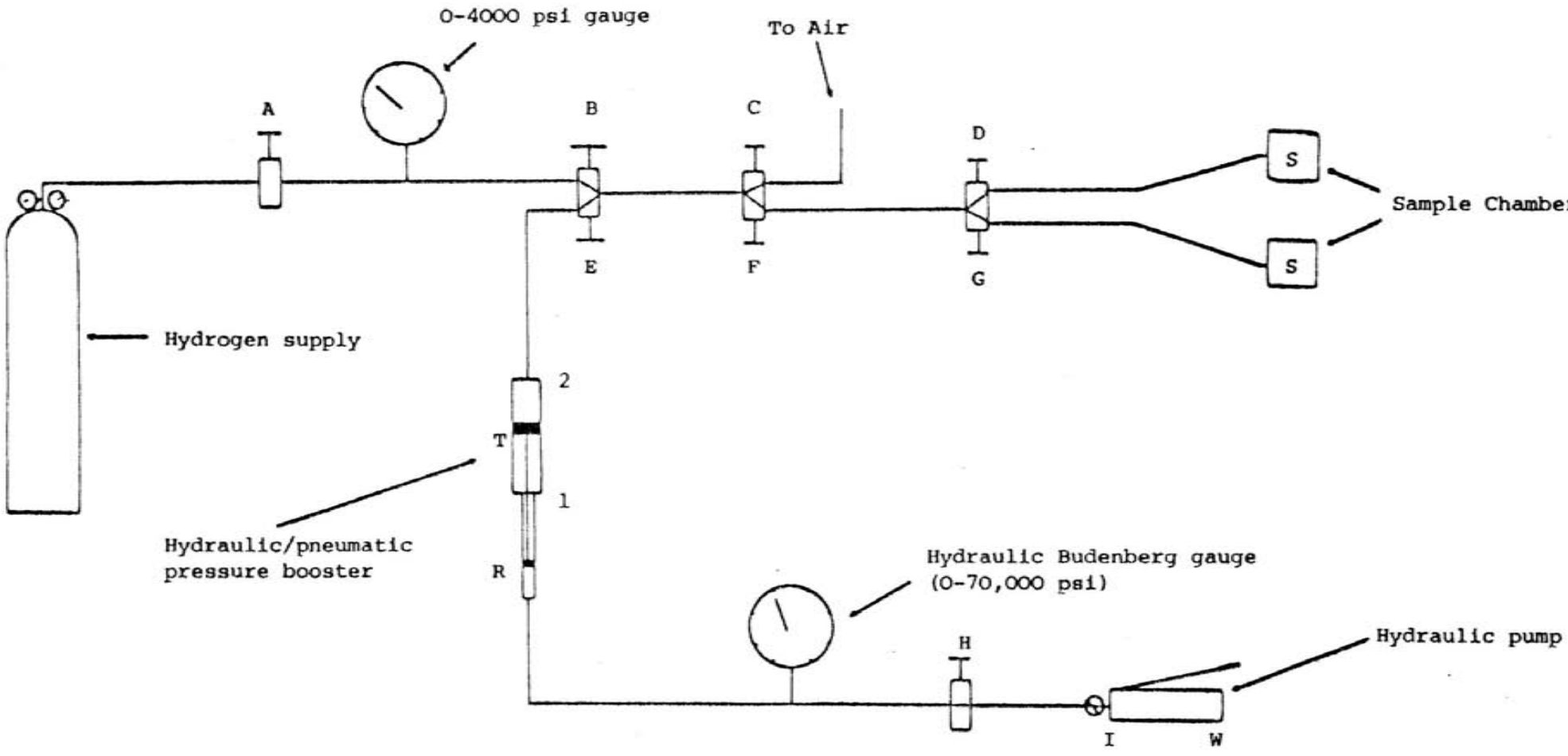

Fig. 6.5 High pressure 0-2000 atms. rig.

i. hydrogenated at about 33 atms. at room temperature for approximately two hours (until no more hydrogen was absorbed by the material, which was indicated by a constant hydrogen pressure on the Budenberg gauge).

ii. hydrogenated at about 200 atms. at room temperature for approximately two hours.

For processes i and ii, the temperature of the alloy on hydrogenating rose quite rapidly indicating a fast activation process (ref. 98), unlike the $Sm(Co,Cu,Fe,Zr)_z$ alloy. The two differently processed materials were then each subsequently ball milled for one hour as described in Section 6.3.2.

As with the $Sm(Co,Cu,Fe,Zr)_z$ type alloy the green compacts made from the Nd-Fe-B alloy powders were vacuum degassed at about 250°C. This removed the majority of hydrogen present and prevented cracking on sintering. Hydrogen is also liberated in a higher temperature range (ref. 98), but this did not cause any green compact cracking.

6.5 Heat Treatments of the Bulk and Green Compact Alloys

6.5.1 Introduction

It has been indicated that during the production of sintered $Sm(Co,Cu,Fe,Zr)_z$ type permanent magnets, a fast cool from a solid solution temperature (S.S.T.) to room temperature was desirable as all the Sm was maintained in solution and a homogeneous precipitation process could then take place on ageing (refs. 104, 105). Kianvash (ref. 100) also found that the intrinsic coercivity was improved

for a quenched specimen rather than an air or furnace cooled treatment.

This investigation has shown that a quenched and isothermally aged Nd-Fe-B alloy sintered magnet has a higher intrinsic coercivity than a furnace cooled and isothermally aged magnet (ref. 97).

6.5.2 The Heat Treatment Apparatus

A suitable furnace system was built so that the specimens could be quickly removed from the furnace zone into a cool region. The system is shown schematically in fig. 6.6 and a photograph is shown in fig. 6.7.

The furnace A was a "Fecralloy A" inductively wound high temperature resistance type, capable of a maximum temperature of 1250^{o}C. The furnace could be moved over the alumina tube B. This tube was connected via a rubber O-ring seal to the copper tubing. The seal was water cooled to prevent the O-ring overheating and breaking the seal. C was a $SmCo_5$ permanent magnet attached to a similar magnet inside the copper tube. The sample, trapped between the baffle D, could then be pulled out of the furnace region so that it dropped into the cylinder at E which was surrounded by liquid nitrogen at F. Since the system was filled with purified argon to a pressure of about 0.75 atm, the cylinder E, when surrounded with liquid nitrogen, cooled to such an extent that some of the argon condensed in the bottom of the cylinder, so that all the samples were effectively quenched in a small amount of purified liquid argon (about 1-2 cm^3).

Metallographic studies were made of three $Sm(Co,Cu,Fe,Zr)_z$ alloy samples which were air cooled, furnace cooled and quenched

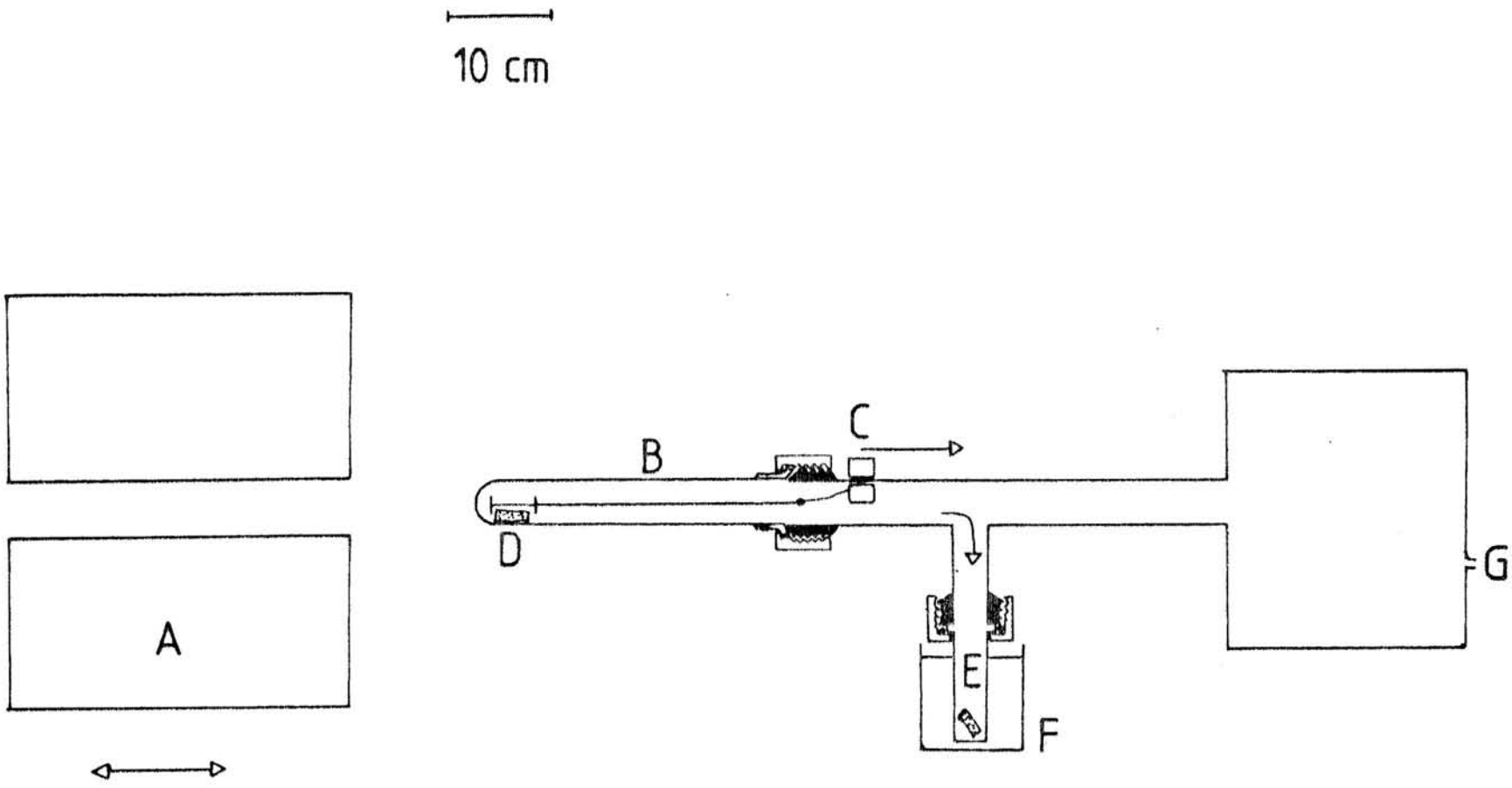

Fig. 6.6 Schematic diagram of the quenching heat treatment system.

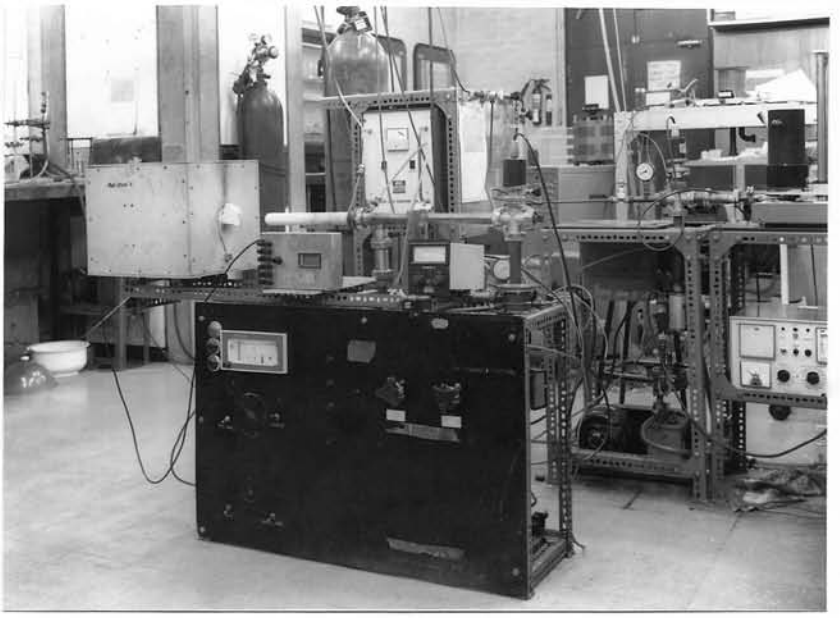

Fig. 6.7 Photograph of the quenching heat treatment system.

using this system. It was found that the quenched sample was essentially single phase, thus indicating the efficiency of the quenching system.

G was the vacuum system, consisting of a rotary pump and oil diffusion pump, and an inlet allowed purified Ar from a "BOC" Rare Gas Purifier to enter the system. The temperatures of the specimens during the heat treatments were measured using a chromel-alumel thermocouple and a "Keithley" digital voltmeter. The maximum fluctuation of temperature in the furnace after stabilizing for about ten minutes was $\pm 5^{o}C$. The voltmeter was linked to a Commodore 64 microcomputer via an 'Interpod' RS232 interface so that a direct read out of the temperature in ^{o}C was possible.

6.5.3 Heat Treatments of the Specimens

To standardize the overall processing procedure of both the alloys, the method of evacuating the quenching system, filling it with Ar and the heating up and cooling down of the specimens were done identically for all the samples; the procedure is described below:

i. a bulk or green compact sample contained in a Ta sleeve was placed in the quenching apparatus.

ii. the system was evacuated to at least 3×10^{-6} torr.

iii. any degassing operations were carried out.

iv. the system was flushed three times with purified Ar; after the second flush the vacuum was allowed to recover

to at least 10^{-5} torr and then filled with purified Ar to a pressure of 0.75 atm.

v. the furnace was pre-heated to the required temperature and then placed over the alumina tube.

vi. the time of heat treatment was started as soon as the specimen reached ± 5°C of the required temperature.

vii. the specimen was then either quenched using the baffle arrangement, air cooled by moving the furnace away from the alumina tube or furnace cooled by switching off the furnace and allowing it to cool to room temperature. The quenched specimens cooled to room temperature from the solid solution temperature in about 1 minute; the air cooled specimens cooled to room temperature in about one hour and the furnace cooled specimens cooled to room temperature in about 12 hours.

The heat treatments of the bulk alloys are described in Section 6.2; the heat treatments of the green compacts of the two alloys are described separately in the next two sections.

6.5.3.i Heat Treatments of the $Sm(Co,Cu,Fe,Zr)_z$ Green Compacts

The heat treatments listed below were chosen to continue work done by Kianvash (ref. 100) and to obtain additional information about this particular alloy composition, which has a lower 'Z-value' than those investigated previously (ref. 100). The heat treatments were used primarily to attempt to optimise the magnetic properties.

A. Heat Treatments of Green Compacts Produced Via Ball Milling Only

a. Solid solution treated (SST) at 1150°C for one hour and quenched; aged isothermally at 800°C for ½ and 1 hour steps to over 30 hours; air cooling after each ageing period (under purified Ar).

b. As for a but SST at 1160°C, 1170°C, 1180°C, 1190°C or 1200°C.

c. Sintered at 1190°C for one hour, cooled to a SST of 1150°C for one hour and then quenched; aged isothermally for ½ and 1 hour steps to over 80 hours with air cooling after each ageing step (under purified Ar).

d. As for c but using a SST of 1160°C, 1170°C, 1180°C or 1190°C.

e. As for c, but SST at 1170°C and after quenching the sample was step aged as follows:

½ hour at 830°C
½ hour at 700°C
1 hour at 600°C
2 hours at 500°C
10 hours at 400°C
then air cooled to room temperature.

At each step the sample was cooled to the next ageing temperature after the previous ageing step was complete.

f. SST at 1170°C for one hour and then quenched; specimens were then isothermally aged at the temperatures below and up to the times indicated; each ageing time step was followed by air cooling.

1. 800°C for over 30 hours
2. 815°C for over 18 hours

3. 830°C for over 14 hours
4. 850°C for over 9 hours
5. 900°C for over 10 hours.

The heat treatments on the green compacts produced by ball milling only are summarised in table 6.2.

B. Green Compacts Produced via HD and Subsequent Ball Milling

a. SST at 1160°C for one hour and then quenched; aged isothermally at 800°C for ½ and 1 hour steps to over 60 hours, with air cooling under purified Ar after each ageing step.

b. As for a but SST at 1170°C, 1180°C or 1190°C.

c. Sintered at 1190°C for one hour, cooled to a SST of 1160°C for one hour and then quenched; aged isothermally for ½ and 1 hour steps to over 80 hours with air cooling under purified Ar after each ageing step.

d. As for c but SST at 1170°C, 1180°C or 1190°C.

The heat treatments on the HD green compacts are summarised in table 6.3.

6.5.3.ii Heat Treatments of the Nd-Fe-B Green Compacts

The heat treatments listed below were used to give more information about the variation of the magnetic properties of the samples, particularly with different isothermal ageing temperatures.

A. Green Compacts Produced via Ball Milling Only

a. SST at 1100°C for one hour and then quenched; aged isothermally

TABLE 6.2 Summary of Ball Milled Only 'Green' Compact Heat Treatments for the $Sm(Co,Cu,Fe,Zr)_z$ Alloy.

Heat Treatment					Ageing Treatment	
1		2				
Temp. (°C)	Time (hours)	Temp. (°C)	Time (hours)		Temp. (°C)	Time (hours)
1150	1	Quenched			800	over 30
1160	1	"				
1170	1	"				
1180	1	"				
1190	1	"				
1200	1	"				
1190	1	1150	1	Quenched	800	over 80
1190	1	1160	1	"	"	"
1190	1	1170	1	"	"	"
1190	1	1180	1	"	"	"
1190	1	1190	1	"	"	"
1190	1	1170	1	"	½ hour 830°C; ½ hour 700°C; 1 hour 600°C; 2 hours 500°C; 10 hours 400°C.	
1170	1	Quenched			800	over 30
1170	1	"			815	" 18
1170	1	"			830	" 14
1170	1	"			850	" 9
1170	1	"			900	" 10

TABLE 6.3 Summary of the Hydrogenated and then Ball Milled 'Green' Compact Heat Treatments for the $Sm(Co,Cu,Fe,Zr)_z$ Alloy.

Heat Treatment					Ageing Treatment	
1		2				
Temp. (°C)	Time (hours)	Temp. (°C)	Time (hours)		Temp. (°C)	Time (hours)
1160	1	Quenched			800	over 60
1170	1	"			"	"
1180	1	"			"	"
1190	1	"			"	"
1190	1	1160	1	Quenched	800	over 80
1190	1	1170	1	"	"	"
1190	1	1180	1	"	"	"
1190	1	1190	1	"	"	"

at 600°C for between 5 and 30 minute intervals to over 80 hours, and air cooling under purified Ar after each ageing period.

b. As for a but SST at 1100°C for one hour and then furnace cooled to room temperature.

c. As for a but isothermally aged at 540°C.

d. As for a but isothermally aged at 570°C.

e. As for a but isothermally aged at 630°C.

f. As for a but isothermally aged at 660°C.

The heat treatments are summarised in table 6.4.

B. Green Compacts Produced via HD and Subsequent Ball Milling

a. The material pressurised at about 33 atms. was SST at 1100°C for one hour and then quenched, aged isothermally at 600°C for between 5 and 30 minute intervals to over 18 hours and air cooled under purified Ar after each ageing step.

b. As for a but using powder that had been made by pressurising at 200 atms. and then ball milling.

These heat treatments are summarised in table 6.5.

6.6 Density Measurements

Density measurements were made on all the samples as they give a good indication of the extent of the sintering operation. This is achieved by calculating the ratio of the sintered density to the bulk density.

TABLE 6.4 Summary of Ball Milled Only 'Green' Compact Heat Treatments for the Nd-Fe-B Alloy.

Heat Treatment			Ageing Treatment	
Temperature (°C)	Time (hours)		Temperature (°C)	Time (hours)
1100	1	Quenched	600	up to 80 hours
1100	1	Furnace cooled	600	"
1100	1	Quenched	540	"
1100	1	"	570	"
1100	1	"	630	"
1100	1	"	660	"

TABLE 6.5 Summary of the Hydrogenated and Ball Milled Green Compact Heat Treatments for the Nd-Fe-B Alloy.

Hydrogenation Decrepitation Pressure	Heat Treatment			Ageing Treatment	
(atm)	Temp. (^{o}C)	Time (hours)		Temp. (^{o}C)	Time (hours)
33 (2 hours) (room temperature)	1100	1	Quenched	600	over 18
200 (2 hours) (room temperature)	1100	1	"	600	"

An "MBL" 50 cm^3 capillary action glass density bottle was used with distilled water at room temperature. The bottle was filled with distilled water and any excess water carefully wiped off the outer surface; the filled bottle was then weighed on a "Sartorius" balance. A sample was weighed on the balance and then placed in the distilled water filled density bottle and any excess water was again carefully wiped off the bottle. The density could be calculated using the formula:

$$\text{density of sample in kg m}^{-3} = \frac{(\text{mass of sample in kg}) \times (\text{density of water in kgm}^{-3})}{[(\text{mass of bottle and water}) - \{(\text{mass of bottle, water and sample}) - (\text{mass of sample})\}]} \quad (6.1)$$

The errors with this method arose from inadequate removal of excess water from the bottle before weighing, variations in room temperature, affecting the capillary action and air bubbles on the specimen surface. The errors were estimated to be about $\pm$ 0.2 kg m^{-3}.

6.7 Degassing (Microbalance) Studies of the Hydrogenated $Sm(Co,Cu,Fe,Zr)_z$ and Nd-Fe-B Alloys

The equipment used for the degassing studies has been described elsewhere (ref. 106). The studies were undertaken for two reasons:

i. to find the approximate temperature or temperatures at which hydrogen was released from the HD material.

ii. to calculate the approximate weight % of hydrogen absorbed by the HD material.

Approximately 0.17 g of material was placed in a silica bucket, which was then placed in the system. The system was evacuated to approximately 10^{-6} torr and the sample was heated at a rate of 4^{o}C/min. until the mass change became zero. The weight % of hydrogen lost was calculated by dividing the final mass of the material by the initial mass.

6.8 Magnetic Measurements

6.8.1 Pulse Magnetizer

The sintered alloy specimens were pulsed in a field of approximately 60 KOe in order to saturate them. The principle is that energy is stored in a capacitor and discharged in a very short period of time: this allows high peak magnetizing fields. A simple circuit diagram is shown in fig. 6.8. The coil design is important as an overdamped circuit will limit the peak current; a typical critically dampled discharge current waveform is shown in fig. 6.9.

The coil design presently in use is based on the "Bitter" magnet type, as this was mechanically rigid and designed to withstand the force produced by the current. It is composed of 50 thin copper discs about 5 cm in diameter and 0.1 cm thick with a central hole of 1 cm diameter and a narrow radial slot. Each disc is insulated from the next by sheets of thin insulating material. Each copper disc is rotated about 20^{o} with respect to its neighbour and a conducting path is provided by the region of overlap. Therefore the total conducting path is helical as in a solenoid. The stack of discs is illustrated in fig. 6.10.

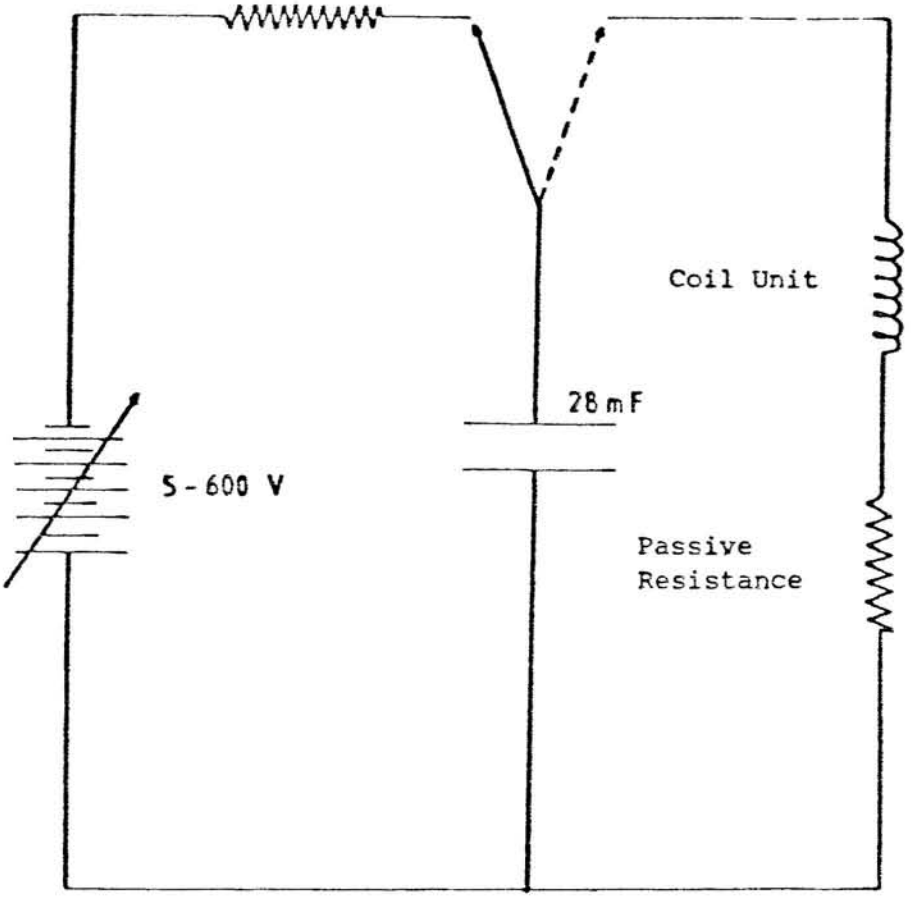

Fig. 6.8 Simplified circuit diagram of pulse magnetizer.

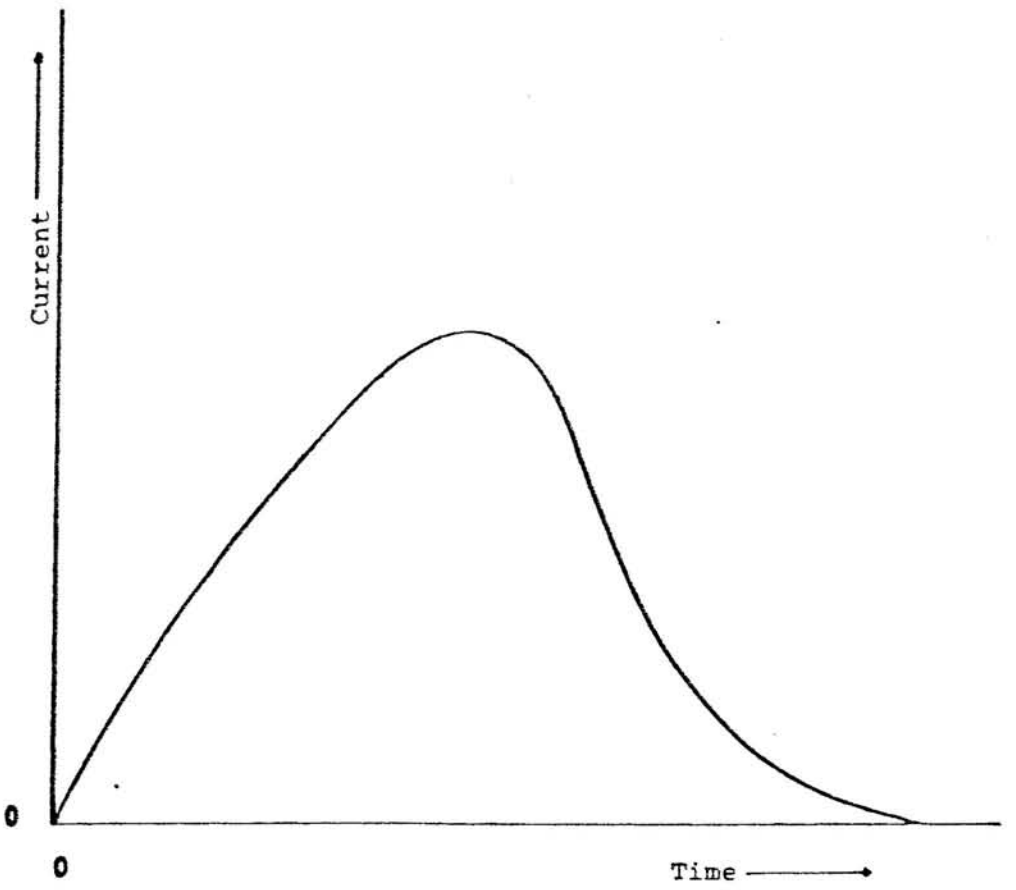

Fig. 6.9 Critically damped waveform from pulse magnetizer.

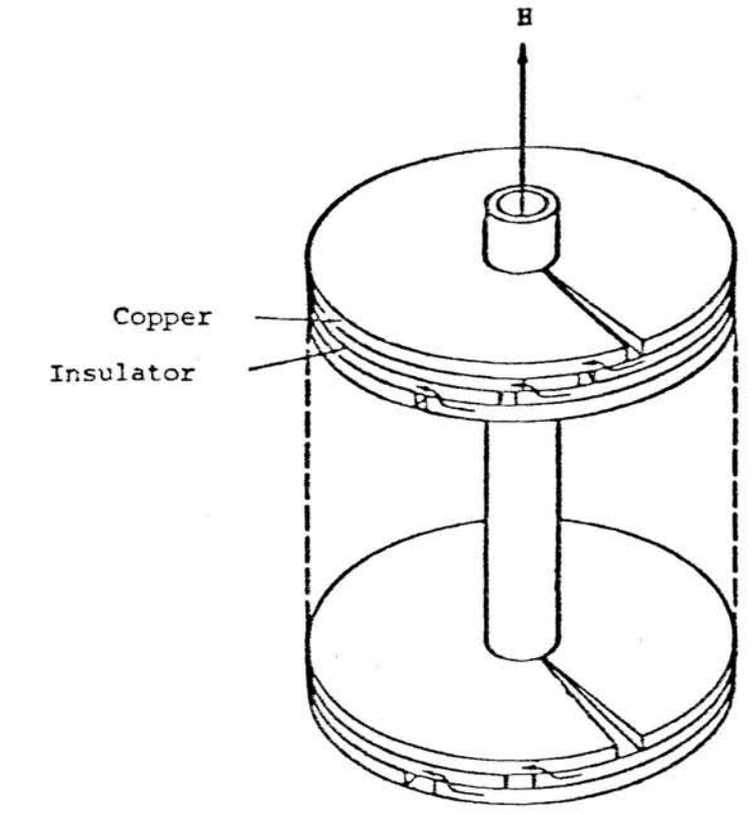

(a)

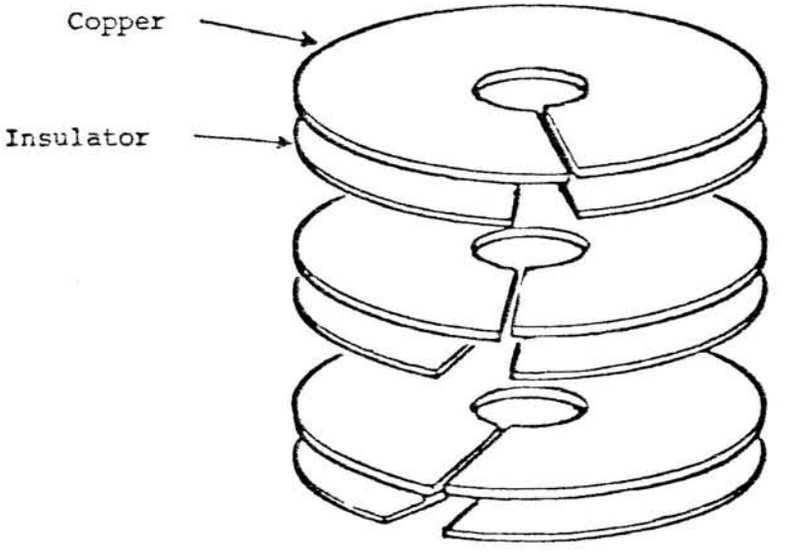

(b)

Figs.6.10 (a,b). (a) Bitter magnet coil,
(b) details of plate pieces
for Bitter magnet.

The Bitter magnet has been calibrated by other workers (refs. 100,102) using a small search coil calibrated in an electromagnet with a known current field characteristic and placed in the Bitter magnet. The resultant voltage induced from a negative pulse was displayed on an oscilloscope and a field of 61.25 KOe was obtained for a 1 cm bore at 360-370 V d.c.

6.8.2 Computerised Magnetic Measurements

A measuring system was built during the course of this work that could, using computer software and the necessary analogue to digital (AD) converter, quickly provide all the required magnetic property information.

6.8.2.i Description of the Measuring System

The system consisted of a "Varian" model V-4007, 15 cm high voltage - low current electromagnet with cylindrical pole caps, providing a uniform field between the poles. The electromagnet was powered by a "Varian" model V-2200 regulated power supply designed to provide a stable direct current.

A set of four search coils were used to measure the electromagnet field and the magnetic intensity (B-H) of the sample. Each coil consisted of 2000 turns of "Enfield Soldereze" polyurethane insulated wire of diameter 0.071 mm. Each search coil was made by winding the wire onto a PTFE former with a length of 1 cm and diameter of about 0.6 cm. A search coil is illustrated schematically in fig. 6.11. The search coils were positioned so that one coil was surrounded by the three other coils which were

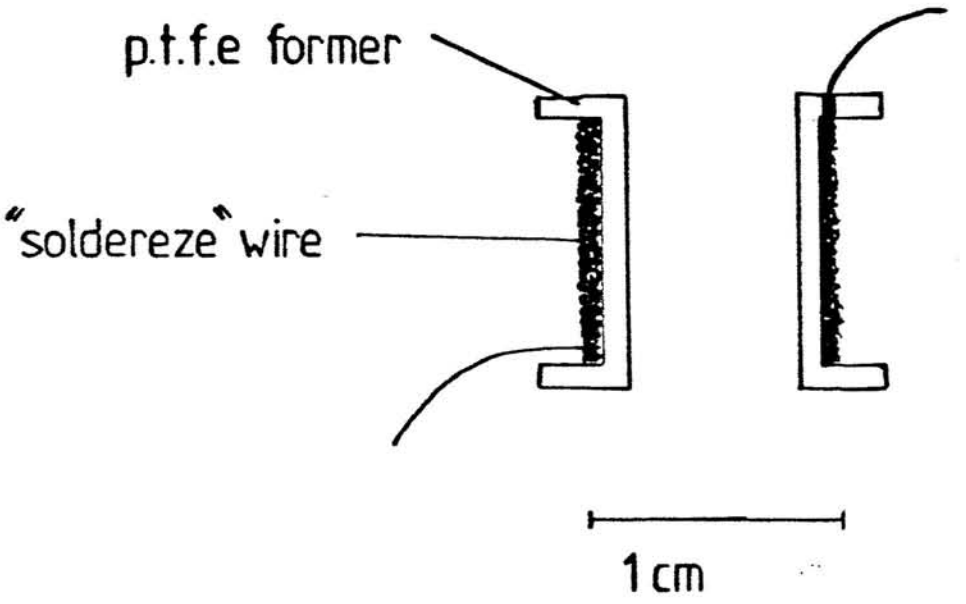

Fig. 6.11 Schematic diagram of a search coil used in the magnetic measurements.

at 120^{o} to each other and 2 cm from the specimen coil. The coils were protected in a thin perspex case. The centre coil was connected in series opposition with a neutralising coil so that the magnetic intensity (B-H) could be measured, or it was disconnected so that the magnetic induction (B) could be measured. A compensating coil was used to allow for the fact that the specimen coil was not wound directly onto the sample. The fourth coil measured the magnetic field produced by the electromagnet. The output of the coils was connected to a double channel flux integrator as shown schematically in fig. 6.12.

The integrator outputs were connected to a two channel relay which passed on the signals to a "Farnell" Omnibus OB2, AD converter. The AD converter was connected to a "Commodore" 3032 32K microcomputer via a standard IEEE 488 24 way parallel connector.

The measuring system is shown schematically in fig. 6.13 and a photograph is shown in fig. 6.14.

The circuit diagrams for the flux integrator and two-channel relay are shown in Appendix B.

6.8.2.ii Measuring Procedure

A pulsed magnetic test sample was placed in the specimen search coil and the coils were placed between the poles of the electromagnet ensuring that the parallel faces of the specimen contact the pole faces, thereby eliminating any demagnetizing effect due to the presence of free magnetic poles. Thus, all

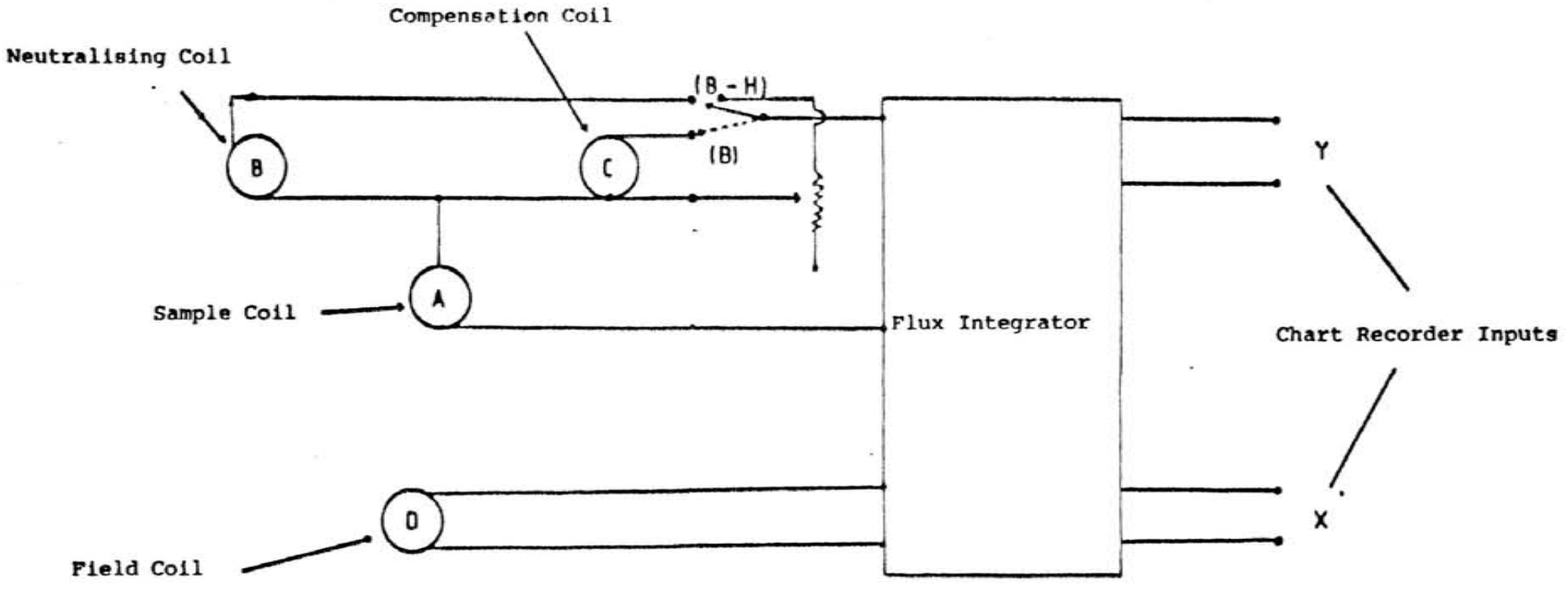

Fig.6.12 Function of search coils in B and B-H integrator in schematic form.

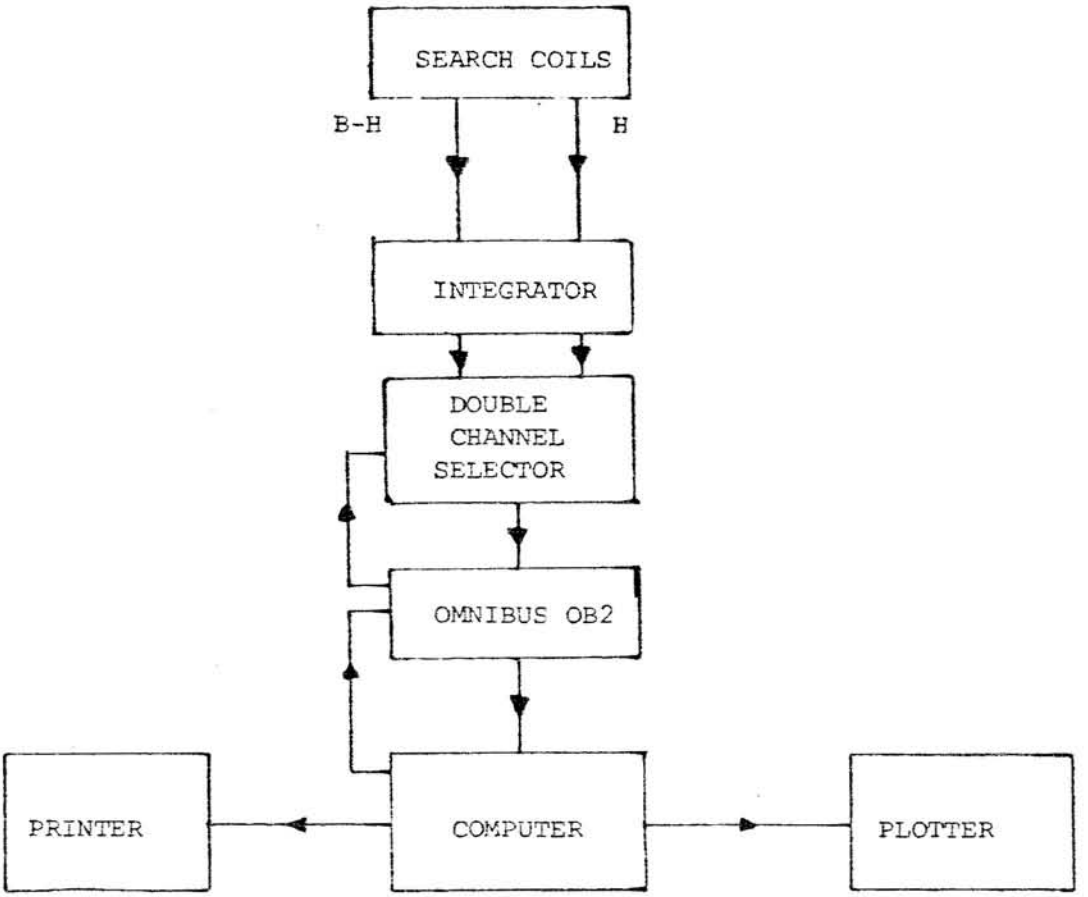

Fig. 6.13 Magnetic Measuring System.

Fig. 6.14 Photograph of magnetic property measuring apparatus.

the specimens were carefully ground (before pulsing) using 1200 grit paper to a length of 1.38 cm.

On applying a reverse field the coil containing the sample obtains an induced emf proportional to the rate of change of flux within the specimen $(\frac{dB}{dt})$; the neutralising coil similarly obtains an induced emf proportional to the rate of flux change within its own area. Since the coils are connected in series opposition, the resultant signal will be proportional to B-H and the field produced by the electromagnet is measured by the field coil.

The computer program "Magnum" (see Appendix C) that was used, accepted the data from the AD converter each time the field was increased in steps. This continued until the intensity of magnetization was zero (B-H = 0). The second quadrant hysteresis loop and the magnetic parameters were printed on a "J.J. Lloyd" PD4 plotter and "Commodore" 4022 printer respectively. The accuracy of the results depends primarily on the intervals between each field increment as this determines the "smoothness" of the second quadrant hysteresis loop.

6.8.2.iii Calibration of the Measuring System

The system was calibrated, so that the digital readings from the AD convertor could be converted to the dimensions of magnetic properties.

The electromagnet field was calibrated by plotting coil current against Hall probe value, using a semiconductor Hall probe connected to a "LDJ" model 511P gaussmeter.

The field versus AD converter digital reading was measured and this enabled a calibration equation to be incorporated in the computer program.

The calibration of the intensity of magnetization (B-H) was carried out by saturating a standard 99.99% purity nickel sample of volume 0.413 cm^3 and with $4\pi M_s$ equal to 6.184 kG; the corresponding digital reading at saturation was noted. The calibration was taken for 1 cm^3 of magnetic material, and all the values of remanence and energy product were quoted for 1 cm^3 of the material.

All the above calibrations are detailed in Appendix D.

6.9 Microhardness Measurements on the Alloys

6.9.1 Introduction

Microhardness measurements were made on some of the bulk and sintered samples of both the alloys studied in this project. The reason for the measurements is to extend the work by Kianvash, who showed that for the $Sm(Co,Cu,Fe,Zr)_z$ alloys, the domain pinning coercivity mechanism is concurrent with a dislocation pinning mechanism that causes a change in microhardness with isothermal ageing time (ref. 96). In addition, measurements were made on the Nd-Fe-B alloy in an attempt to provide information on the coercivity mechanism in this material.

6.9.2 Microhardness Measuring Technique

One flat surface of the samples to be tested was ground

to 1200 grit emery paper and then polished to $\frac{1}{4}$ μ diamond paste after the initial S.S.T. heat treatment. This minimised the effects of surface preparation on the hardness values, since, on isothermal ageing the crystal damage associated with the grinding process was recovered.

The bulk samples to be hardness tested were mounted in hard bakelite and polished to produce a flat, parallel surface. The sintered samples were cylindrical in shape so that rather than mount the sample in bakelite, they were clamped tightly in a small hand clamp: the differences in the hardness values between a bakelite mounted sintered sample and a clamped sintered sample were negligible and were well within experimental errors.

A "Leitz" microhardness tester was used to perform the Vickers hardness test. The apparatus employed a small diamond indenter incorporated in an optical microscope, the diameter of the indentation being a measure of the hardness. The reflectivity of etched samples was too low to afford easy visibility of the indentations and so the tests were performed on unetched specimens. The hardness value was achieved by measuring 10 indentations and taking the average.

The errors were calculated using the equation below:

$$\pm \text{ error on average microhardness value} = \frac{\sqrt{\sum_{i=1}^{n} (x_i - a)^2}}{n} \qquad (6.2)$$

n is the total number of readings, giving an average microhardness a. $\sum_{i=1}^{n} (x_i - a)^2$ is the sum of the squares of the value remaining after the average value is subtracted from each reading x_i.

6.9.3 Samples Chosen for Microhardness Measurements

6.9.3.i Measurements on the $Sm(Co,Cu,Fe,Zr)_z$ Alloy

A bulk sample was solid solution treated at 1170°C for 2 hours and then quenched, and aged isothermally at 800°C for ½ and 1 hour steps. Microhardness measurements were made on the bulk sample after each ageing step.

Sintered samples were solid solution treated at 1170°C for 1 hour and then quenched, and then isothermally aged for ½ and 1 hour steps at the temperatures below:

a. 800°C

b. 830°C

c. 850°C

d. 900°C.

6.9.3.ii Measurements on the Nd-Fe-B Alloy

Microhardness measurements were made on the two bulk samples below:

a. SST at 1100°C for one hour and quenched; then isothermally aged at 600°C for between 5 and 30 minute intervals.

b. SST at 1100°C for one hour and furnace cooled to room

temperature; then isothermally aged at 600°C for between 5 and 30 minute intervals.

Microhardness measurements were also made on the sintered samples below:

a. SST at 1100°C for one hour and then quenced; then isothermally aged at 600°C for between 5 and 30 minute intervals.

b. SST at 1100°C for one hour and then furnace cooled to room temperature and isothermally aged at 600°C for between 5 and 30 minute intervals.

Microhardness measurements were made on four sintered samples each SST at 1100°C for one hour, quenched, and then aged at the temperatures for up to 1000 minutes:

a. 540°C

b. 570°C

c. 630°C

d. 660°C.

6.10 Electrical Resistivity Measurements

6.10.1 Introduction

Smallman (ref. 107) has described the variation of electrical resistivity with ageing time for Al-Cu alloys. The ageing process in these alloys involves the formation of coherent precipitates which pin dislocations. Electrical resistivity measurements were

used in an attempt to follow the precipitation processes in the $Sm(Co,Cu,Fe,Zr)_z$ alloy.

6.10.2 Apparatus used in Electrical Resistivity Measurements

The method used to obtain a value of the electrical resistivity was based on the Standard Four-Probe Method described in a number of texts (see for example ref. 108). A known current is passed through the sample and the voltage drop is measured across a specific distance. From Ohm's Law (V = IR), the electrical resistance can be calculated, and from the equation below the electrical resistivity can be calculated:

$$\text{electrical resistivity } \rho = \frac{RA}{l} \quad (\text{in } \Omega \text{ cm}) \tag{6.3}$$

A is the sample cross-sectional area, l is the voltage drop probe gap and R is the electrical resistance.

The apparatus consisted of a perspex frame through which four hardened steel screws with pointed ends passed to hold a symmetrical specimen (fig. 6.15).

A stabilised 1 A d.c. was supplied from a "Farnell" power supply which was tested using a "Cambridge" 1 Ω standard resistor.

The current and voltage drop were measured on a "Keithley" digital voltmeter and averaged out using a "Cambridge" reversing switch.

The apparatus is illustrated schematically in fig. 6.16.

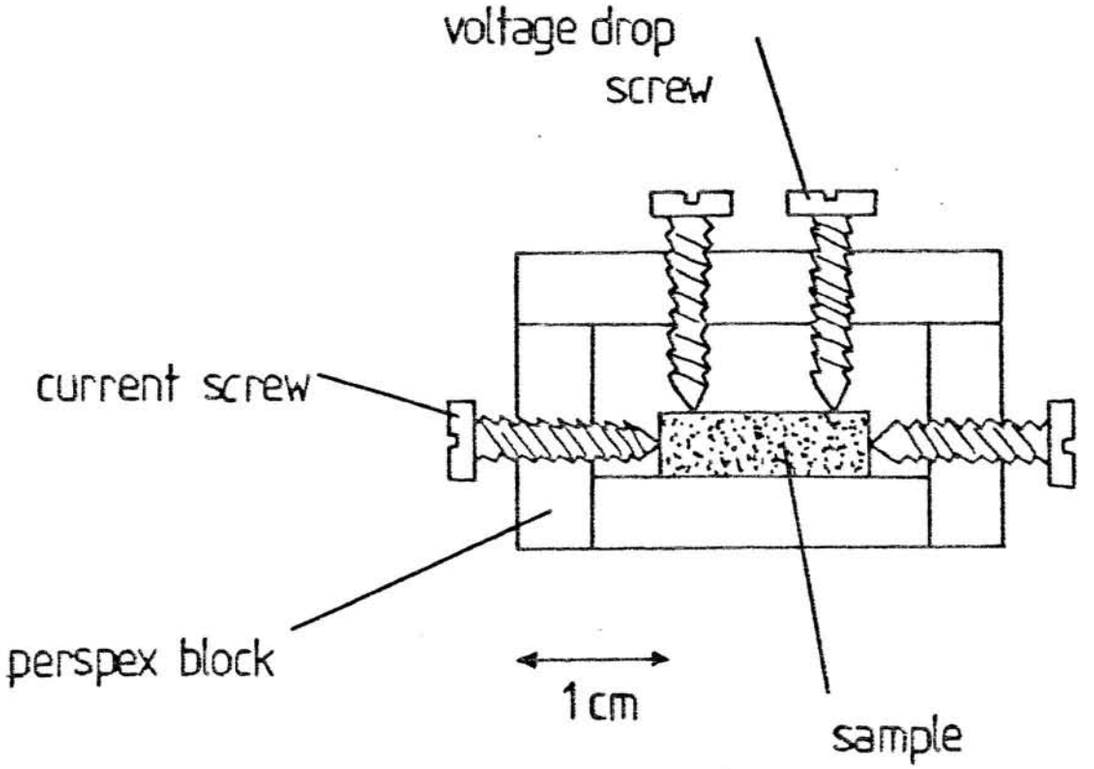

Fig. 6.15 Diagram of the four point electrical resistivity measuring sample holder.

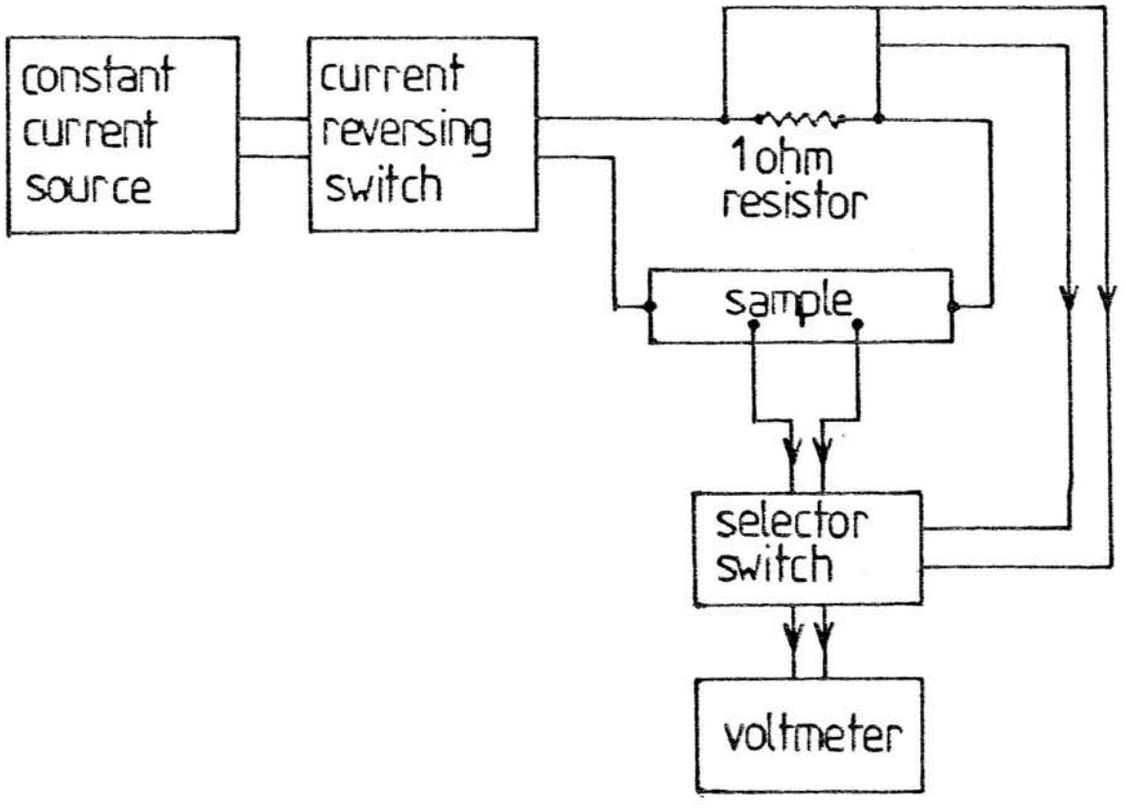

Fig. 6.16 Schematic diagram of four point electrical resistivity measuring rig.

6.10.3 Procedure for Measuring the Electrical Resistivity

A sample was placed symmetrically in the perspex frame (see fig. 6.15) and the four screws were tightened so that the points touched the sample. A 1 A d.c. was passed through the sample and the voltage drop was read off the voltmeter. The current was then reversed and the voltage drop read off again. An average value was then calculated for the voltage drop.

From Ohms' Law, since I is 1 then the electrical resistance (in μΩ) was directly equal to the voltage drop (in μV). Using equation 6.3, where 1 = 0.615 cm:

$$\rho = \frac{R.A}{0.615} \quad \mu\Omega \text{ cm}$$

A is the sample cross-sectional area (in cm^2) measured using a "Moore and Wright" micrometer.

To test the accuracy of the four-point apparatus an Invar cylindrical sample was made and the electrical resistivity calculated using the equipment. The results below show that the apparatus was accurate enough to show a change in resistivity of ± 3 μΩ cm.

Invar [64% Fe 36% Ni] reference value (ref. 109)

of electrical resistivity = 81 μΩ cm.

Value of electrical resistivity produced by

four-point rig = 82.5 μΩ cm.

The results were calculated to give the relative electrical resistivity,

ρ/ρ_o. ρ_o is the initial electrical resistivity value before isothermal ageing.

6.11 Optical Metallography of the Alloys

The sintered specimens were first demagnetized using a "Varian" high voltage low current electromagnet. Both bulk and sintered specimens were mounted in conducting bakelite as this was necessary for the scanning electron microscope (SEM) studies.

After mounting, the specimens were ground on four grades of wet and dry paper (150, 320, 800 and 1200); each change of grade coincided with rotating the mount so that the scratches left by the previous paper were replaced by finer ones at right angles on the specimen surface.

After grinding, the specimens were polished on a cloth covered polishing wheel and charged with 6, 1 and $\frac{1}{4}$ μ "dialap" diamond paste. The final polishing stage involved using 0.05 μ alumina suspended in distilled water on a cloth covered polishing wheel. After each polishing stage the specimens were washed in running water using "Teepol" detergent and then alcohol and were dried with a "Buehler" specimen drier.

The polished specimens were etched the particular treatment depending on which alloy was being investigated. The two etching procedures are shown below:

i. for $Sm(Co,Cu,Fe,Zr)_z$, about 1 second in 2% nital at room temperature.

ii. for Nd-Fe-B, about 15 seconds in 2% nital at room temperature.

The etched specimens were then observed and photographed using a "Zeiss" Ultraphot microscope.

6.12 SEM Studies of the Alloys Investigated

For the electron microscope studies the mounted, polished and unetched specimens were adhered to specimen holders using "Bostik" adhesive and vacuum dried for 3-4 minutes. A thin conducting line of "electrodag" was applied between the bakelite mounting and specimen holder in order to provide a conducting path. The specimens were investigated on a "Philips" PSEM 500 scanning electron microscope (SEM) and secondary and backscattered images were photographed using a "Praktica" L2 camera.

Energy dispersive X-ray analyses (EDAX) were made on the specimens using a "ISI" 100A SEM. The spot analyses were converted using a "Link System" microcomputer into weight %.

The powders used in producing the sintered specimens were adhered to specimen holders using double sided adhesive tape. The powders were then gold coated using a "Polaron" EM5000 gold coating apparatus; this provided a conducting path for the mounted powders. These specimens were then studied using a "Philips" PSEM 500 SEM.

CHAPTER SEVEN

RESULTS AND DISCUSSION ON THE $Sm(Co,Cu,Fe,Zr)_z$ ALLOY

7.1 Introduction

This chapter contains the results of the investigations on a $Sm(Co_{0.66}Cu_{0.10}Fe_{0.22}Zr_{0.02})_{7.37}$ alloy.

The bulk alloy in the "as cast" and heat treated conditions is discussed first using the results of optical metallography and SEM studies. The character of the powders used in the production of the magnet samples are also discussed using SEM studies.

The magnetic properties of samples produced from ball milled only (BMO) and hydrogen decrepitated and ball milled (HD) materials are discussed in the next sections as functions of different heat treatments. It should be noted that the magnetic properties were rather low when compared with the values quoted for commercial magnets. These low values can be attributed principally to the larger particle sizes of the powders used to make the samples which leads to lower densities and lower maximum energy products (BH_{max}).

Studies of the variations of the electrical resistivity and microhardness with ageing time are discussed and correlated with the variations of intrinsic coercivity with ageing time.

The final sections consist of optical metallography and SEM studies (including X-ray microanalysis) of the heat treated sintered samples.

7.2 Studies of the Bulk Alloy

7.2.1 Optical Metallography of the Bulk Alloy

7.2.1.i Study of the "As Cast" Alloy

A small piece of the as cast alloy was observed under an optical microscope. The microstructure shown in Fig. 7.1 is very similar to that observed by Kianvash (ref. 100). It has been reported (refs. 69, 110) that the dark phase is rich in Sm and Cu and deficient in Co and Fe indicating a 1:5 or 2:7 type phase; the light grey matrix was found to be relatively rich in Co and Fe, and deficient in Sm and Cu, this is a general characteristic of the 2:17 phase and the light regions were identified as a Zr-rich and Sm depleted phase (ZRSD). The present analysis of these phases is described later (see Section 7.2.2).

7.2.1.ii Study of the Heat Treated Bulk Alloy

In Fig. 7.2 an optical micrograph is shown of the bulk material in the "as quenched" condition after solid solution treatment (SST) at 1170^{o}C for one hour. Several large single grains can be observed with some grains containing a substructure of a second phase which could form during the quenching treatment. In Fig. 7.3 a second sample has been subsequently aged at 800^{o}C for over 30 hours after quenching from 1170^{o}C. The microstructure of both these samples are also very similar to the results obtained by Kianvash (ref. 100) thus indicating that a "z-value" range of $z = 7.37$ to $z = 8.92$ does not affect the microstructure of the bulk alloy.

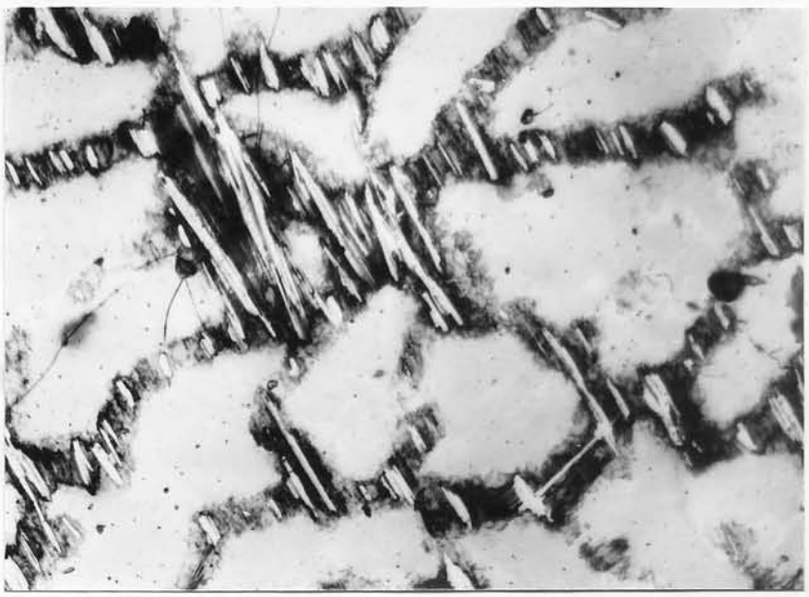

Fig. 7.1 Optical micrograph of "as cast" specimen. (x 400).

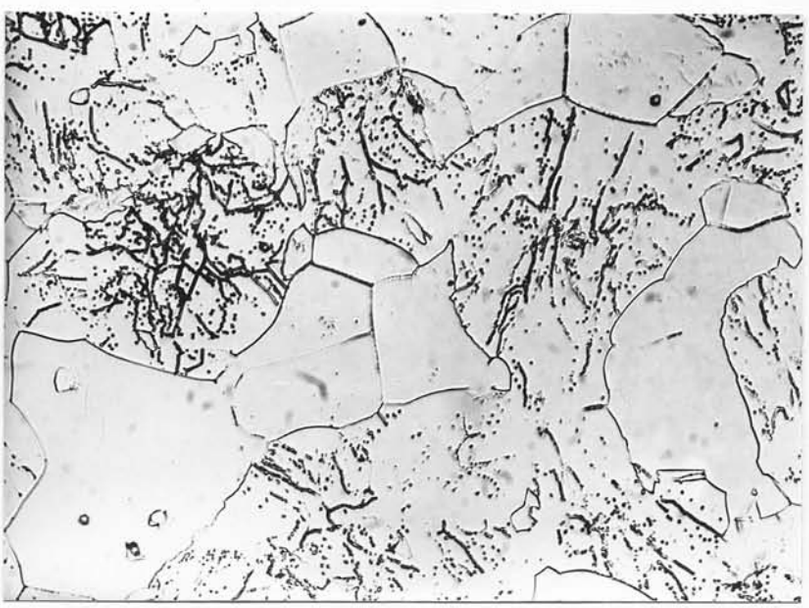

Fig. 7.2 Optical micrograph of bulk specimen SST at 1170°C for one hour and then quenched. (x 400).

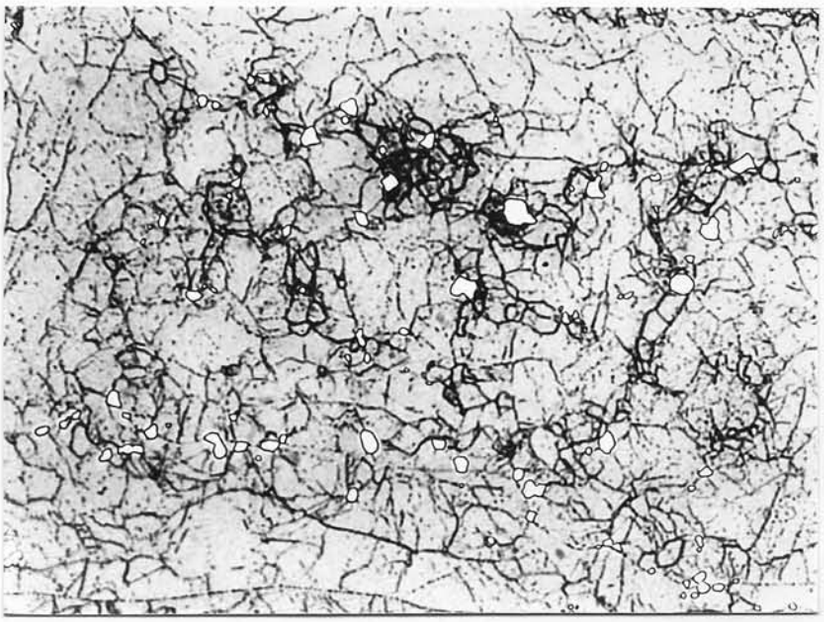

Fig. 7.3 Optical micrograph of bulk specimen SST at 1170°C for one hour, quenched and then aged at 800°C for over 30 hours. (x 400).

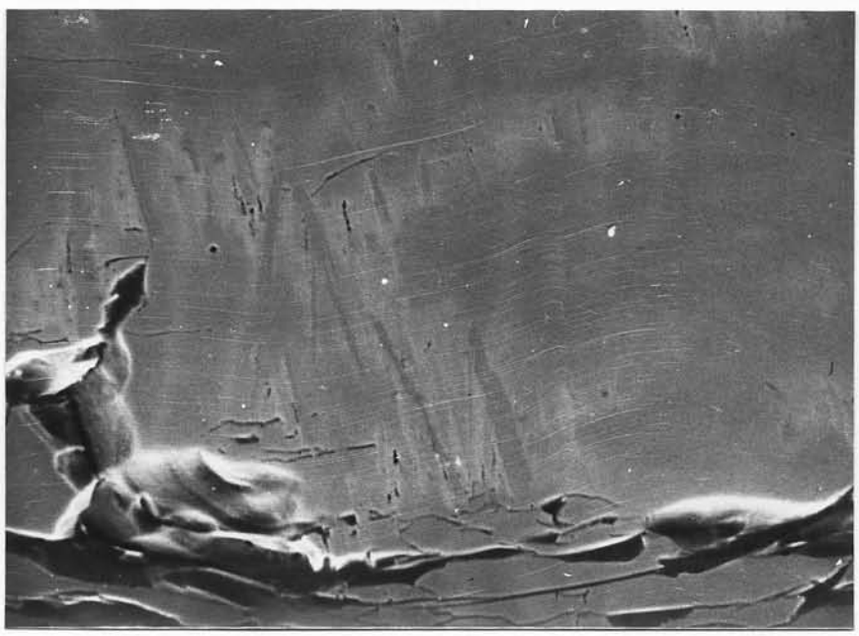

Fig. 7.4a Secondary electron SEM micrograph of the "as cast" specimen. (x 640).

The sample SST at 1170°C and quenched was found to have a similar composition to the light grey matrix phase in Fig. 7.1; Kianvash (ref. 100) has shown that this phase corresponds to the 2:17 composition.

The sample that has been isothermally aged (Fig. 7.3) contains regions of a light phase in the matrix;this phase is the ZRSD phase as observed in Fig. 7.1. The "Thread-like" phase observed within the matrix phase has been shown to be Cu-rich (ref.100) and is associated with the coherent precipitates that are responsible for the coercivity mechanism in this alloy.

7.2.2 SEM Studies of the "As Cast" Alloy

The SEM studies were undertaken to obtain information on the microstructure before the sintered samples were observed, so that any changes in microstructure or phase composition could be seen in the bulk samples that might be on too fine a scale in the sintered samples. The secondary electron image is shown in Fig. 7.4a for the "as cast" alloy and the back scattered image is shown in Fig. 7.4b.

The matrix appears grey in Fig. 7.4a, while the phase that appears light in Fig. 7.1 is slightly darker than the matrix. A light grey phase can also be seen which is the dark phase in Fig. 7.1.

X-ray microanalysis (EDAX) of the phases gave the following results (the phases are described as they appear in the backscattered image in Fig. 7.4b):

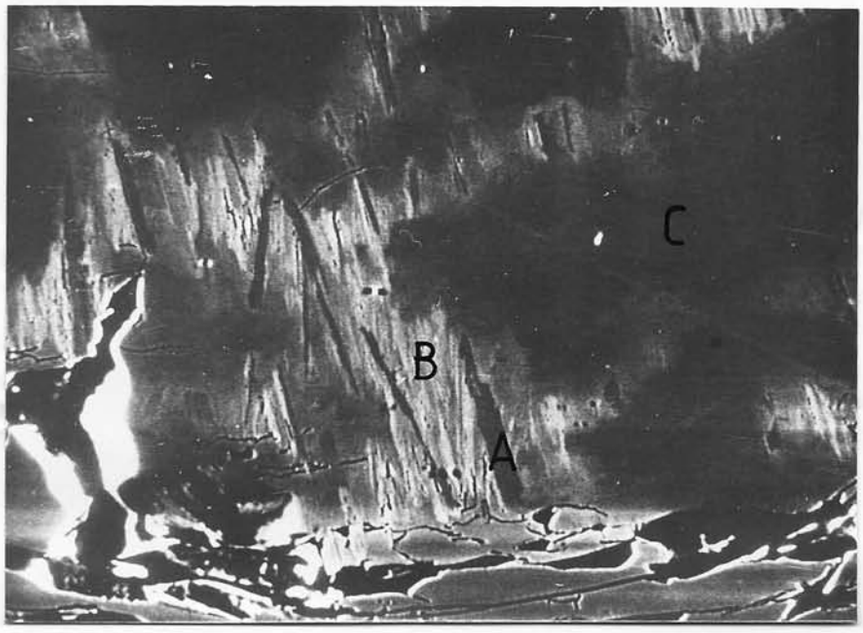

Fig. 7.4b Backscattered SEM micrograph of the "as cast" specimen. (x 640).

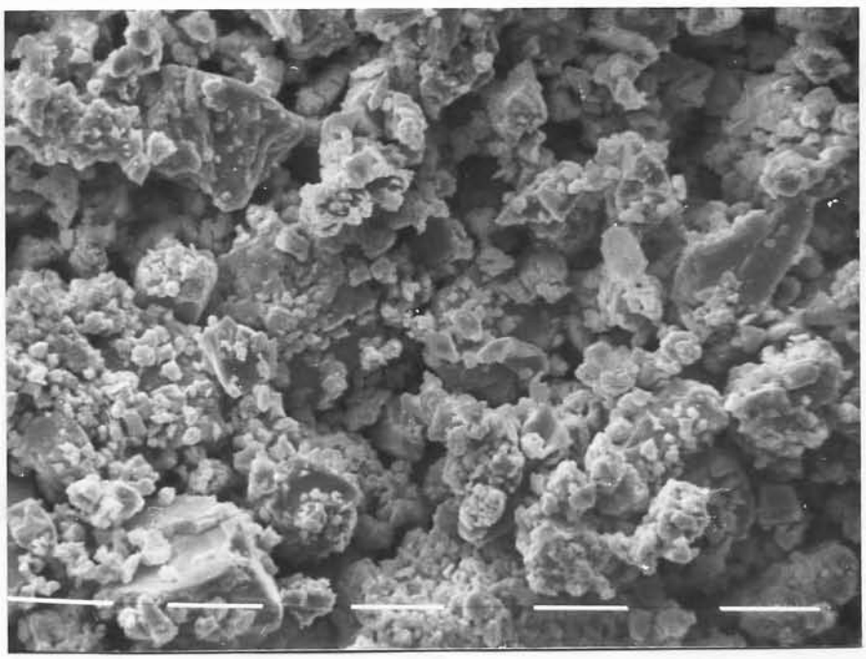

Fig. 7.5a Secondary SEM image of BMO powder. (x1250). (10 μ markers).

i Dark Phase (A) : $Sm(Co_{0.65}Cu_{0.05}Fe_{0.16}Zr_{0.14})_{10.36}$

ii Light Phase (B) : $Sm(Co_{0.46}Cu_{0.41}Fe_{0.12}Zr_{0.01})_{4.13}$

iii Matrix (C) : $Sm(Co_{0.68}Cu_{0.06}Fe_{0.25}Zr_{0.01})_{8.35}$

The errors on these substitution compositions were estimated as being about ±0.03 to ±0.05. These results agree very well with Kianvash (ref. 100) and indicate the presence of: 1. a Co and Fe rich matrix; 2. a Cu and Sm rich light phase; and a 3. a ZRSD dark phase. To avoid a repeat of work done previously by Kianvash (ref. 100) further bulk microscope studies of this alloy were not undertaken.

7.2.3 SEM studies of the Powders Used in the Production of the Specimens

These studies were undertaken to indicate the particle sizes achieved using the different powder production routes.

7.2.3.i SEM Study of the Ball Milled Powder

The secondary electron micrograph of the ball milled powder produced as detailed in section 6.3.1b. is shown in Fig.7.5a, with 10μ markers. The powder consists of large particles of about 10 to 20μ diameter, accompanied by smaller particles of less than 3 to 5μ diameter.

In terms of the particle size requirement for producing permanent magnets, most workers have used about 4μ diameter particles (see for example, ref. 77), as these would be single grain particles which aid

the aligning process and the size of the particle would result in an increased density.

7.2.3ii SEM Study of the HD Powder

The hydrogen decrepitated (HD) powder was produced as detailed in Section 6.4.2. The secondary electron micrograph is shown in Fig. 7.5b, with 10μ markers. The particle size is about 100μ in diameter which agrees with the results of Kianvash (ref. 100). Some of the particles have fine cracks in them and the particle surfaces are smooth, suggesting that the HD material was very friable.

7.2.3iii SEM Study of the Hydrogen Decrepitated and then Ball Milled Powder

This material was hydrogen decrepitated and then ball milled as detailed in section 6.3.1. The secondary electron micrograph is shown in Fig. 7.5c with 10μ markers. The particle size lies between 10 and 50μ in diameter. The size is in agreement with the low densities achieved with this material and the large amounts of porosity observed under the SEM. (See Fig. 7.47).

It can be seen that the HD process is a viable process providing a small enough particle size can be achieved for producing the green compacts. There are a number of ways that this can be done, and would feature in a detailed future investigation:

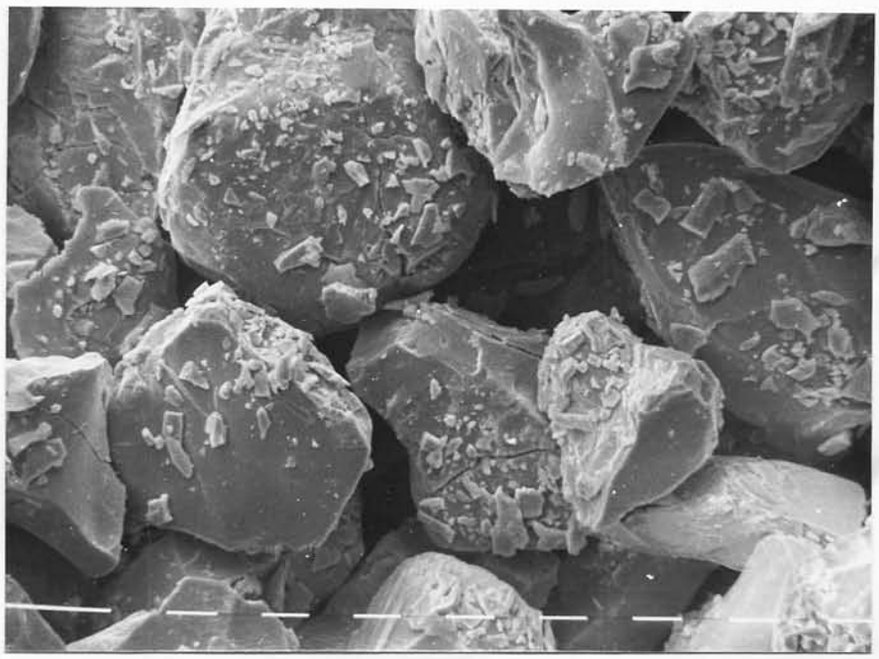

Fig. 7.5b Secondary SEM image of material HD at 200 atm. and 200°C for about 12 hours. (x 640). (10 μ markers).

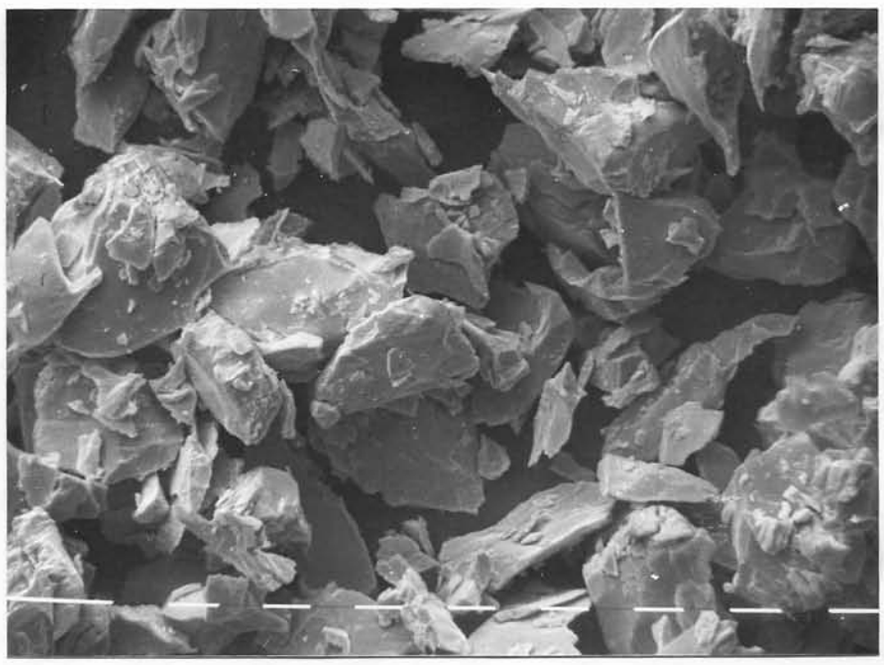

Fig. 7.5c Secondary SEM image of ^{HD} and then ball milled material. (x 640). (10 μ markers).

1. The use of higher hydrogen pressures for decrepitating.
2. The use of higher temperatures for decrepitating.
3. The use of different ratios of balls to material during the ball milling stage to alter the degree of agitation during ball milling.
4. The use of different ball milling times.

7.3 Magnetic Properties of the Sintered Specimens produced from Ball Milled Only Powder

7.3.1 The specimens SST at 1150°C-1200°C

The heat treatments of these specimens are detailed in section 6.5.3i A (specimens a and b). The investigation was carried out to obtain the optimum magnetic properties using a range of solid solution temperatures.

7.3.1i The Effects of Solid Solution Temperature on $_iH_c$, B_r and BH_{max}

The variation of the intrinsic coercivity $_iH_c$ and the remanence B_r as a function of the solid solution temperature are shown in Fig. 7.6. The results are plotted for an ageing time of 15½ hours (± 5 minutes) as this corresponds to a maximum value of $_iH_c$ and B_r for the optimum solid solution temperature of 1180°C (± 5°C).

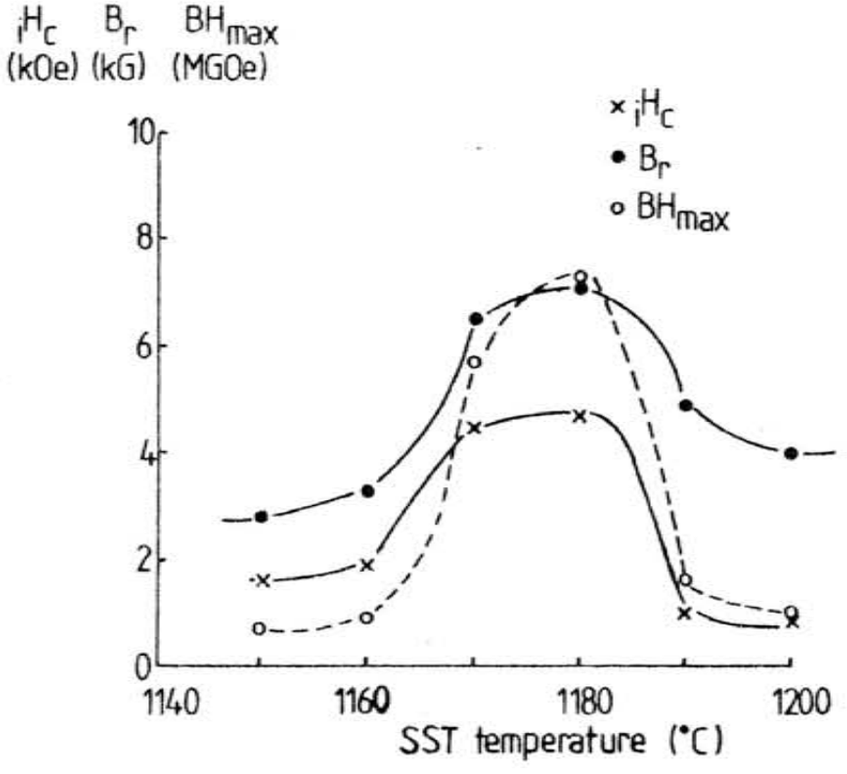

Fig. 7.6 Plots of magnetic properties versus solid solution treatment temperature for samples aged at 800°C and about 15 hours.

It can be seen that there is quite a narrow range of temperature over which the optimum magnetic properties occur, and there is quite a large increase in $_iH_c$ and B_r as the optimum solid solution temperature range is reached; this then falls quite rapidly above about 1185°C. The mid point solid solution temperature is similar to that found by Hadjipanayis (ref. 64) for a similar alloy composition. The variation in $_iH_c$ and B_r with S.S.T. temperature can be explained in terms of the presence of an optimum single phase condition which is desirable for coherent precipitate growth on ageing. Kronmuller (ref. 60) has proposed that the as-S.S.T. condition consists of a single phase 2:17-type hexagonal structure which on ageing changes to a 2:17-type rhombohedral (Th_2Zn_{17}) matrix structure with hexagonal 1:5-type precipitates.

The variation of the maximum energy product BH_{max} with S.S.T. temperature is also shown in Fig.7.6. The results are plotted for an ageing time of about 15½ hours. The shape of the BH_{max} versus S.S.T. temperature is similar to the $_iH_c$ versus SST temperature curve, but at about 1170°C there is a steep rise in the BH_{max} value, to a maximum of about 7.3 MGOe at 1180°C.

The shape of the B_r versus SST temperature plot does not show such a large fall-off above 1180°C as in the case of the $_iH_c$ and BH_{max} curves. This is possibly due to the fact that the increased density (discussed later) at the temperatures above 1180°C offset the effects of the inhomogeneities produced on solid solution treatment.

7.3.1.ii The Effects of Ageing Time on $_iH_c$, B_r and BH_{max} for Different Solid Solution Temperatures

The plots of intrinsic coercivity $_iH_c$ versus log ageing time for the different solid solution temperatures are shown in Fig. 7.7. It can be seen that for the temperatures below the optimum temperature of about 1180°C, there is a more rapid rise in $_iH_c$ up to the optimum ageing time and then a decrease. For the solid solution temperatures 1190°C and 1200°C, the variation in $_iH_c$ is much flatter and is accompanied by lower $_iH_c$ values. The optimum ageing times for the solid solution temperatures other than around 1170°C to 1180°C are lower.

This effect may be discussed in terms of the absence of a single phase condition after solid solution treatment and subsequent quenching. At the temperatures below the optimum, there is possibly some Cu-rich phase still remaining after SST, which causes a rapid growth of incoherent precipitates on ageing at 800°C. At the higher solid solution temperatures, there may be some phase segregation caused by melting, as observed by Kianvash and Harris (refs. 70, 100), thus the coherent precipitates that pin dislocations cannot fully develop at 800°C and subsequently do not become incoherent on a large scale until after long ageing times.

The plots of remanence, B_r and maximum energy product, BH_{max} versus log ageing time are shown in figures 7.8 and 7.9 respectively. The specimens S.S.T. at less than 1170°C-1180°C show a fall in B_r and BH_{max} with ageing time. The samples S.S.T. at above 1180°C show a rise in B_r and BH_{max} followed by a steady fall. The sample S.S.T. at 1180°C shows a peak in B_r and BH_{max} at about 10 hours which is shorter than the time

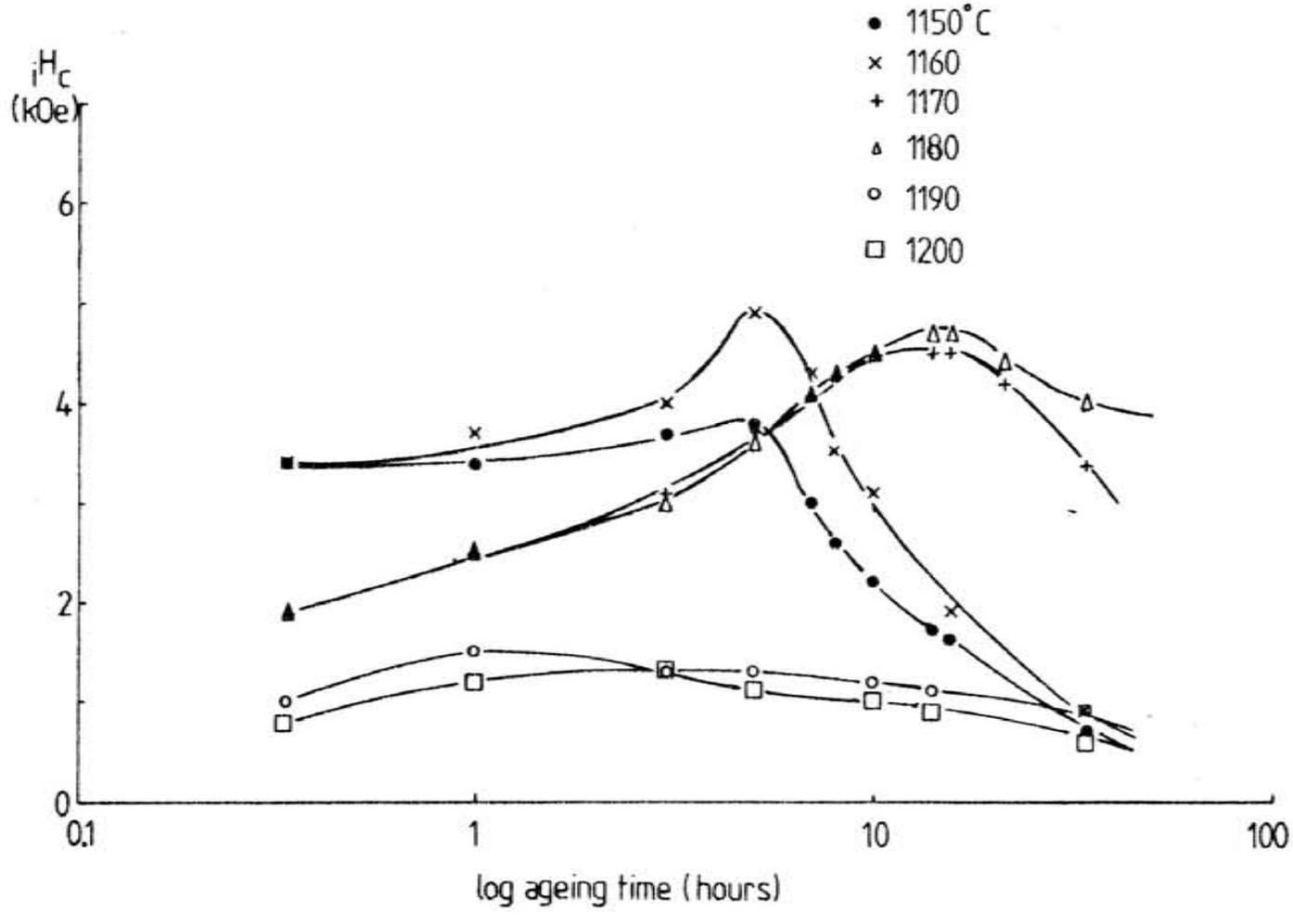

Fig. 7.7 Plots of $_{i}H_{c}$ versus log ageing time for samples SST at 1150°C-1200°C and aged at 800°C.

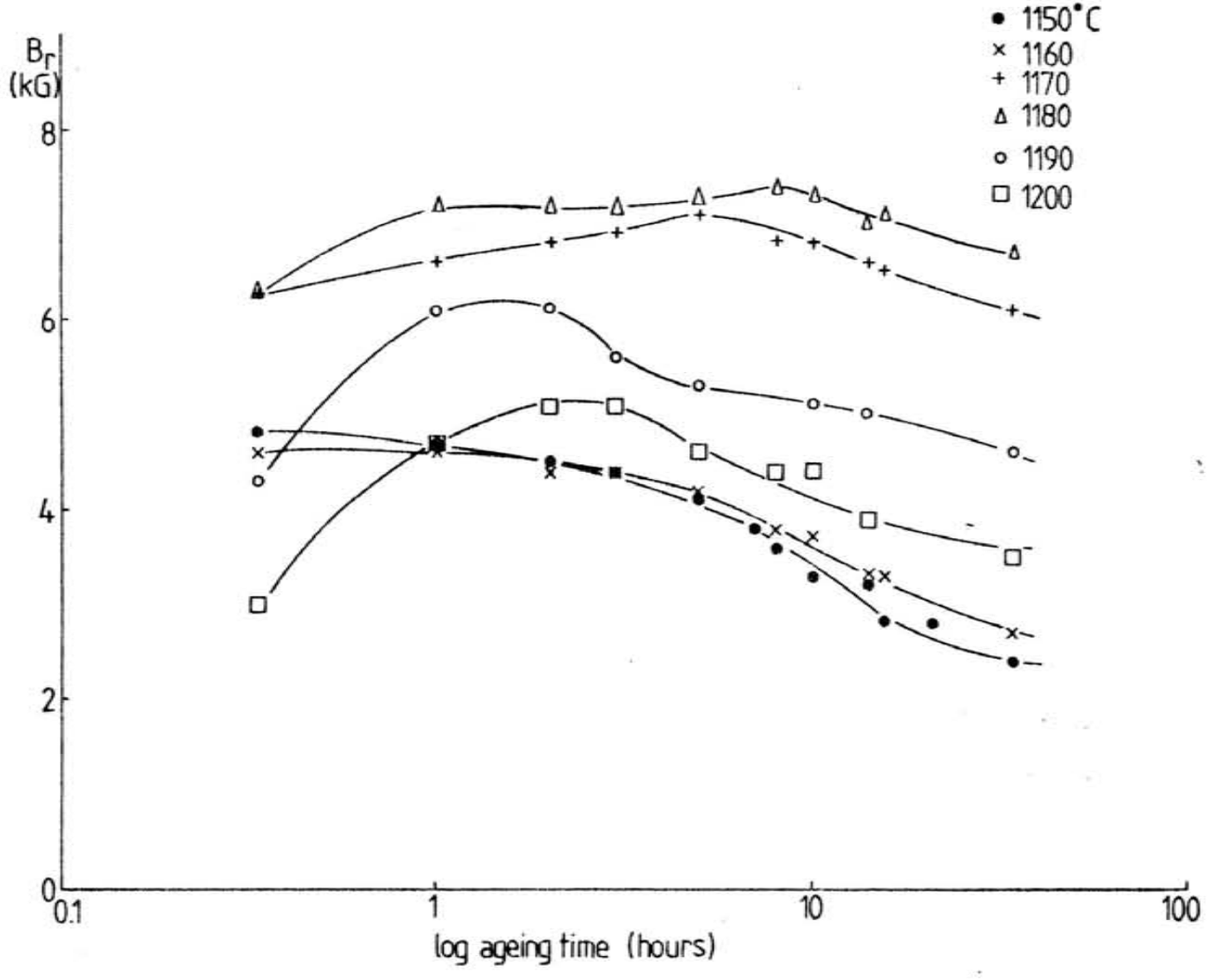

Fig. 7.8 Plots of B_r versus log ageing time for samples SST at 1150°C-1200°C and aged at 800°C.

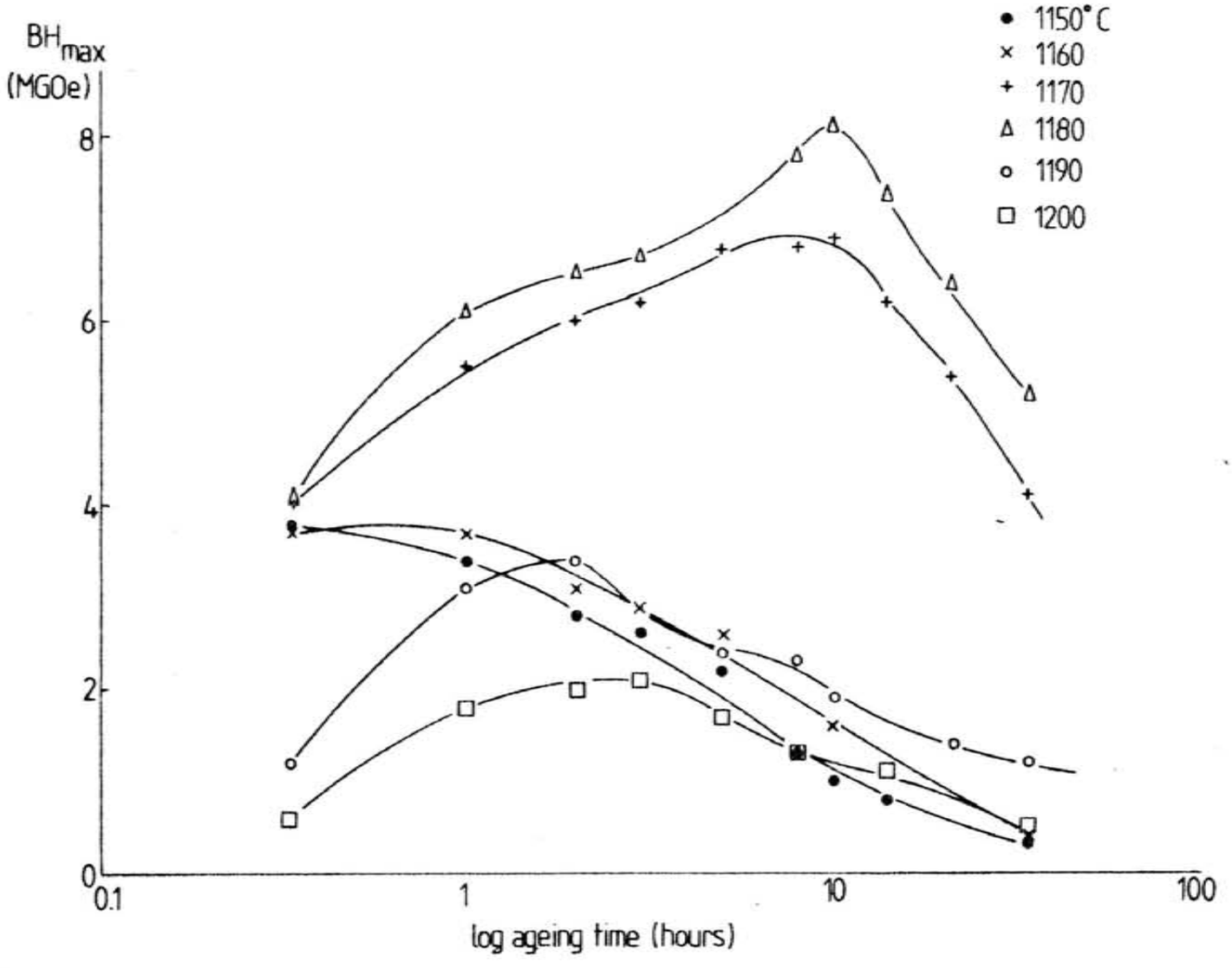

Fig. 7.9 Plots of BH_{max} versus log ageing time for samples SST at 1150°C–1200°C and aged at 800 C.

required to reach a peak in $_iH_c$. This may be attributed to the fact that as Cu goes into the 1:5 phase on ageing the matrix phase becomes relatively richer in Fe and so the magnetization of the matrix phase is higher. There is thus an increase in the remanence and therefore the BH_{max} values at an earlier ageing time. Wendi et al. (ref. 111) has found that as the Cu content increases in the 2:17-type magnets, $_iH_c$ increases (up to a certain Cu content) and B_r decreases. As the coherent Cu rich precipitates grow, there is an effect on the magnetization of the matrix and though the coercivity continues to increase, the remanence decreases.

7.3.2 The Specimens Sintered at 1190°C and then SST at 1150°C-1190°C

The heat treatments used on these specimens are detailed in Section 6.5.3i A (specimens c and d). The use of a sintering treatment is necessary so that the green compacts can achieve a high density, which in turn leads to a high B_r and BH_{max} value. The subsequent solid solution treatment is then necessary to obtain a single phase before ageing by possibly removing grain boundary segregation.

The sintering temperature of 1190°C was chosen, because above this temperature the green compacts melted and fused to the tantalum sleeve during heat treatment.

7.3.2i The Effects of Solid Solution Temperature on $_iH_c$, B_r and BH_{max} for the Pre-sintered Specimens

The variations of the intrinsic coercivity $_iH_c$, the remanence B_r and the maximum energy product BH_{max} with S.S.T. temperature are shown in Fig. 7.10. The results are plotted for an ageing time of about 15 hours as this corresponds to a maximum value of B_r and BH_{max} for an optimum solid solution temperature of about 1160°C.

As with the S.S.T. only specimens, there is a narrow range of temperature for which the magnetic properties have optimum values. The optimum solid solution temperature is about 1160°C which is lower than if the specimens had been S.S.T.-only, where the optimum temperature is 1180°C. This can be explained in terms of the time required to obtain a single phase condition during the S.S.T. The inhomogeneities produced by sintering at 1190°C are removed faster by S.S.T. at 1160°C as at this temperature there is an optimum transformation to the single phase condition during the one hour S.S.T. time interval. A further investigation is required to determine the time required at each S.S.T. temperature to achieve the optimum phase condition.

7.3.2ii The Effects of Ageing Time on $_iH_c$, B_r and BH_{max} for the Pre-sintered (PS) and S.S.T. (1150°C-1190°C) Specimens

The plots of intrinsic coercivity, $_iH_c$, versus log ageing time for the different solid solution temperatures are shown in Fig. 7.11. It can be seen that the values of $_iH_c$ all reach a maximum at about 20

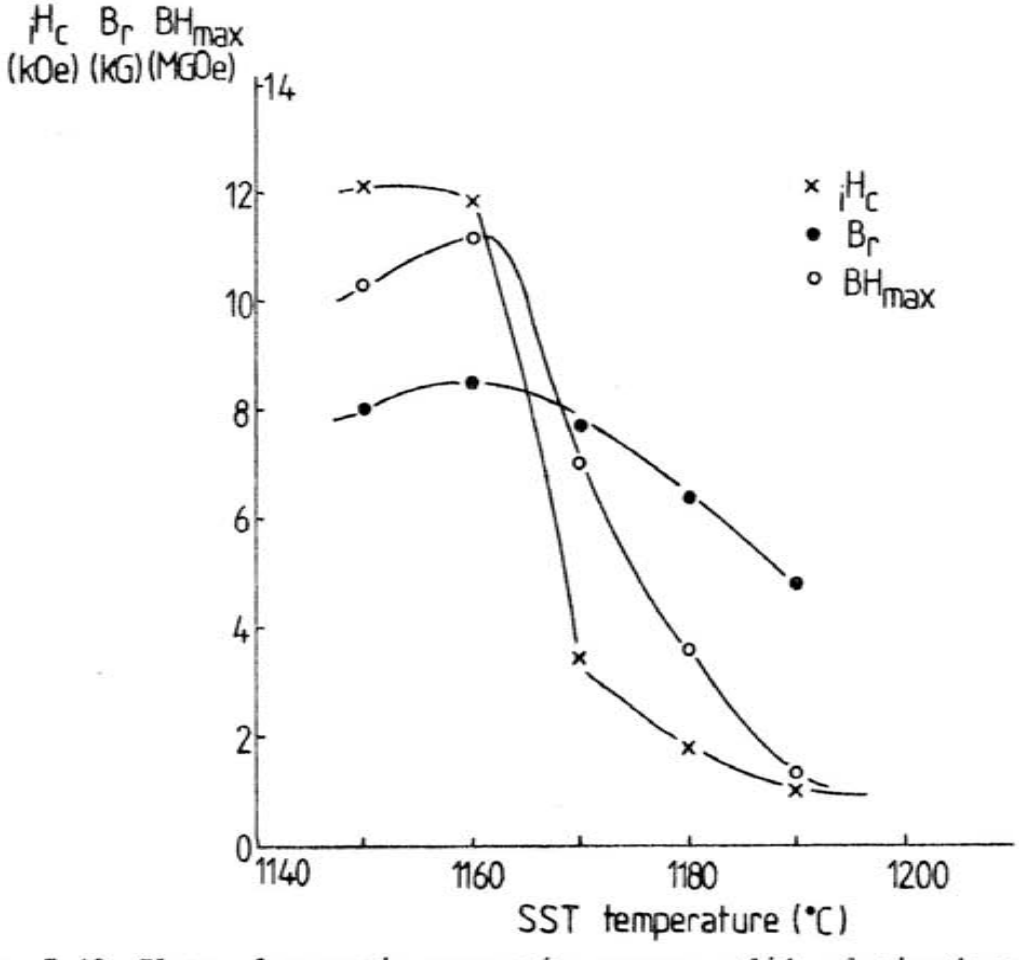

Fig. 7.10 Plots of magnetic properties versus solid solution heat treatment temperature after sintering at 1190°C; aged at 800°C for 15 hours.

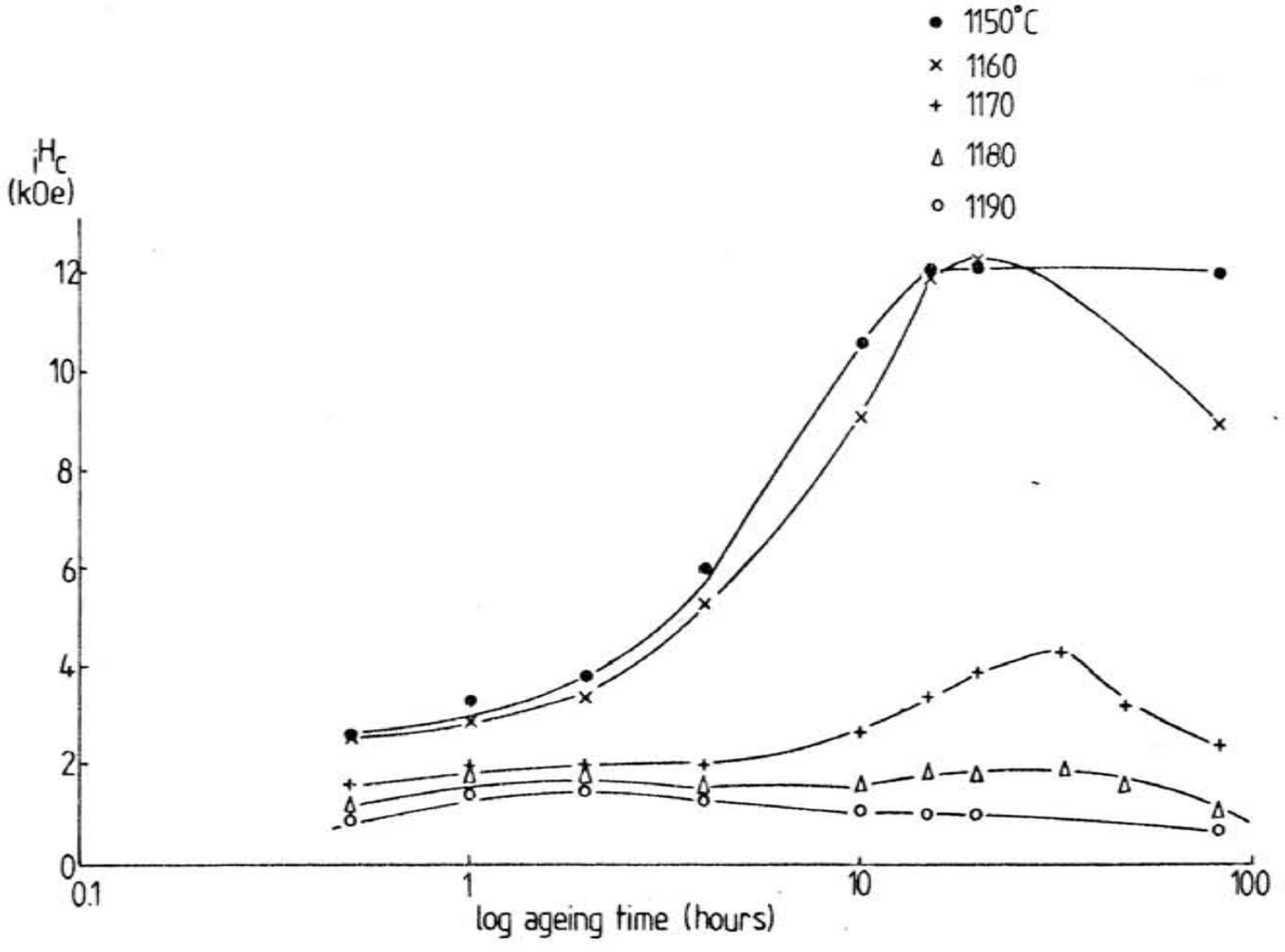

Fig. 7.11 Plots of $_{i}H_{c}$ versus log ageing time for samples pre-sintered at 1190°C and SST at 1150°C-1190°C and aged at 800°C.

to 30 hours, except for the solid solution temperature of 1190°C, in which a shallow peak $_iH_c$ value occurs at about 2 hours. The optimum solid solution temperature is at about 1160°C, and this gives a maximum coercivity of about 12.2 KOe compared with the S.S.T. only samples which gave a maximum $_iH_c$ value of about 4.7 kOe.

The higher intrinsic coercivity values may be explained in terms of the phase condition of the samples after pre-sintering (PS) and SST followed by quenching. The PS temperature of 1190°C may remove any solute segregation at grain boundaries for example so that on S.S.T. a more optimum microstructure is achieved than the SST-only samples.

The similarity in the peak ageing times may be explained by the fact that the microstructure has a similar density in all the specimens due to the same sintering temperature so that on ageing, the diffusion paths of the alloy components are similar.

The plots of B_r and BH_{max} versus log ageing time for the different S.S.T. temperatures are shown in Figs. 7.12 and 7.13 respectively. As in the case of the S.S.T.-only specimens (see Figs. 7.7, 7.8, 7.9) the values of B_r and BH_{max} reach a maximum at earlier ageing times when compared with the ageing times required to reach a peak in $_iH_c$. This may be explained in a similar way to the S.S.T.-only specimens, in that the chemical partitioning of Cu into the coherent precipitates on ageing (ref. 52) is concurrent with an increase in the magnetization of the matrix phase due to a lack of Cu which "dilutes" the magnetization. However on further ageing the distribution of the Cu-rich precipitates increases and again affects the matrix phase magnetization, even though

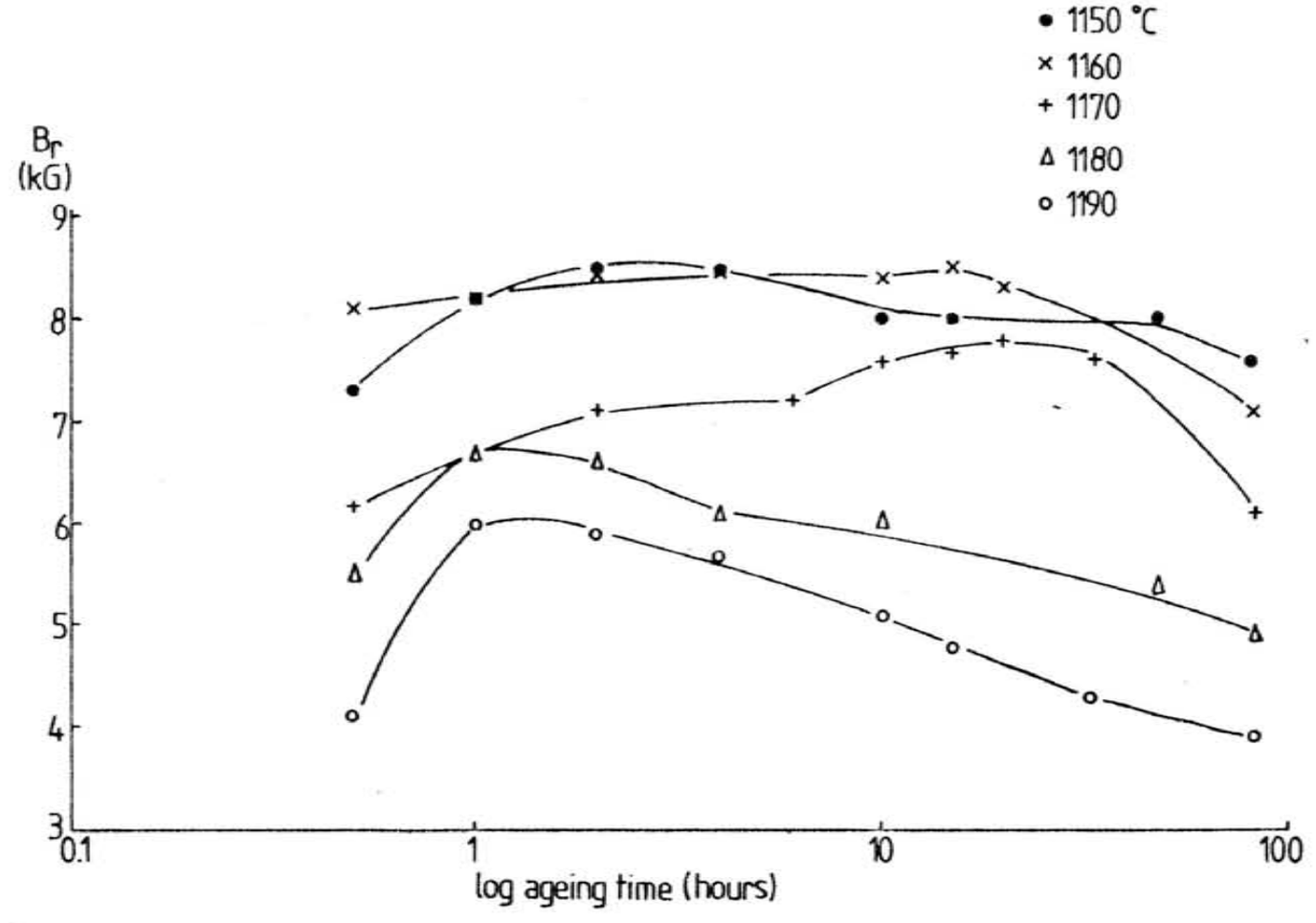

Fig. 7.12 Plots of B_r versus log ageing time for samples pre-sintered at 1190°C and SST at 1150°-1190°C and aged at 800°C.

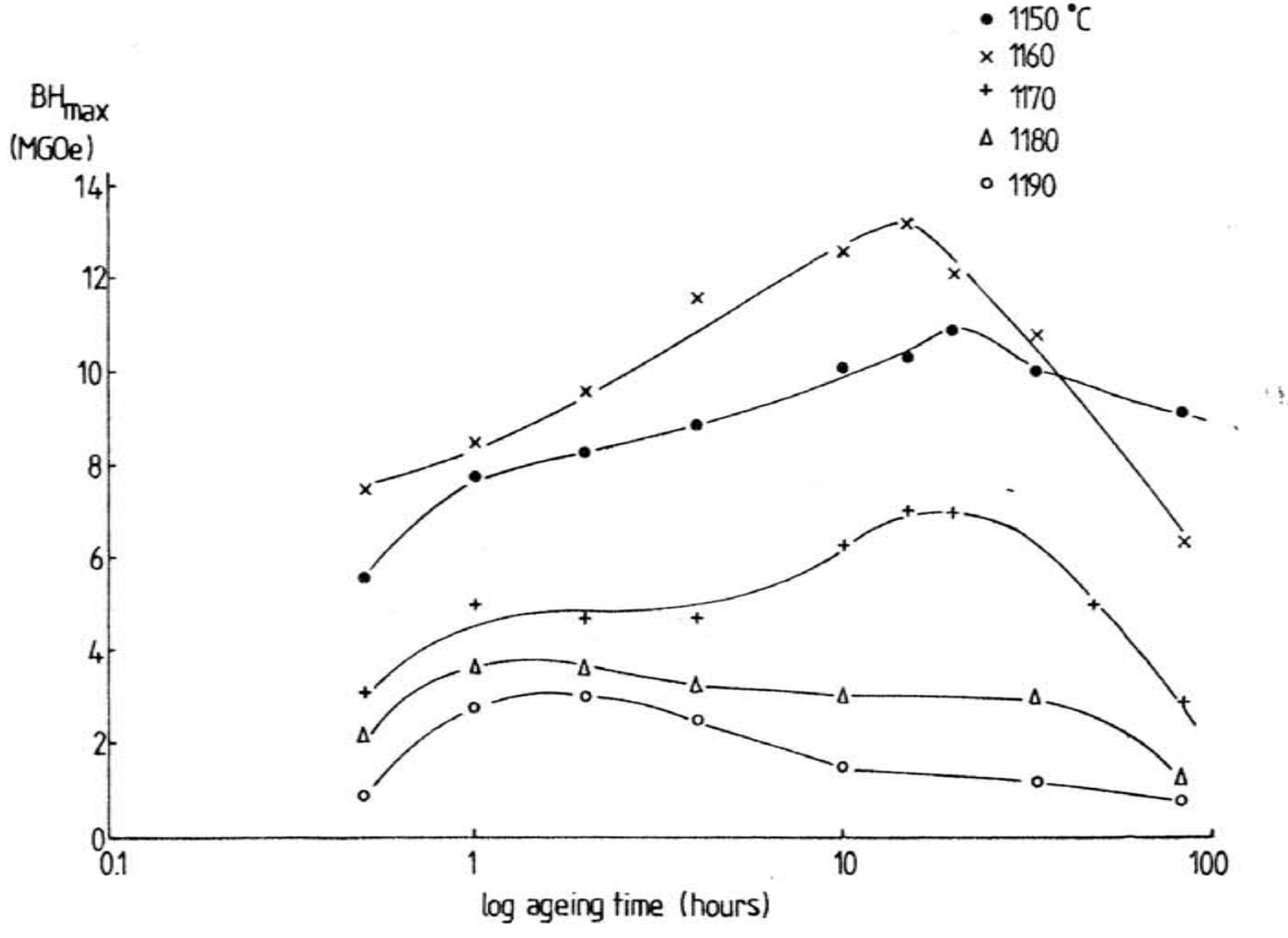

Fig. 7.13 Plots of BH_{max} versus log ageing time for samples pre-sintered at 1190°C and SST at 1150°C-1190°C and aged at 800°C.

the $_{i}H_{c}$ values continue to increase. This explanation is supported by the observation that as Cu is added to $Sm(Co,Cu,Fe,Zr)_{Z}$ alloys the intrinsic coercivity increases, but B_{r} decreases, and the amounts of the Cu-rich coherent 1:5-type precipitates increase (ref. 111).

7.3.2iii The Effects of Ageing Time on the Loop Shapes for the PS and S.S.T. (1150°C-1190°C) Specimens

The changes in loop shape during isothermal ageing at 800°C were studied for these particular specimens to show how the coherent precipitates produced on ageing become less effective domain pinning sites as they become incoherent. This is indicated by the change in the "squareness" of theB-H versus H plot.

The loop shape plots are shown in Figs. 7.14 and 7.15 for the S.S.T. temperatures of 1160°C and 1180°C respectively. At the optimum ageing time of 15 to 20 hours (Fig. 7.14) the loops are quite elongated. At an ageing time of about 81 hours, the shape of the curve is more convex, this can be explained by the gradual growth of incoherent precipitates in the matrix which do not pin domains, so that there is a more rapid fall in B-H with applied field.

7.3.3 The Specimens SST at 1170°C and aged at 800°C-900°C

This investigation was undertaken to study the effects of ageing temperature on the development of the magnetic properties. A similar study has been done by Daku and Yujin (ref. 77) but on an alloy of composition $Sm(Co_{0.69}Cu_{o.1}Fe_{0.2}Zr_{0.01})_{7.5}$.

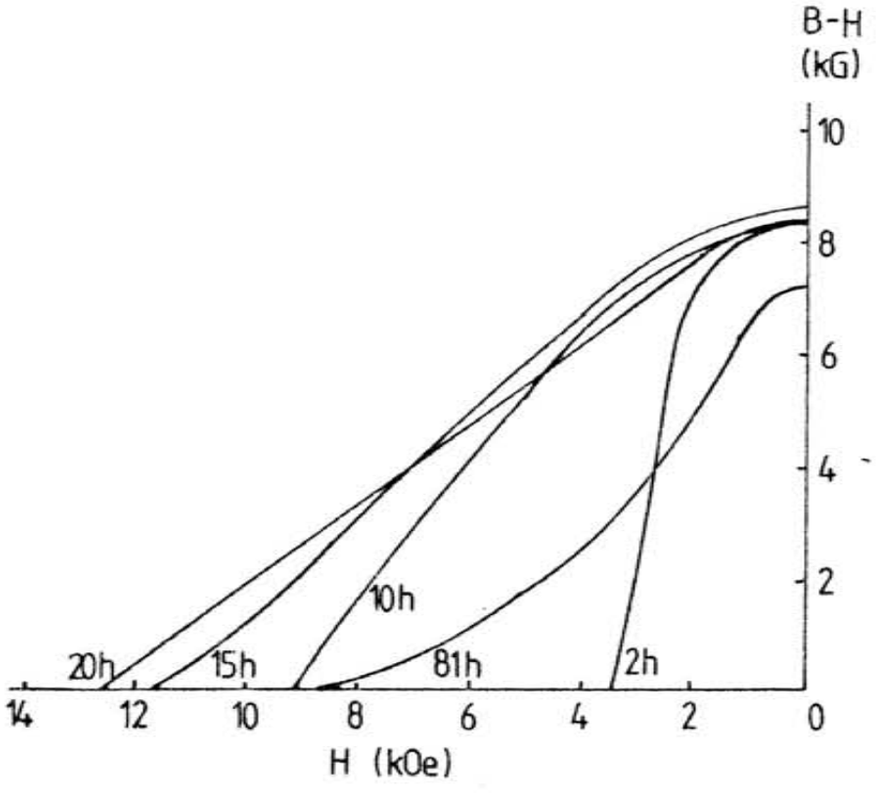

Fig. 7.14 Second quadrant loop shapes for PS at 1190°C and SST at 1160°C and aged at 800°C sample for different ageing times.

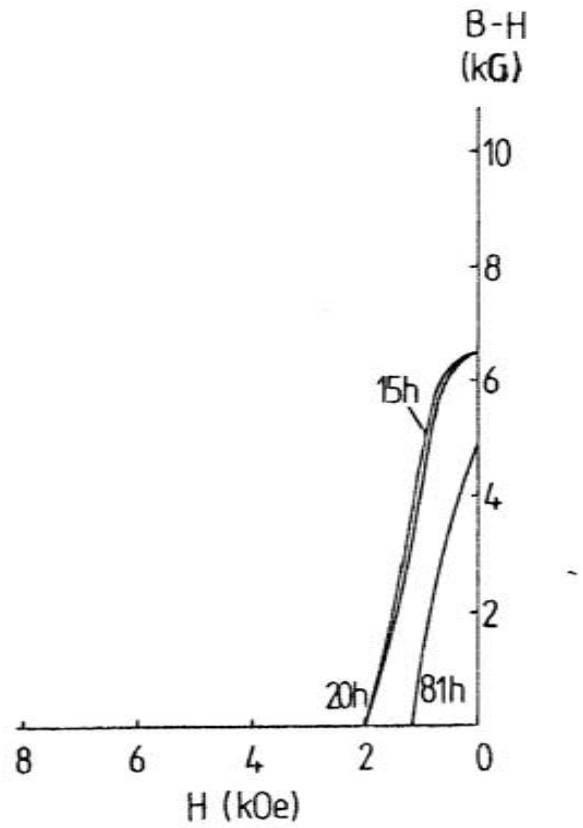

Fig. 7.15 Second quadrant loop shapes for PS at 1190°C and SST at 1180°C and aged at 800°C sample for different ageing times.

7.3.3.i The Effects of Ageing Temperature on $_iH_c$, B_r and BH_{max}

The variation of $_iH_c$ against log ageing time is shown in Fig. 7.16. The peak $_iH_c$ value occurs at about 15 hours for an ageing temperature of 800°C. Above this temperature, the times required to reach a peak coercivity decrease with increasing ageing temperature. These times are much longer than has been found by Daku and Yujin (ref. 77); but are similar to those found by Yoneyama et al. (ref. 65). This could indicate that Daku and Yujin may have used a different processing technique involving starting powders of a similar size but different heating and/or cooling rates.

The decreasing peak heights of $_iH_c$ ageing times with increasing ageing temperature, may be explained by considering the precipitation process of the Cu-rich phase. As the ageing temperature increases, the precipitates grow at a higher rate and so an overageing phenomena occurs more rapidly. At an ageing temperature of 900°C there is little time for the steady growth of Cu enriched precipitates before overageing occurs, so that there is only a small increase in $_iH_c$ before the peak ageing time. Alternatively, as discussed in Section 7.12.2, the absence of the Zr-rich phase in the sample aged at 900°C may be concurrent with the lower $_iH_c$ values.

The ageing temperature between 800°C and 850°C did not have a large effect on the maximum $_iH_c$ values. However, there was a large effect on the B_r and BH_{max} values due possibly to the rapid overageing of the Cu-rich precipitates or alternatively due to the Cu being maintained in the matrix due to an increased solubility at temperatures above 800°C (ref. 104) with no chemical partitioning (ref. 60). The plots of B_r and BH_{max} versus log ageing time are shown in Figs. 7.17 and 7.18 respectively for the ageing temperatures of 800°C, 830°C and 900°C.

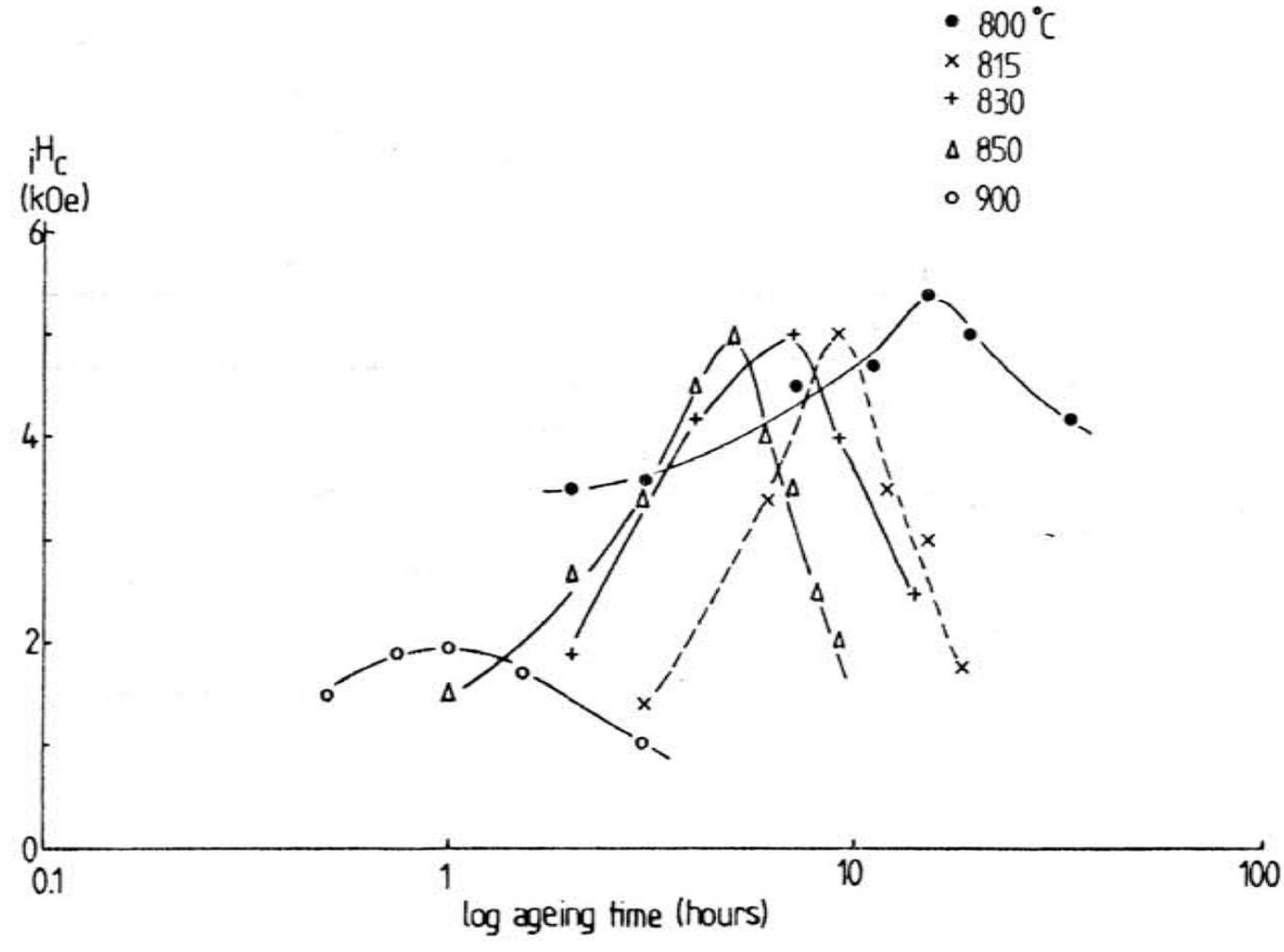

Fig. 7.16 Plots of $_{i}H_{c}$ versus log ageing time for samples SST at 1170°C and aged at 800°C-900°C.

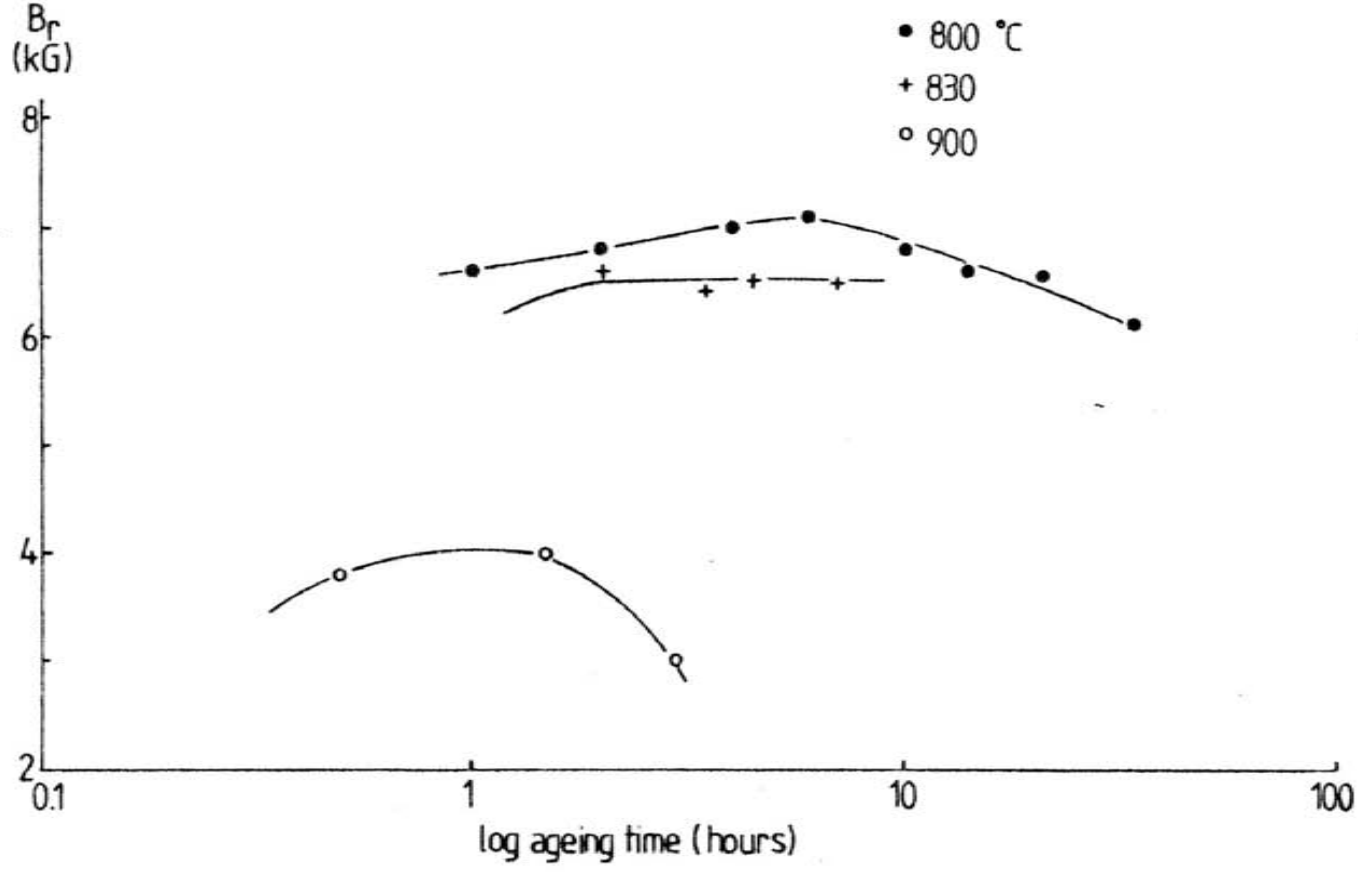

Fig. 7.17 Plots of B_r versus log ageing time for samples SST at 1170°C and aged at 800°C-900°C.

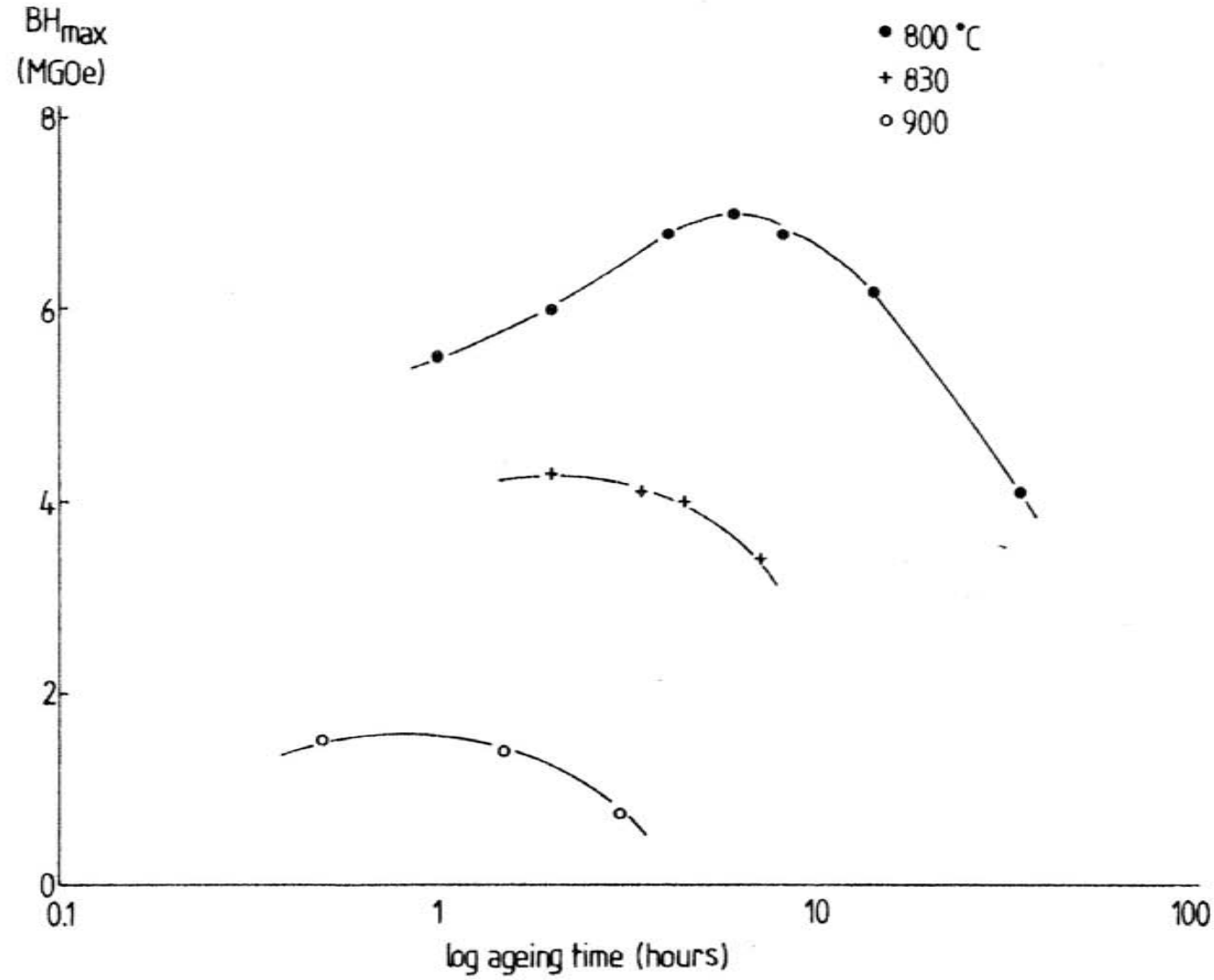

Fig. 7.18 Plots of BH_{max} versus log ageing time for samples SST at 1170°C and aged at 800°C-900°C.

7.3.4 The Effects of Step Ageing on $_iH_c$, B_r and BH_{max}

It has been noted that on step ageing after the S.S.T. (ref. 52), Cu partitioning occurs in which Cu enters into the coherent 1:5 type precipitate phase producing a consequent increase in the magnetic properties (ref. 65).

Thus, a step ageing treatment was attempted in this investigation in an attempt to show a similar improvement in the magnetic properties.

The heat treatment used is detailed in section 6.5.3iA (specimen e), and is one used by other workers for a similar alloy (see for example, ref. 112). The magnetic properties achieved are shown in Table 7.1a and are compared with those of a similar sintered but isothermally aged sample. Allowing for error, the $_iH_c$ and B_r values for the isothermally aged and step aged samples are similar. There is an improvement in the energy product, and these results agree with the increases seen in a similar alloy on multiple step ageing (ref. 112).

Table 7.1a Comparison of isothermally aged and step aged magnetic properties.

Isothermally aged:heat treatment detailed in section:6.53iAi		Step aged:heat treatment detailed in section:6.5.3iA1
$_iH_c$ (kOe)	3.9 ± 0.2	3.7 ± 0.2
B_r (kG)	7.8 ± 0.2	7.9 ± 0.2
BH_{max} (MGOe)	7.0 ± 0.4	9.6 ± 0.4

7.4 Magnetic Properties of the Sintered Specimens produced from Hydrogen Decrepitated (HD) and Ball Milled Powder

7.4.1 The Specimens S.S.T. at 1160°C-1190°C

All the heat treatments carried out on these specimens are detailed in section 6.5.3iB (specimens a and b), and are the same as those done on the ball milled only material so that a comparison of the relative magnetic properties could be made.

7.4.1i The Effects of Solid Solution Temperature on $_iH_c$, B_r and BH_{max}

The variations of $_iH_c$, B_r and BH_{max} as a function of solid solution temperature are shown in fig. 7.19. The results are plotted for an ageing time of about 15½ hours as this corresponds to a maximum value of $_iH_c$, B_r and BH_{max}, for the optimum solid solution temperature of about 1180°C.

The forms of the plots show a similar pattern to the ball milled only material shown in fig. 7.6. This may again be explained in terms of achieving the optimum single phase condition during solid solution treatment. The values of intrinsic coercivity with S.S.T. temperature are approximately the same for the ball milled material and the HD material. The remanence values are however lower in the HD material which is expected due to the larger particle size as discussed in section 7.2.3. which leads to lower densities. The particle size does not have a large effect on the $_iH_c$ values however as the coercivity mechanism is one of domain pinning rather than the nucleation of reverse domains at particle surfaces (ref. 10).

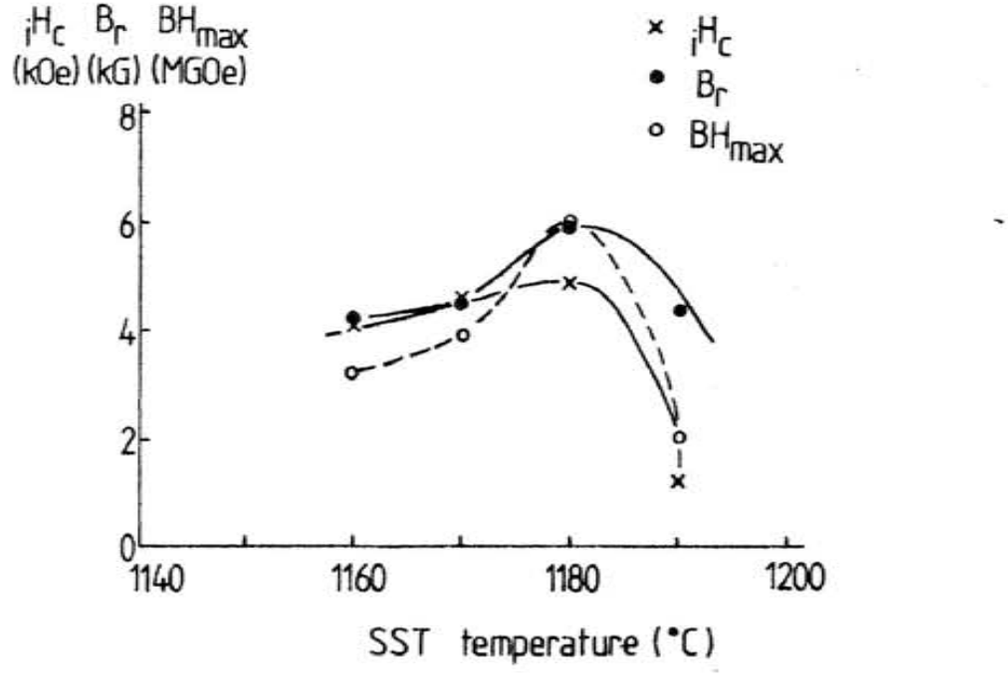

Fig. 7.19 Plots of magnetic properties versus SST for HD samples aged at 800°C for 15 hours.

7.4.1ii The Effects of Ageing Time on $_iH_c$, B_r and BH_{max} for different Solid Solution Temperatures

The plots of $_iH_c$ versus log ageing time for the different solid solution temperatures are shown in Fig. 7.20. The peak $_iH_c$ value occurs for the S.S.T. temperature of about 1180°C and at an ageing time in the range 15 to 25 hours. It can be seen that the increases in $_iH_c$ with ageing time throughout the S.S.T. temperature range are more gradual than in the case of the BMO specimens (see Fig. 7.7). This may be explained in terms of the larger particle size of the HD and ball milled material when compared with the BMO material. This is supported by the results of Kianvash (ref. 100) who showed that a peak $_iH_c$ value occurred at an ageing time of about 35 hours, when ageing at a temperature of 800°C; the powder used in the investigation was hand-ground and so would be expected to be larger than the ball milled and HD and ball milled powders used in this study. The longer ageing times found by Kianvash may also be due to a slightly different alloy composition.

The larger particle sizes of the starting powder used in the green compact may result in longer ageing times being required due to the formation of the coherent precipitates responsible for domain pinning taking longer to develop to an optimum size due to the larger distances along grain boundaries involved for the diffusion of the alloy components that constitute the coherent phase. In terms of the magnetic properties, a smaller particle size is desirable as this leads to a larger remanence due to an increased density after sintering and to shorter ageing times being required to achieve the optimum intrinsic coercivity.

The plots of B_r and BH_{max} versus log ageing time for the HD material are shown in figs. 7.21 and 7.22 respectively. The variations of B_r and BH_{max} with ageing time do not show such a large change as in the case of the BMO material (see figs.7.8 and 7.9). However, the peak values of B_r and BH_{max} do occur at earlier ageing times than for the peaks in $_iH_c$. This may be explained again in terms of the Cu content in the matrix and coherent precipitates detailed in sections 7.3.1ii and 7.3.2ii.

7.4.2 The HD Specimens Sintered at 1190°C and then S.S.T. at 1160-1190°C

The heat treatments used on these specimens are detailed in section 6.5.3iB (specimens c and d).

7.4.2i The Effects of Solid Solution Temperature on $_iH_c$, B_r and BH_{max} for the PS HD Specimens

The variations of $_iH_c$, B_r and BH_{max} with S.S.T. temperature are shown in fig. 7.23. The results are plotted for an ageing time of about 20 hours, which corresponds to the peak magnetic properties achieved for a S.S.T. temperature of about 1160°C.

The plots follow a similar pattern to the BMO material (see Fig. 7.10), and the same explanation for the variations may be applied to these specimens. Thus, on cooling from the sintering temperature of 1190°C, a single phase structure is achieved more rapidly at the S.S.T. temperature of 1160°C than for higher temperatures. The optimum single

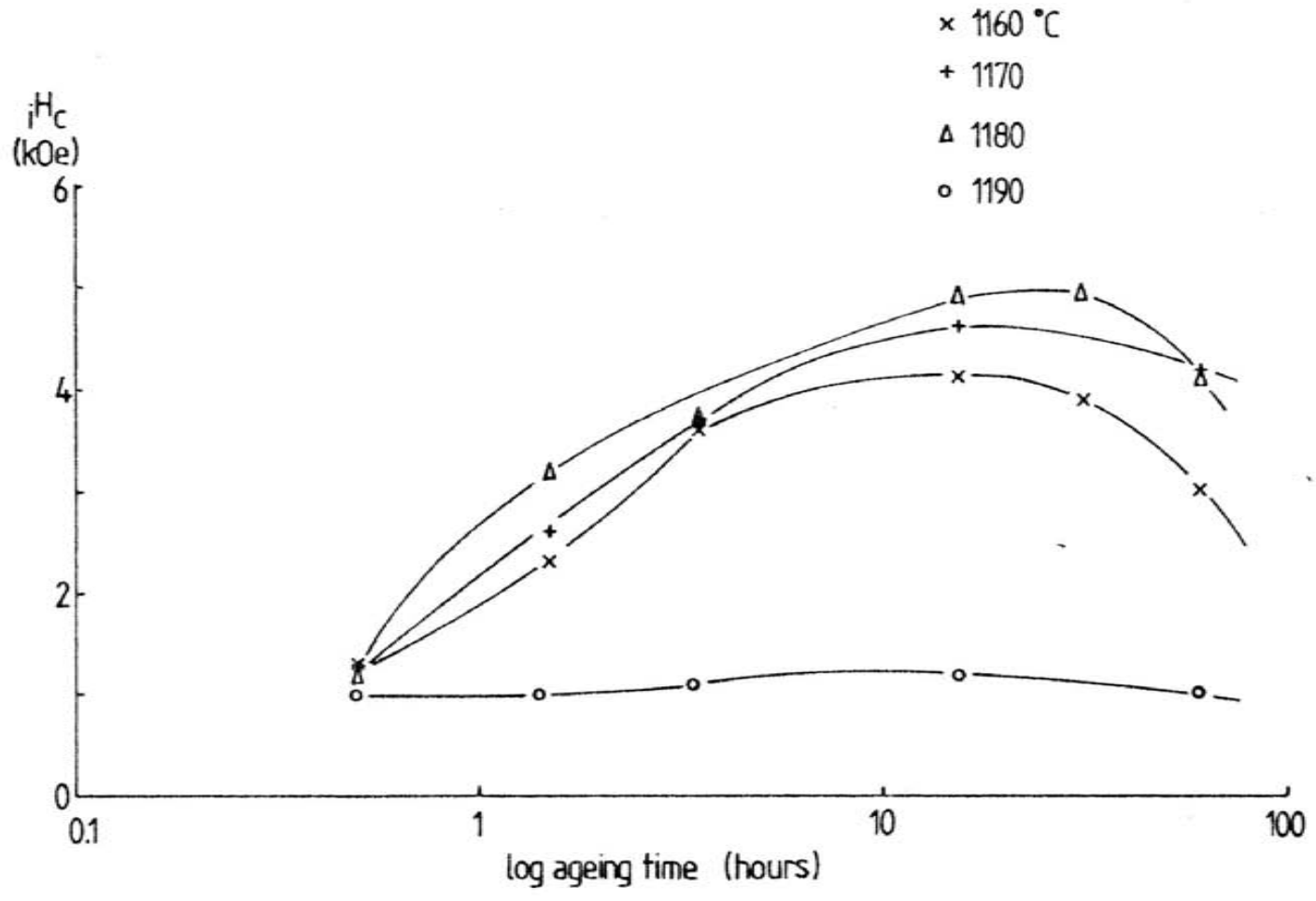

Fig. 7.20 Plots of $_iH_c$ versus log ageing time for HD samples SST at 1160°C-1190°C and aged at 800°C.

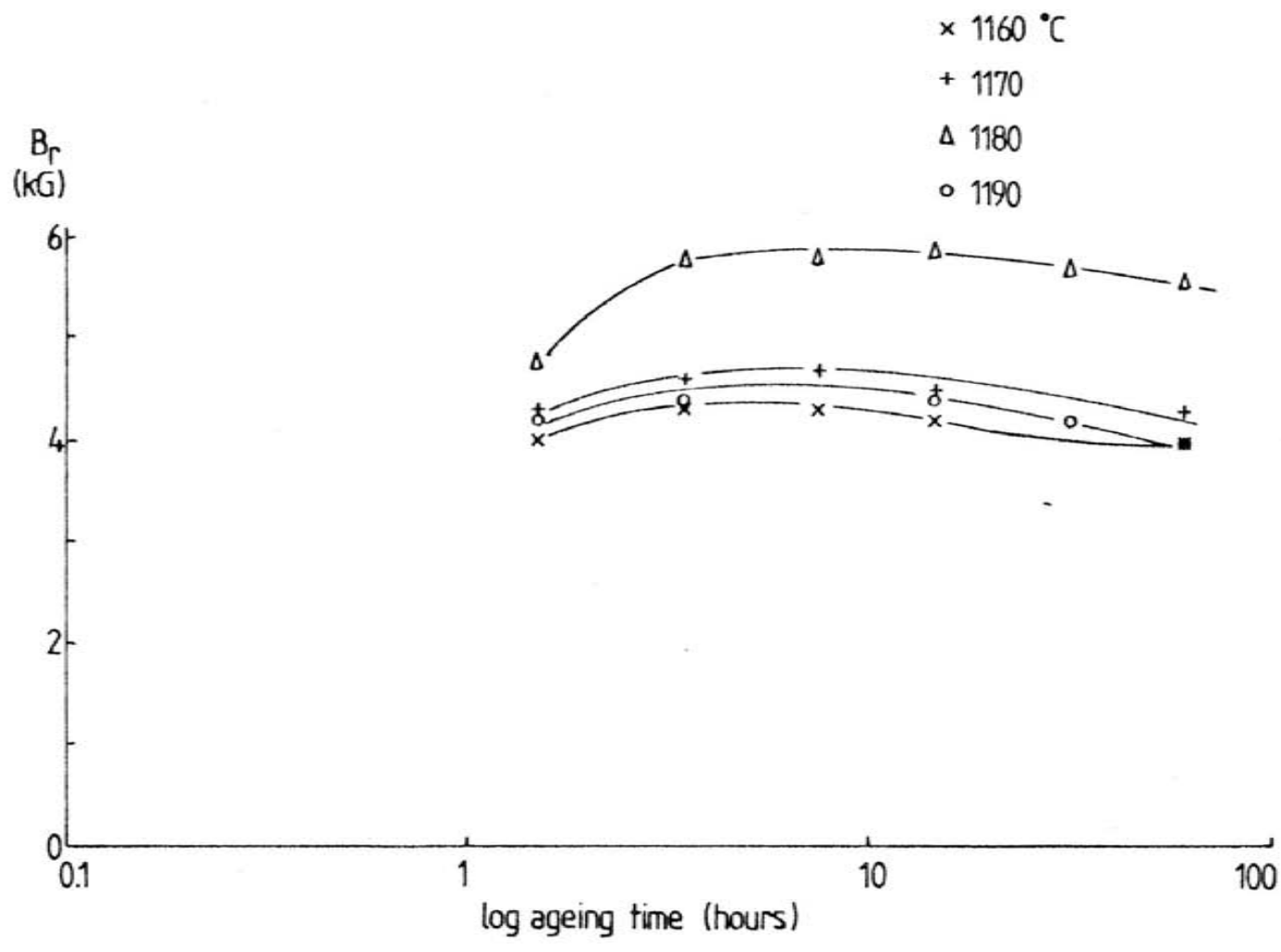

Fig. 7.21 Plots of B_r versus log ageing time for HD samples SST at 1160°C-1190°C and aged at 800°C.

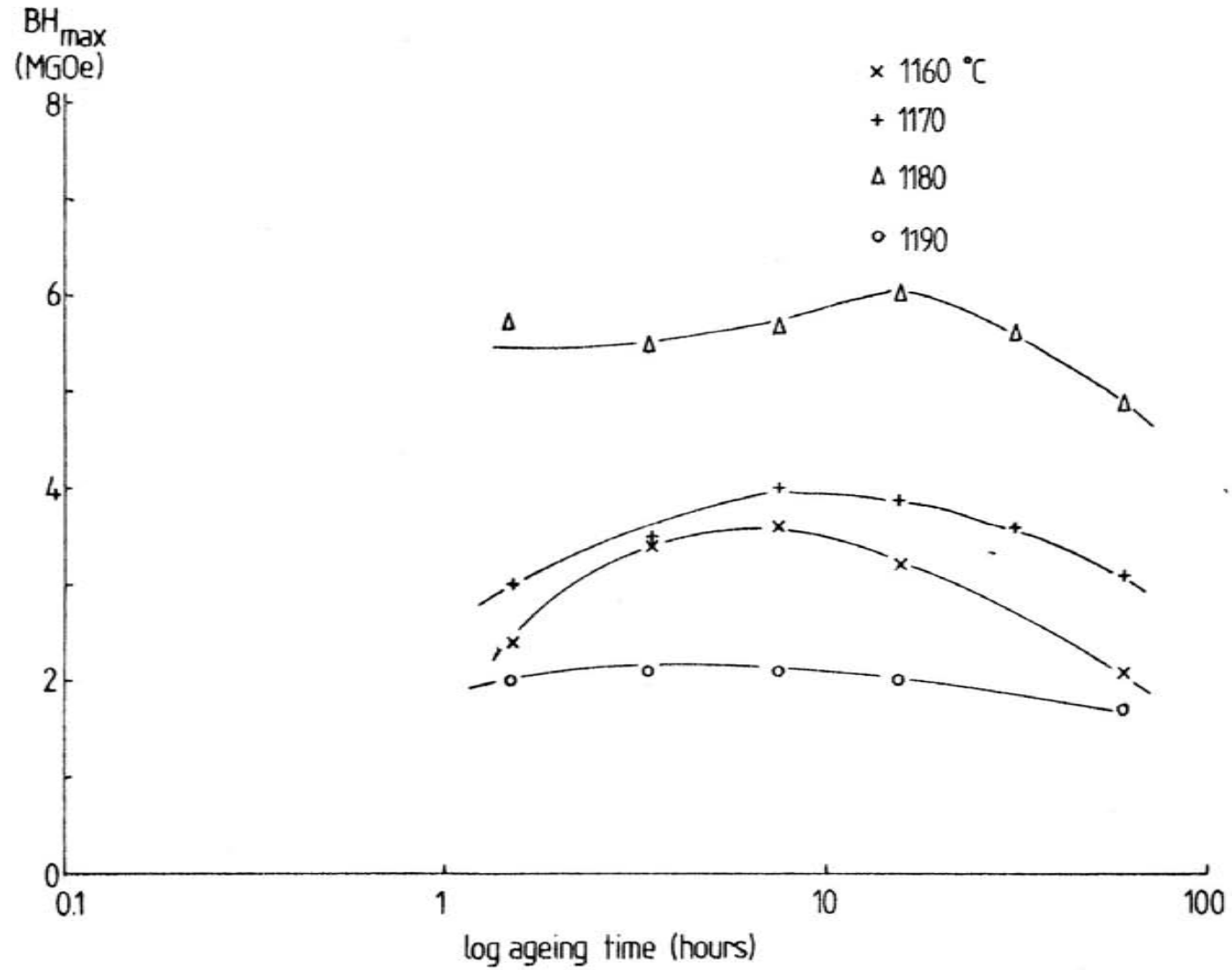

Fig. 7.22 Plots of BH_{max} versus log ageing time for HD samples SST at 1160°C-1190°C and aged at 800°C.

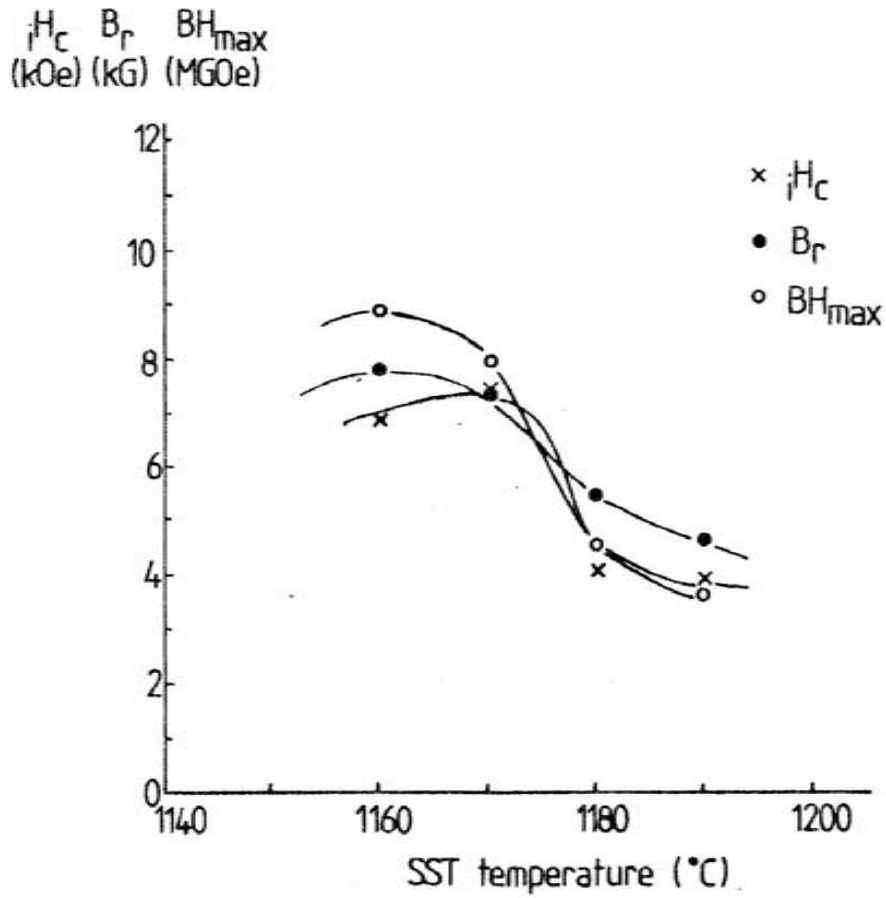

Fig. 7.23 Plots of magnetic properties versus SST temperature for PS at 1190°C and aged at 800°C for 15 hours HD samples.

phase structure may be achieved at temperatures above 1160°C but at longer S.S.T. times.

The peak values of B_r for the HD specimens are lower than the ball milled only specimens, which supports the larger particle size of the starting material in the HD material.

7.4.2ii The Effects of Ageing Time on $_iH_c$, B_r and BH_{max} for different Solid Solution Temperatures

The plots of $_iH_c$, B_r and BH_{max} versus log ageing time are shown in figs. 7.24, 7.25 and 7.26 respectively. The shapes of the curves are similar to those in figs. 7.20, 7.21 and 7.22 for the S.S.T. only specimens. However, the ageing times at which the peak magnetic properties occur are much broader, and there is little discrepancy between the ageing times required to reach the maximum values of $_iH_c$, B_r or BH_{max}.

These results may be explained in terms of the large particle size of the HD material and the fact that the diffusion distances are larger during isothermal ageing.

7.5 Density Measurements on the Sintered Samples

The density measurements provided information on the sintered samples, in terms of the extent of sintering and the initial particle size of the starting powder.

The bulk denisty was found to be: 8.2 kgm^{-3} (± 0.2 kgm^{-3})

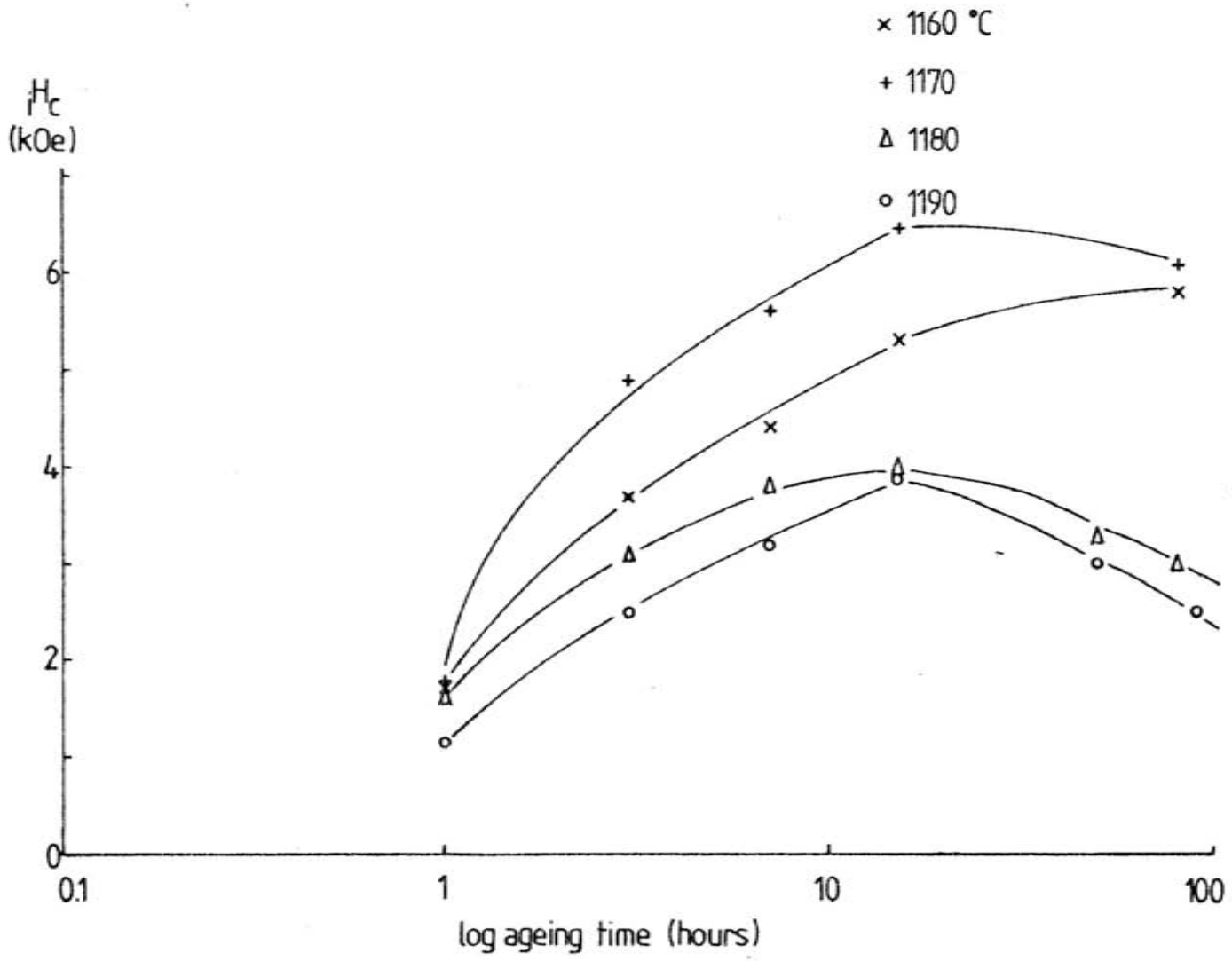

Fig. 7.24 Plots of $_iH_c$ versus log ageing time for HD samples PS at 1190°C and SST at 1160°C-1190°C and aged at 800°C.

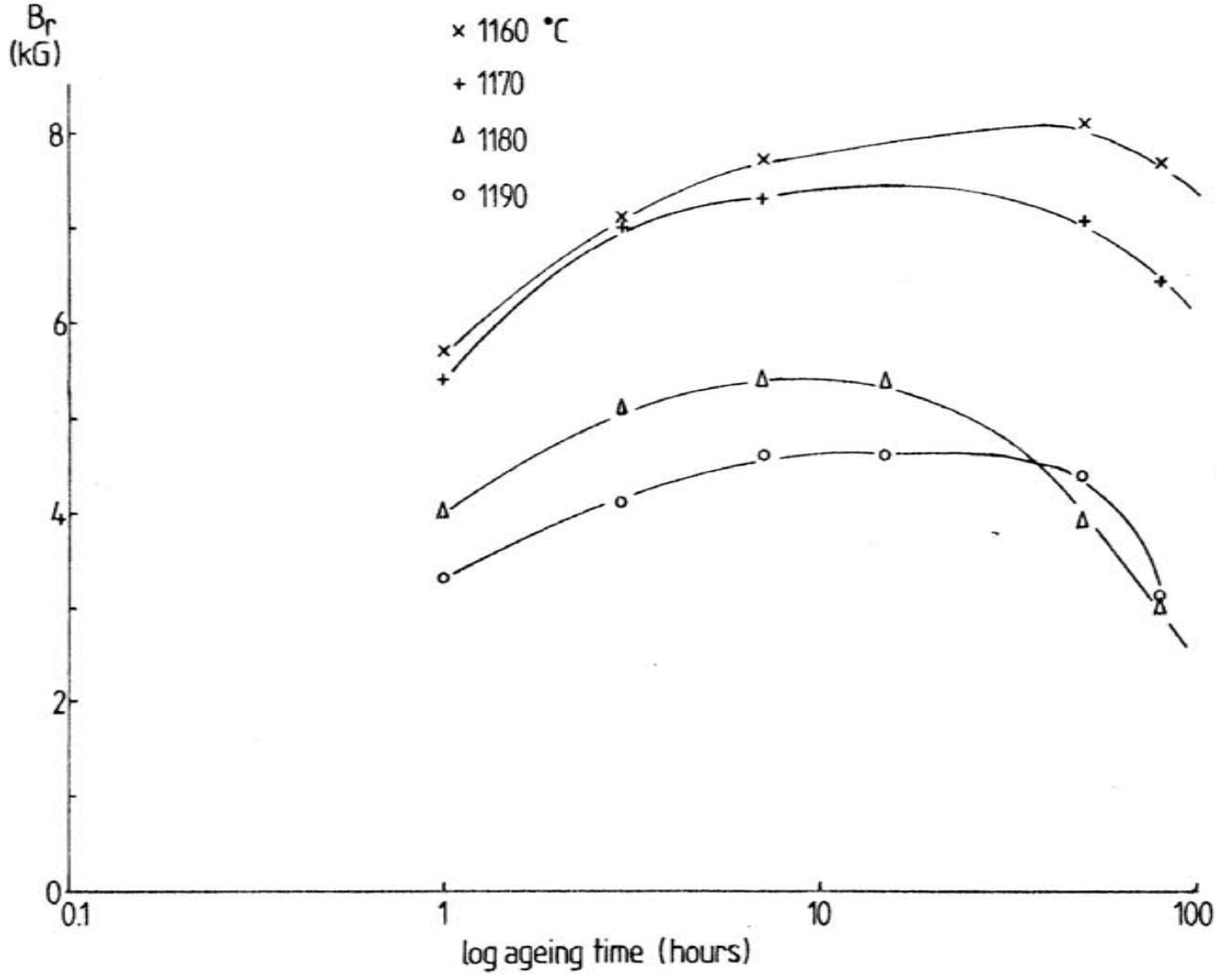

Fig. 7.25 Plots of B_r versus log ageing time for HD samples PS at 1190°C and SST at 1160°C-1190°C and aged at 800°C.

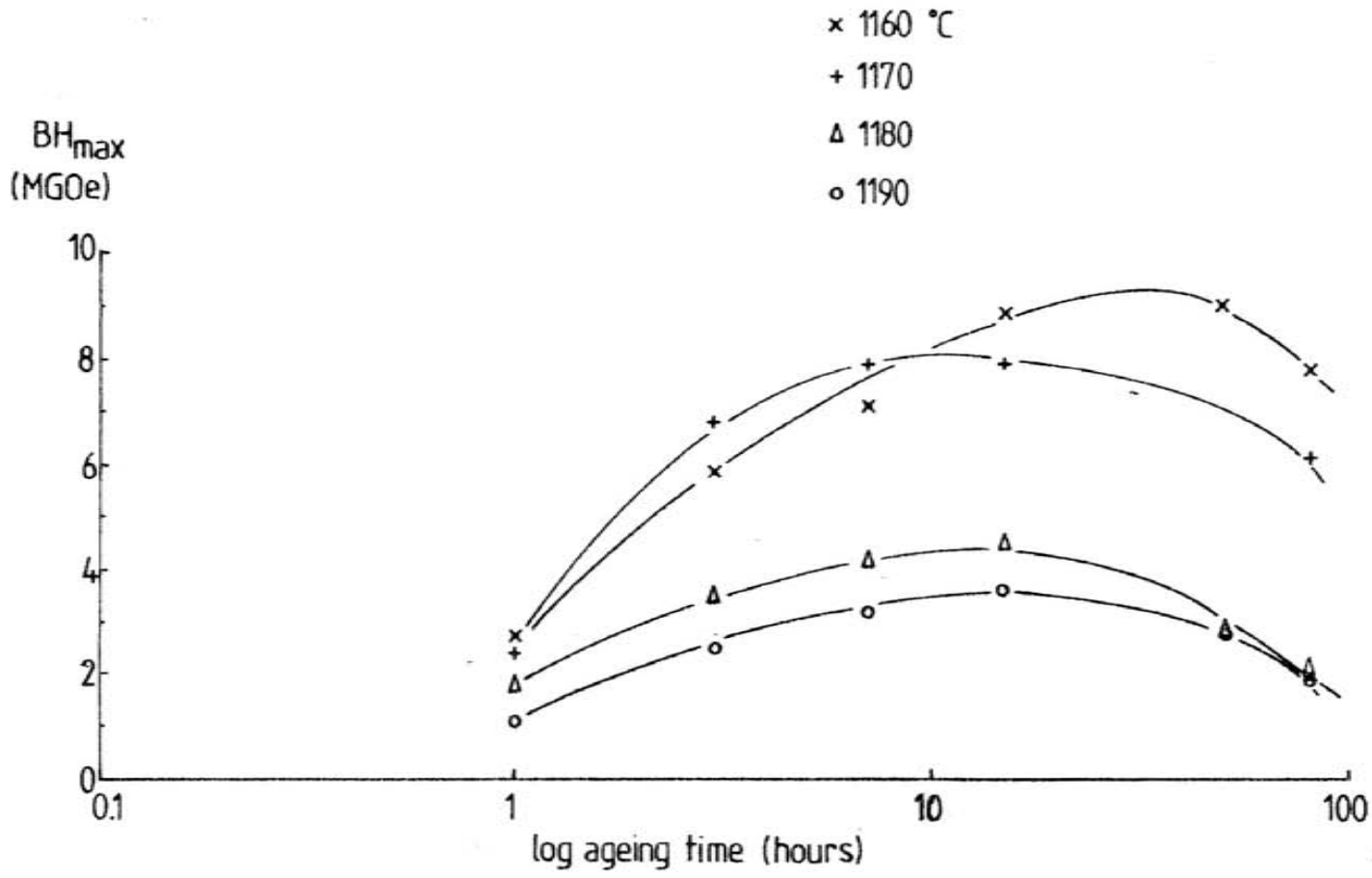

Fig. 7.26 Plots of BH_{max} versus log ageing time for HD samples PS at 1190°C and SST at 1160°C-1190°C and aged at 800°C.

7.5.1 Density Measurements on the BMO Material for the Specimens S.S.T. Treated at 1150°C-1200°C, and Pre-sintered at 1190°C and then S.S.T. Treated at 1150-1190°C

The densities of the specimens S.S.T. at different temperatures in the range 1150°C-1200°C for one hour and then quenched are shown in figure 7.27. The densities of the specimens pre-sintered (PS) at 1190°C for one hour and then S.S.T. in the range 1150°C-1190°C are also shown in fig. 7.27.

Allowing for errors, the S.S.T. only specimens show an increase with S.S.T. temperature and this levels out at about 1190°C to 1200°C. This rise in density is expected, since as the temperature increases, the driving force for densification is increased and some particle surface melting occurs.

The densities of the PS specimens are (allowing for errors) essentially constant throughout the S.S.T. temperature range. This is expected as a single sintering temperature was used (1190°C) and the density values agree well with the specimen S.S.T. at 1190°C only.

7.5.2 Density Measurements on the Hydrogen Decrepitated and Ball Milled Material For the Specimens S.S.T. at 1160°C-1190°C and PS at 1190°C and then S.S.T. at 1160°C-1190°C

The densities of the specimens produced from HD and then ball milled material are shown in fig. 7.28 as a function of S.S.T. temperature. The densities of the specimens PS at 1190°C and then S.S.T. are also shown in fig. 7.28.

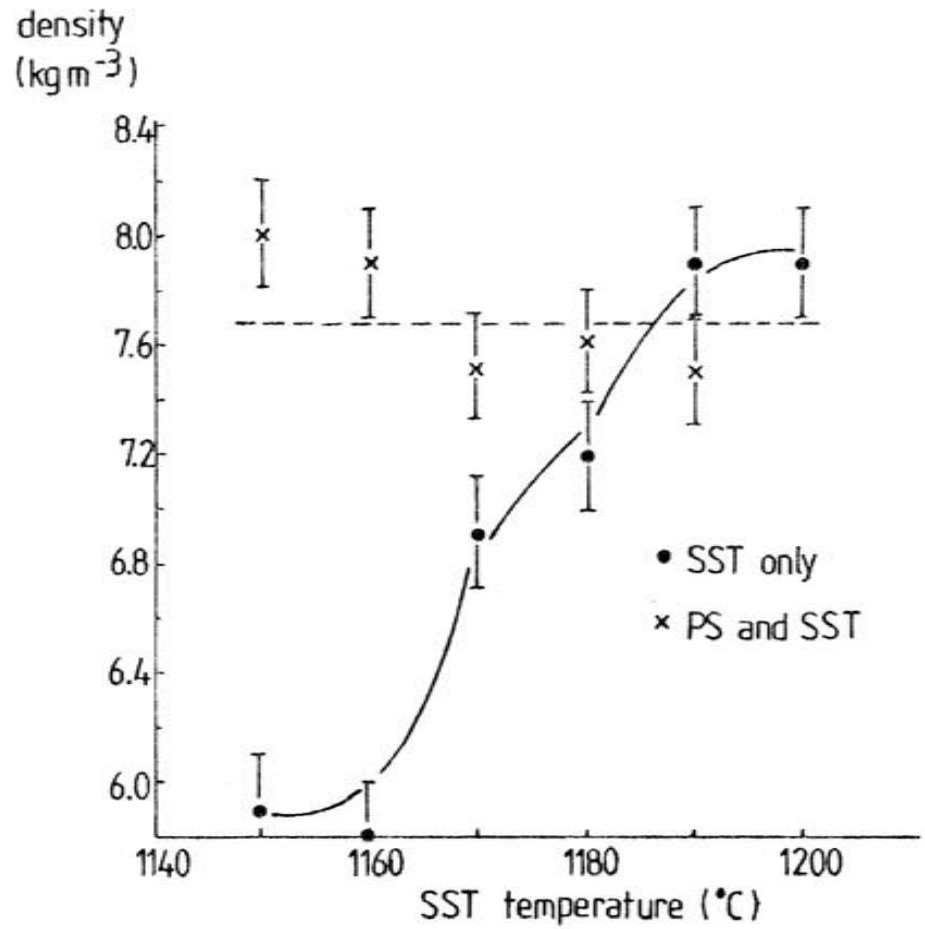

Fig. 7.27 Plots of density for PS at 1190°C and SST only samples.

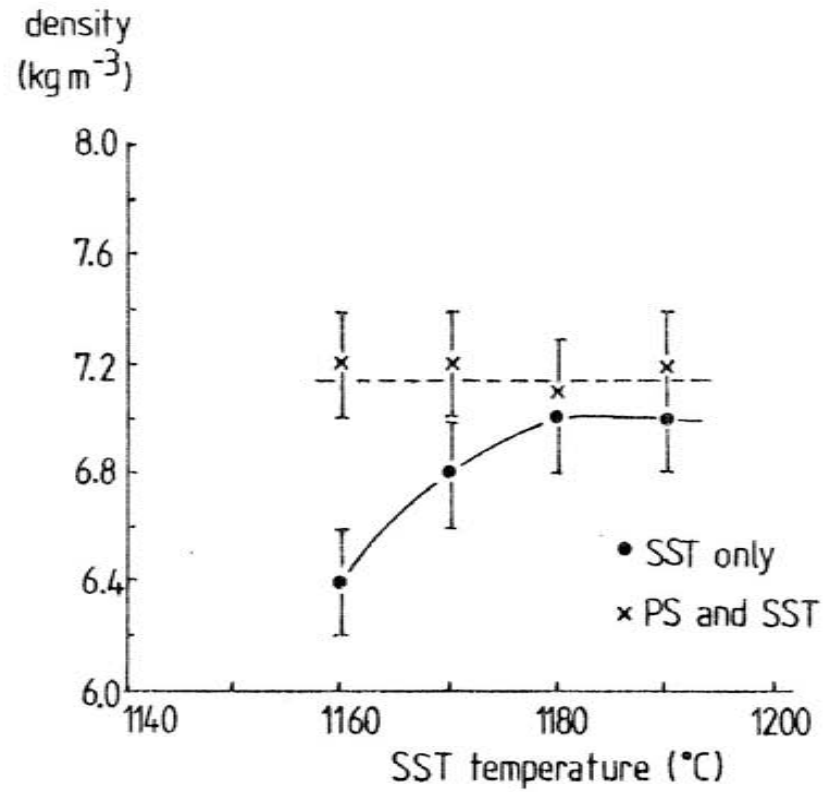

Fig. 7.28 Plots of density for PS at 1190°C and SST only HD samples.

The variations of the densities show a similar pattern to the ball milled only material. However, the specimens show lower density values through the S.S.T. range, which indicates that the size of the particles used in the green compact production stage were larger, so that densification is more difficult due to the larger pore size in the starting material.

7.6 Degassing Studies on the HD Material

The 2:17 alloy was hydrogen decrepitated (HD) at 200°C and 200 atm for about 12 hours.

The amount of hydrogen absorbed by the material was calculated from degassing studies, using the weight loss value after complete degassing had occurred. In addition, the temperature range at which the degassing occurs could also be found. The results are shown in fig. 7.29 as the weight loss versus temperature.

Using the value of the initial mass of HD material, the percentage weight loss was about 0.3%. The hydrogen begins to be released from the material at about 50°C, the process becomes more rapid at about 100°C and ends at about 350°C, the process is most rapid at about 150°C.

7.7 Microhardness Measurements on the Specimens aged at 800°C-900°C

The heat treatments given on the bulk and sintered specimens used for the microhardness measurements are detailed in section 6.9.3i. The results of the microhardness measurements for the bulk sample aged at 800°C and for the sintered samples aged in the range 800-900°C are shown in figs. 7.30 and 7.31 respectively.

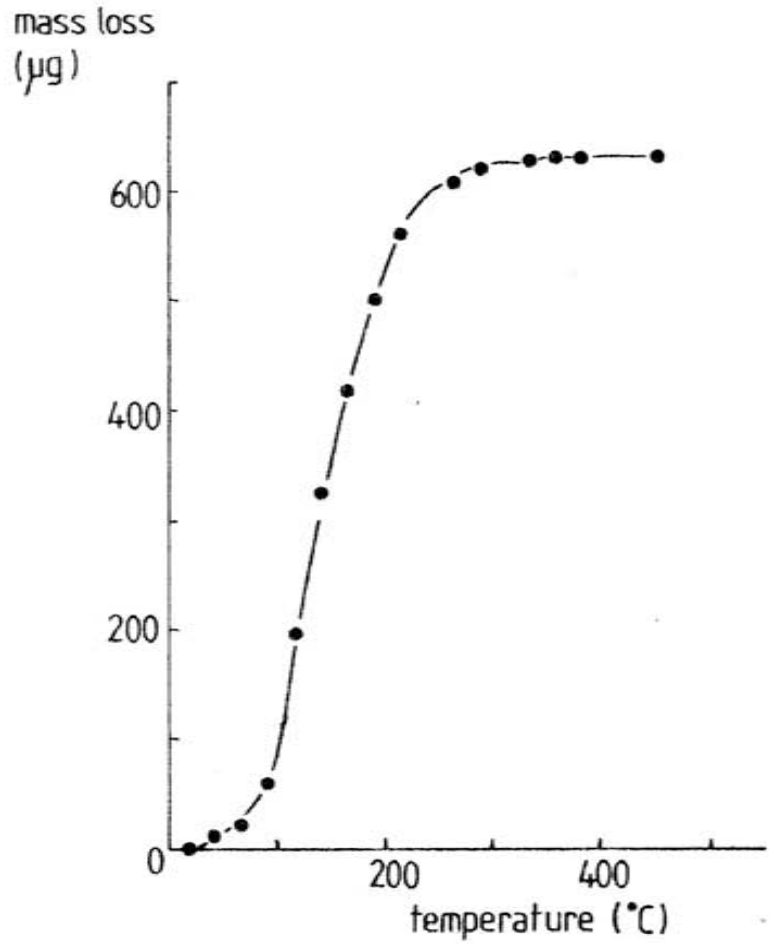

Fig. 7.29 Plot of mass loss versus degassing temperature for material hydrogenated at 200°C and 200 atm for about 12 hours.

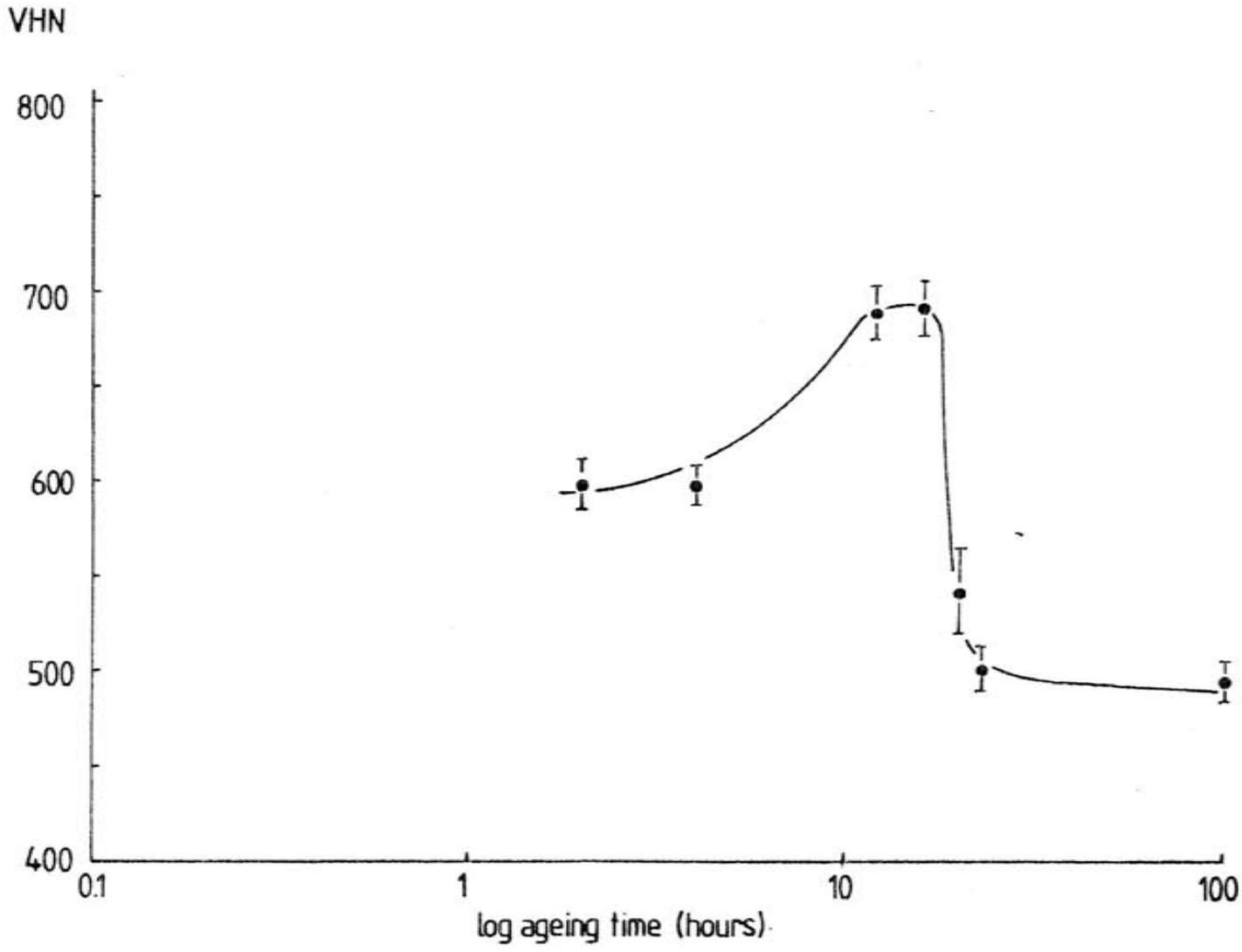

Fig. 7.30 Plot of microhardness (Vickers Hardness Number) versus log ageing time for a bulk sample SST at 1170°C and aged at 800°C. (VHN at 0 hours = 555 ± 12).

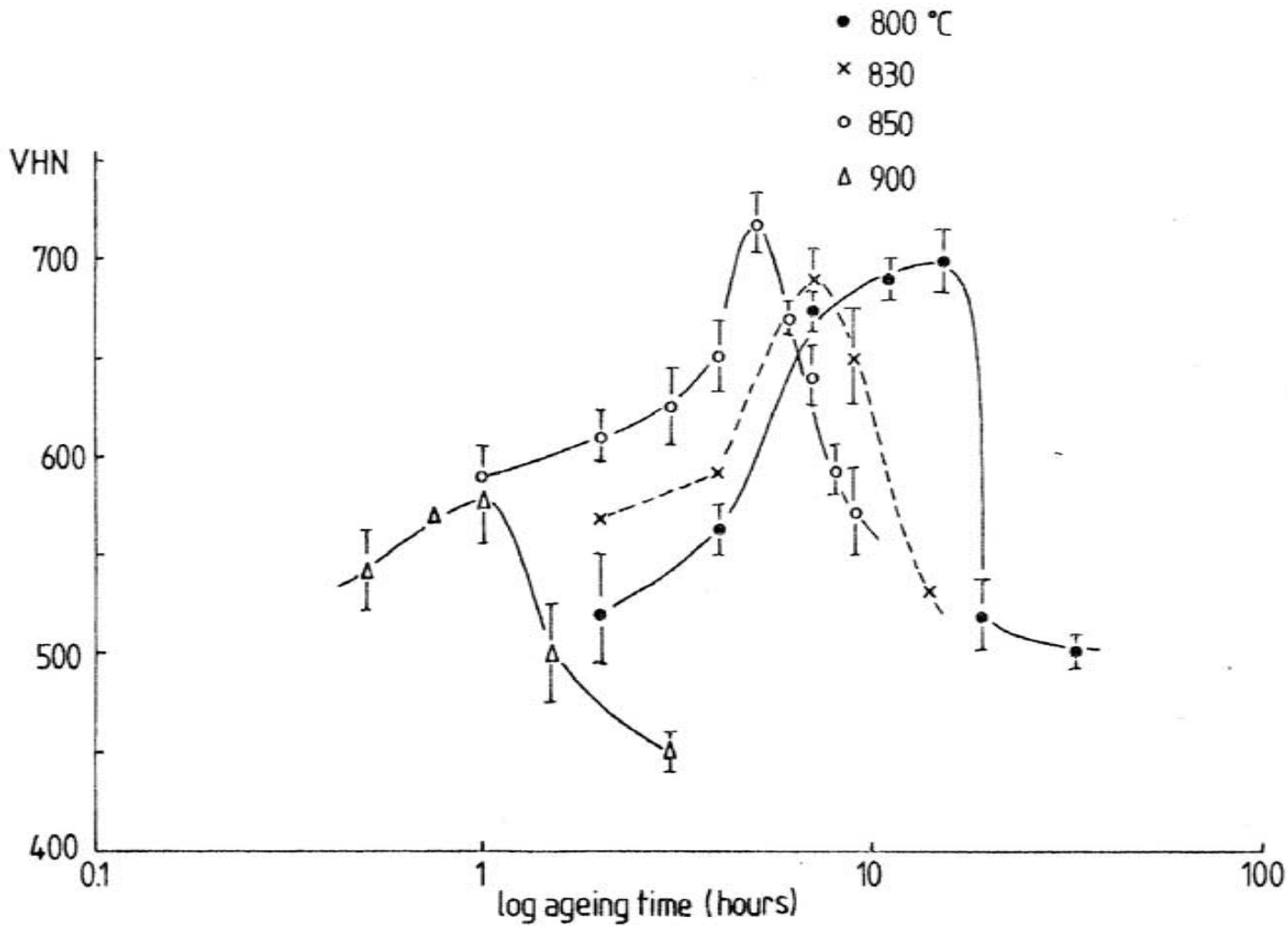

Fig. 7.31 Plots of microhardness versus log ageing time for sintered samples SST at 1170°C and aged at 800°C-900°C.

The values of microhardness versus log ageing time for the bulk sample aged at 800°C (fig. 7.30) show an increase up to an ageing time of about 15 hours, there is then a rapid fall and then the hardness values stabilize at about 25 hours. These results are similar to those achieved by Kianvash and Harris (ref. 96) for a similar alloy composition. They have shown that the ageing time corresponding to a peak in the microhardness values was about 26 hours and 38 hours for a 'z-value' of 7.55 and 8.92 respectively.

Thus, it would appear that as the 'z-value' decreases so does the ageing time required to reach a peak in the microhardness value.

The values of microhardness versus log ageing time for the sintered sample aged at 800°C (fig.7.31) show a similar plot to the bulk sample. At about 15 hours, there occurs a maximum hardness value, which is also followed by a rapid fall and the hardness then stabilizes after about 35 hours. The peak hardness value ageing time is the same as the ageing time required to reach a peak in the intrinsic coercivity (see fig. 7.16), and this is in excellent agreement with Kianvash and Harris (ref. 96). These results may be explained in terms of the pinning of domains by coherent precipitates which on ageing become incoherent. The fall in the microhardness value may be explained by the semi- and incoherent precipitates no longer pinning dislocations; this phenomenon occurs in a number of precipitation hardening systems (refs. 107,113).

As the ageing temperature increases, the ageing times required to reach the maximum microhardness decrease. The maximum hardness values for the ageing temperatures 800°C to 850°C are similar. However at an ageing temperature of 900°C there is a fall in the peak hardness value. These results are analogous to the variation of the intrinsic coercivity with ageing time at different ageing temperatures; the lower hardness

values observed in the sample aged at 900°C are possibly due to the rapid formation of incoherent precipitates which accompany the existing coherent precipitates. Alternatively, as discussed in Section 7.12, there is a subtle change in microstructure in the sample aged at 900°C.

7.8 Relative Electrical Resistivity Measurements on the Specimens Aged at 800°C-900°C

The heat treatments given on the bulk and sintered specimens used for the electrical resistivity measurements are detailed in Section 6.9.3i. The variation of the relative electrical resistivity, ρ/ρ_o as a function of log ageing time for the bulk specimen aged at 800°C is shown in fig. 7.32. The variations of ρ/ρ_o for the sintered samples aged at 800°C-900°C are shown in fig. 7.33.

The ρ/ρ_o values for the bulk sample (fig. 7.32) show a steady decrease up to an ageing time of about 15 hours, at this point there is an "elbow" in the plot and the subsequent ρ/ρ_o decrease is then very small.

The ρ/ρ_o values for the sintered specimen aged at 800°C (fig. 7.33) shows a similar variation when compared with the bulk sample. As the ageing temperature is increased, the "elbow" occurs at smaller ageing times. For the specimen aged at 900°C, there is a larger fall in the ρ/ρ_o values up to the "elbow" at an ageing time of about one hour. The difference in the resistance values for the sample aged at 900°C is also concurrent with lower values of $_iH_c$ and microhardness (figs. 7.16 and 7.31). This difference possibly arises from a change in the phases present during ageing. As discussed later in Section 7.12 and table 7.3 the sample aged at 900°C consists only of a matrix phase and a copper rich phase: the Zr rich phase is absent.

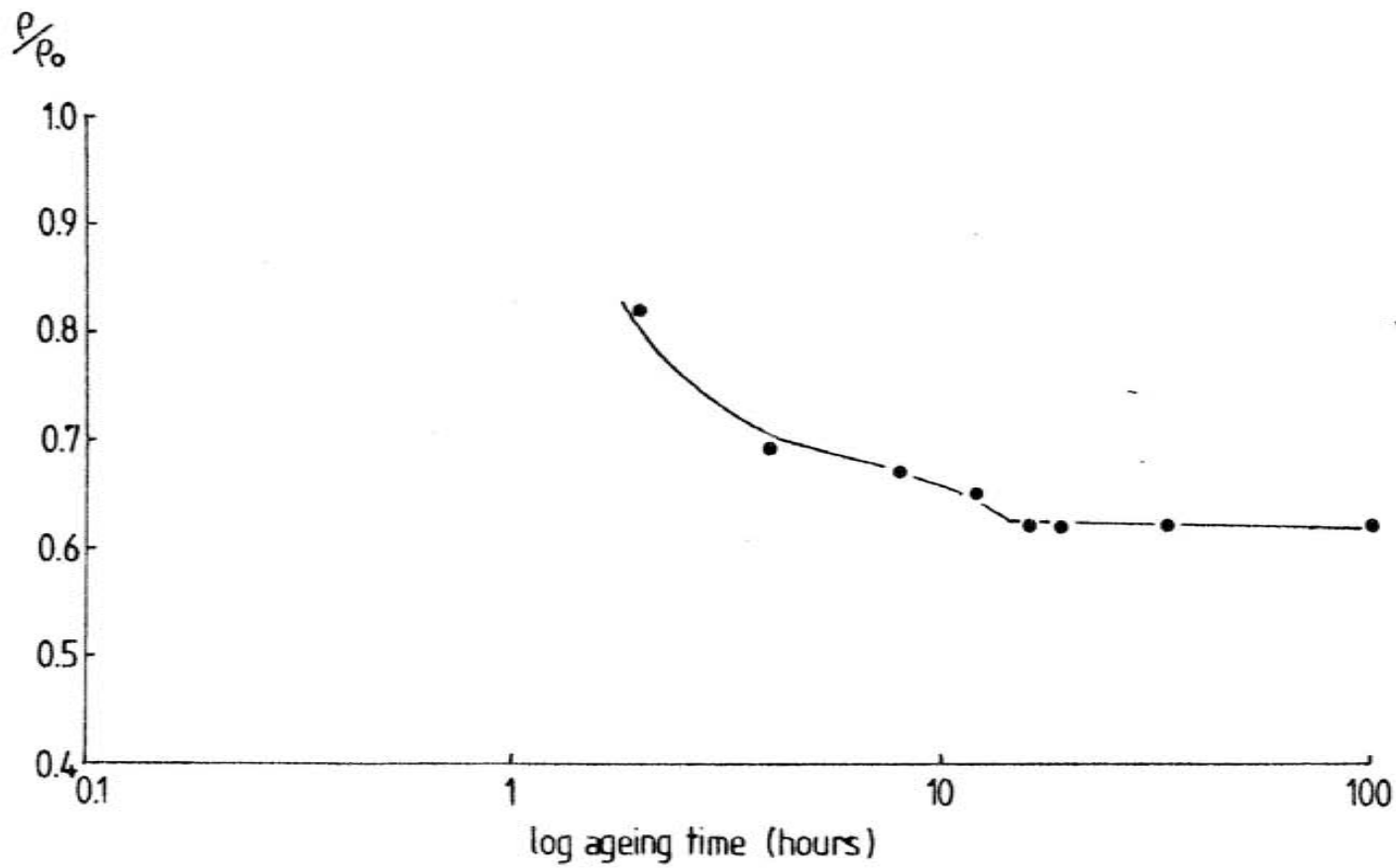

Fig. 7.32 Plots of relative electrical resistivity (ρ/ρ_o) versus log ageing time for bulk sample SST at 1170°C and aged at 800°C.

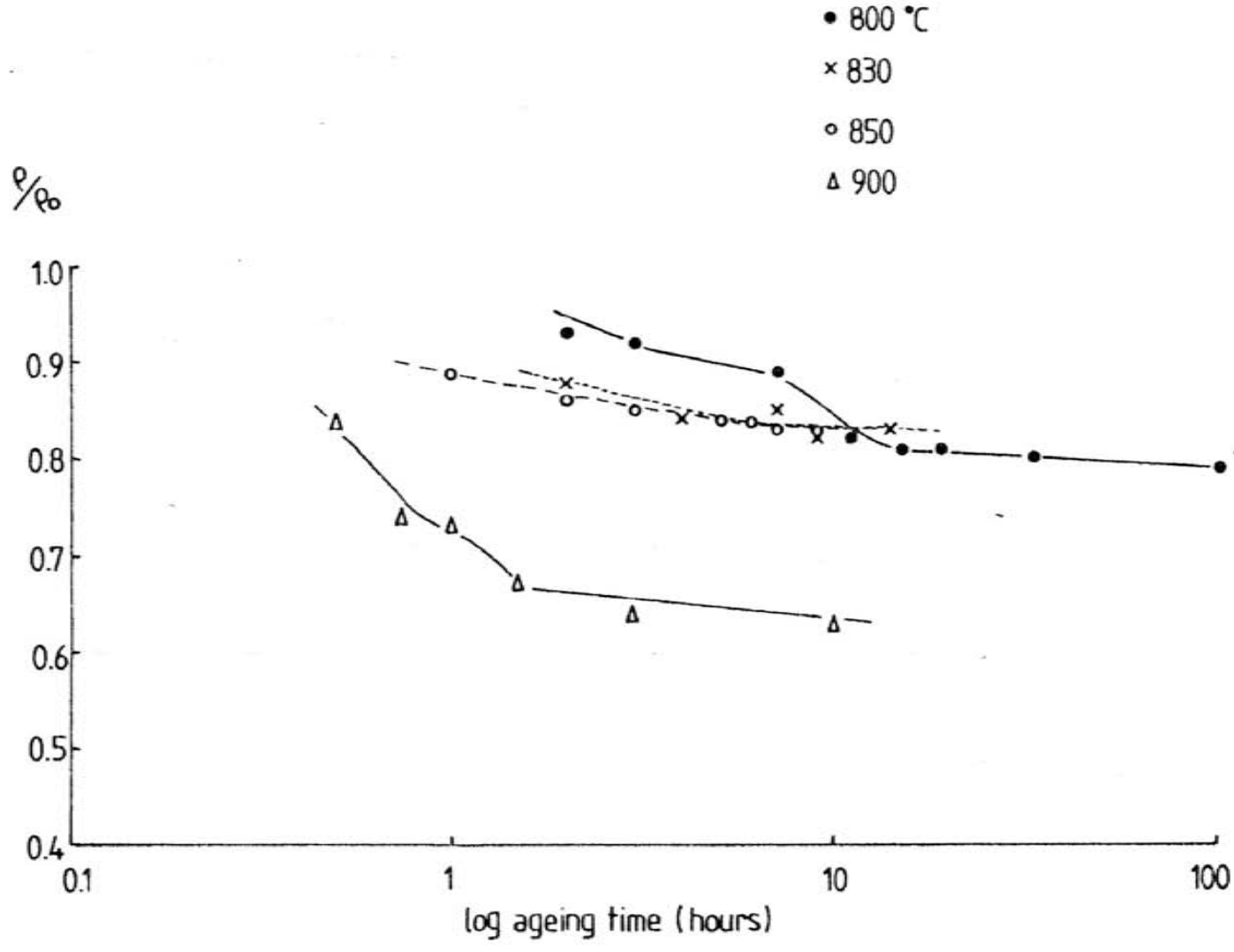

Fig. 7.33 Plots of relative electrical resistivity (ρ/ρ_o) versus log ageing time for sintered samples SST at 1170°C and aged at 800°C-900°C.

These results are all analagous to the results obtained for the peak $_iH_c$ values and the microhardness values, in terms of the change that occurs in the measured properties at the peak ageing time for the different ageing temperatures.

The fall in the relative electrical resistance with increasing ageing time may be explained in terms of the presence of the precipitates which form on ageing. Up to the ageing time at which the "elbow" occurs, the growth of the coherent precipitates reduces the electrical resistivity of the matrix. After the ageing time at which the "elbow" occurs is passed however, the formation of incoherent precipitates offsets this decrease due to a scattering of electrons at the incoherent boundaries between the matrix and the precipitates so that there is only a small fall in electrical resistivity with increasing ageing time. King and Glover (ref. 114) have observed a fall in electrical resistance with tempering time for Cr and Mo steels. This was proposedly due to the precipitation of a coherent carbide phase. Therefore the phenomenon observed in this investigation of a fall in resistivity with ageing time is not unknown, but it is unlike the situation normally observed in precipitation hardening systems, whereby the coherent precipitate formation is concurrent with a rise in electrical resistivity due to the scattering of electrons up to the ageing time at which the precipitates become semi- and incoherent (ref. 107).

7.9 A Calculation for the Activation Energy for Diffusion of the Coherent 1:5-type Precipitates in the $Sm(Co,Cu,Fe,Zr)_z$-type Alloys

For any nucleation and precipitation process as in the case of the 2:17-type alloys, there is an activation energy that is necessary for the precipitation process to start and to continue.

A standard Arrhenius equation may state that (ref. 115):

$$\text{rate of growth} = Ke^{-Q/RT} \tag{7.1}$$

therefore,

$$\log \text{rate} = \log K - \frac{Q}{RT} \tag{7.2}$$

K is a constant, Q is the activation energy for growth, R is the molar gas constant and T is the temperature.

The results obtained for the sintered specimens, have shown that as the ageing temperature increases, the intrinsic coercivity and microhardness have maximum values at lower ageing times which are identical for the two sets of measurements. In addition, an "elbow" occurs in the relative electrical resistivity values at ageing times identical to those at which the maximum values of ${}_iH_c$ and microhardness occur. Therefore it should be possible to obtain an activation energy for the precipitation and growth of the coherent 1:5-type phase in this alloy.

From equation 7.2, a plot of the reciprocal of the peak ageing time, which is analogous to the rate in sec^{-1} for the growth of coherent precipitates versus the reciprocal of the ageing temperature in degrees Kelvin, will yield a value for Q, the activation energy.

The values of ageing temperature, the peak microhardness and ${}_iH_c$ ageing time, one over the peak time, $\frac{1}{pt}$ (in $seconds^{-1}$), $\log_e \frac{1}{pt}$ and $\frac{1}{T}$ are listed in table 7.1b.

Table 7.1b

Ageing Temperature (^{o}K)	Peak Time (hours)	$\frac{1}{pt}$ (sec^{-1})	$\log_e \frac{1}{pt}$	$\frac{1}{T}$ (K^{-1})
1073	15	1.85×10^{-5}	-10.90	0.93×10^{-3}
1088	9	3.09×10^{-5}	-10.39	0.92×10^{-3}
1103	7	3.97×10^{-5}	-10.13	0.91×10^{-3}
1123	5	5.56×10^{-5}	-9.80	0.89×10^{-3}
1173	1	27.78×10^{-5}	-8.19	0.85×10^{-3}

The plot of $\log_e \frac{1}{pt}$ vs $\frac{1}{T}$ is shown in Fig. 7.34. From this graph, the activation energy Q can be calculated:

$$\text{gradient} = 3.11 \times 10^{4} = -\frac{Q}{R}$$

R is the molar gas constant = 8.314 $JK^{-1}\ mol^{-1}$

Therefore, Q = 259 $kJ\ mol^{-1}$. This value represents the energy required to initiate and maintain the precipitation of the coherent phase, and it is the correct order of magnitude for this type of process. By substituting in a value for K a standard equation can be written down for the precipitation in the $Sm(Co,Cu,Fe,Zr)_{7.4}$ alloy:

$$\text{rate of growth} = 2.16 \times 10^{-17}\ e^{\frac{3.11 \times 10^{4}}{T}} \qquad (7.3)$$

7.10 Optical Metallography of the Sintered Specimens

Due to the porous nature of the sintered samples, good quality optical micrographs were difficult to produce because of the uneven polishing of the individual particles making up the sintered compacts. Therefore, in this section some representative micrographs are shown, which give information

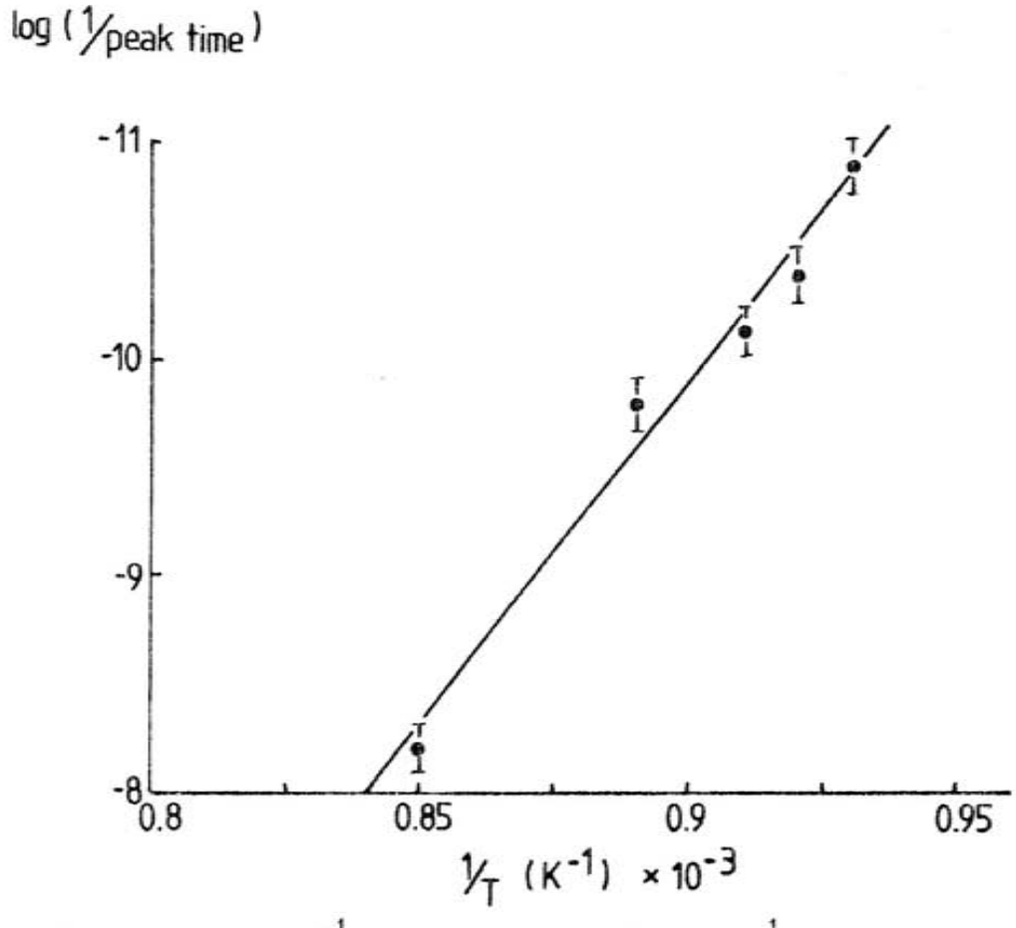

Fig. 7.34 Plot of log (^{1}/peak ageing time) versus ^{1}/T (T is the ageing temperature in degrees Kelvin). (Times are for peaks in microhardness and $_{i}H_{c}$).

about the density and particle sizes of the sintered specimens. More detailed SEM studies are given in the next section.

7.10.1 The Samples Produced from Ball Milled Only Material and Sintered at 1190°C and then S.S.T. at 1150°C-1190°C

The heat treatments given on these samples are detailed in section 6.5.3iA (specimens c and d).

7.10.1i The Specimen SST at 1170°C

The optical micrograph is shown in fig. 7.35 for the specimen sintered at 1190°C and then S.S.T. at 1170°C and aged at 800°C. The black areas are porosity which is quite sparce, indicating that the specimen has a high density. There is evidently some grain growth which is outlined by a dark grey phase, which is extensive in some grain boundary regions.

7.10.1i The Specimen S.S.T. at 1190°C

The optical micrograph is shown in fig. 7.36 for the specimen sintered at 1190°C and then S.S.T. at 1190°C and aged at 800°C. The black areas are porosity which are quite sparce, and similar to the specimen S.S.T. at 1170°C, which is expected as both specimens had the same sintering treatment at 1190°C. Some grain growth is also evident and the dark grey phase present at the grain boundaries is larger than in the sample S.S.T. at 1170°C. This agrees well with the magnetic properties which are rather

poor and indicative of a inhomogeneous phase distribution after ageing and/ or the presence of well developed incoherent precipitates.

7.10.2 The Samples Produced from HD Material and Sintered at 1190°C and then S.S.T. at 1150°C-1190°C

The heat treatments given on these samples are detailed in section 6.5.3iB (specimens c and d).

7.10.2i The Specimen S.S.T. at 1170°C

The optical micrograph is shown in Fig. 7.37. The black regions are porosity, which are larger than in the specimen produced from ball milled only material (see fig. 7.35). This would indicate that the starting material used in making the green compact consisted of a larger particle size. The higher amount of porosity also supports the lower density value of this specimen, compared with the specimen prdouced from BMO powder, (see figs. 7.27 and 7.28), and the lower remanence values.

Similar to the specimen in fig. 7.35, there is a distribution of a dark grey phase in the matrix, which is also associated with a light phase, that is elongated in one direction. The light phase is analagous to that observed in the "as cast" micrograph.

Both the specimens shown in figs. 7.35 and 7.37 were isothermally aged at 800°C for about 30 hours. The difference in the distribution of the dark grey phase is possibly related to the finer grains in the specimen produced from ball milled only material. The difference in the magnetic properties of the two specimens would appear to arise mainly from the difference in the density of the specimens, that is, a higher density (less porosity) gives a higher remanence value.

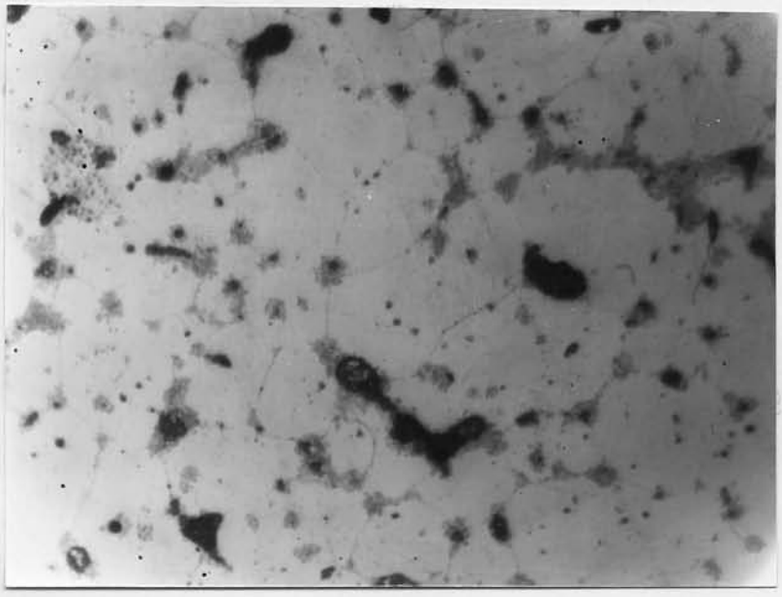

Fig. 7.35 Optical micrograph of BMO specimen sintered at 1190°C and then SST at 1170°C, quenched and then aged at 800°C for over 80 hours. (x 400).

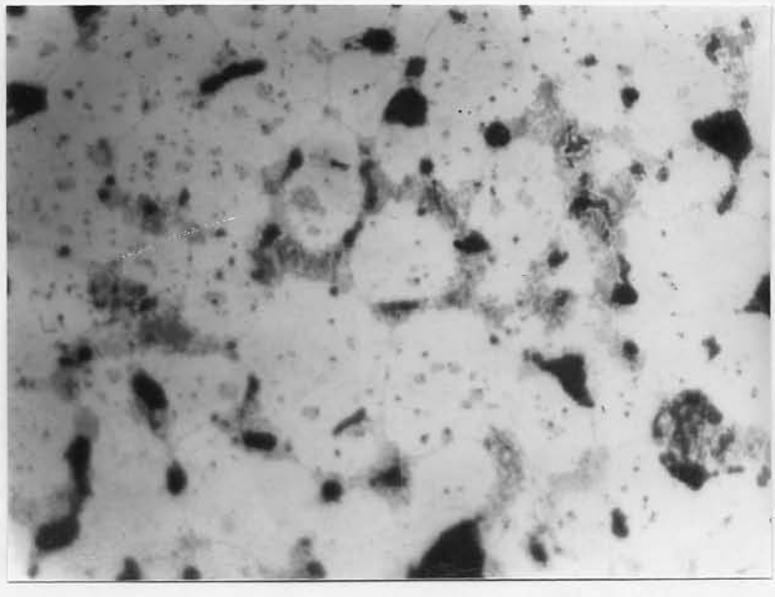

Fig. 7.36 Optical micrograph of BMO specimen sintered at 1190°C and then SST at 1190°C, quenched and then aged at 800°C for over 80 hours. (x 400).

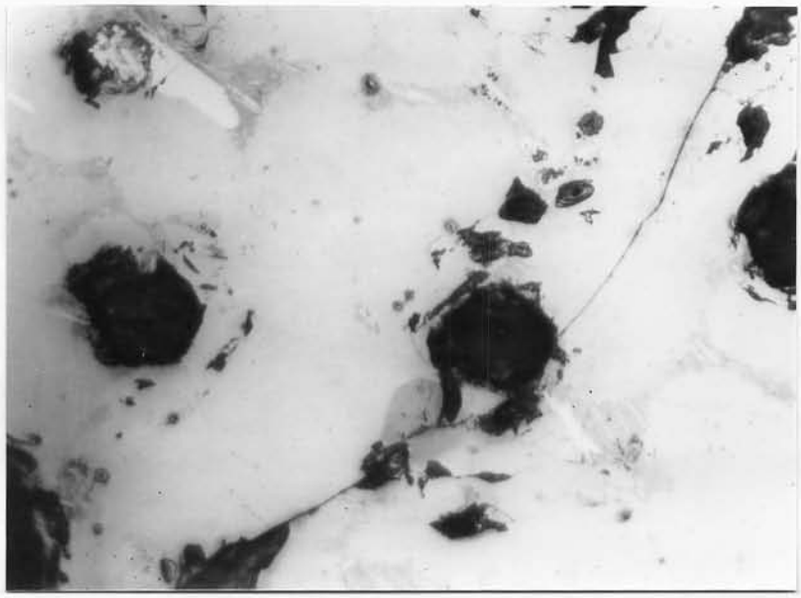

Fig. 7.37 Optical micrograph of HD specimen sintered at 1190°C and then SST and 1170°C, quenched and aged at 800°C for over 80 hours. (x 400).

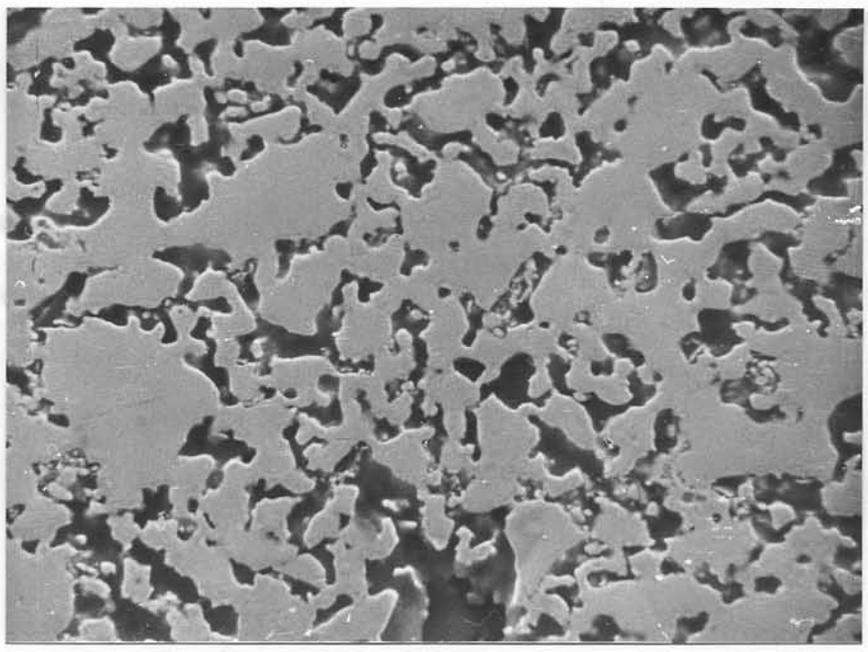

Fig. 7.38 Secondary SEM micrograph of specimen SST at 1150°C, quenched and aged at 800°C for over 80 hours. (x 640).

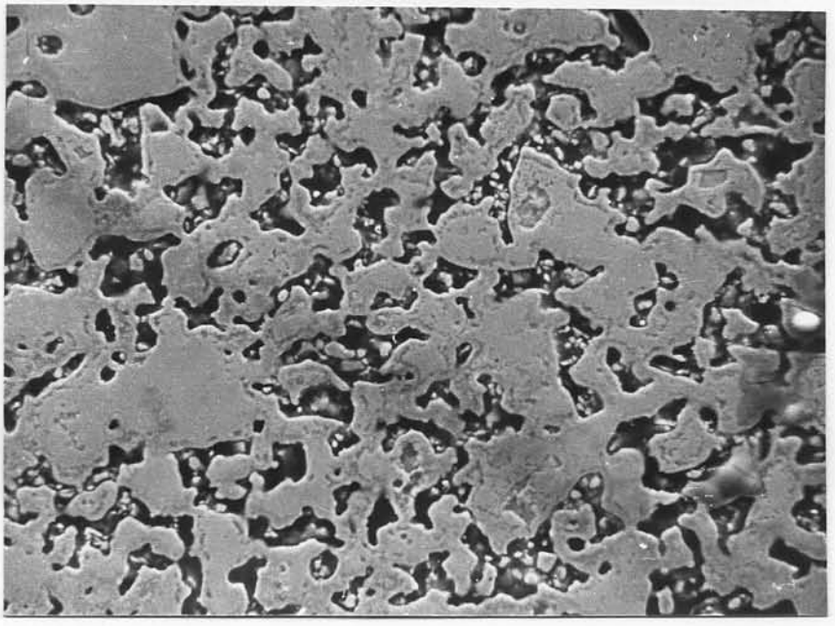

Fig. 7.39 Secondary SEM micrograph of specimen SST at 1160°C, quenched and aged at 800°C for over 80 hours. (x 640).

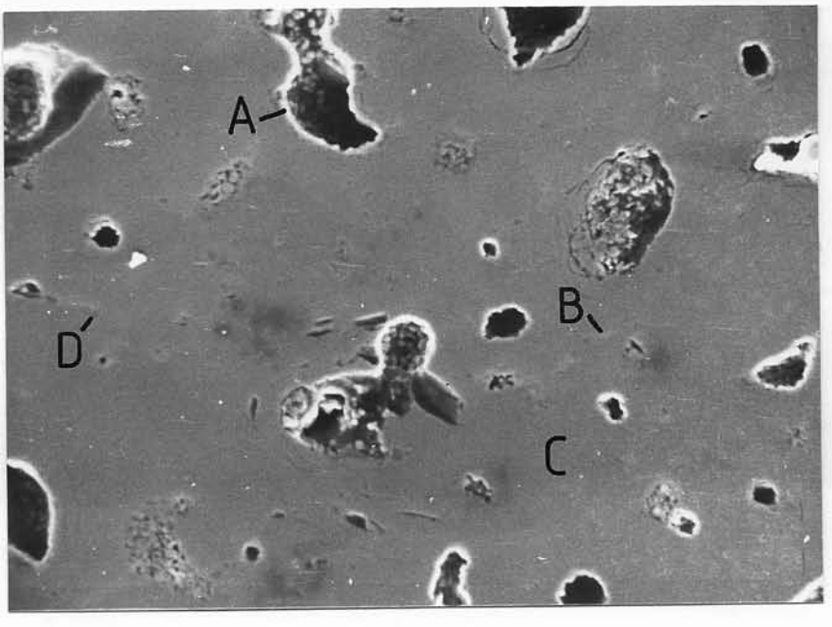

Fig. 7.40 Secondary SEM micrograph of specimen SST at 1170°C, quenched and aged at 800°C for over 80 hours. (x 640).

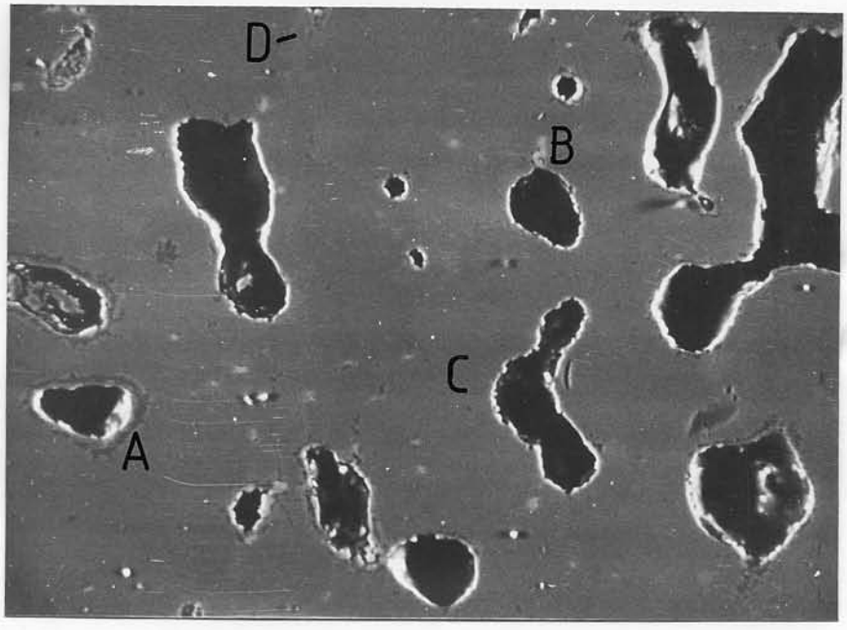

Fig. 7.41 Backscattered SEM micrograph of specimen SST at 1180°C, quenched and aged at 800°C for over 80 hours. (x 640).

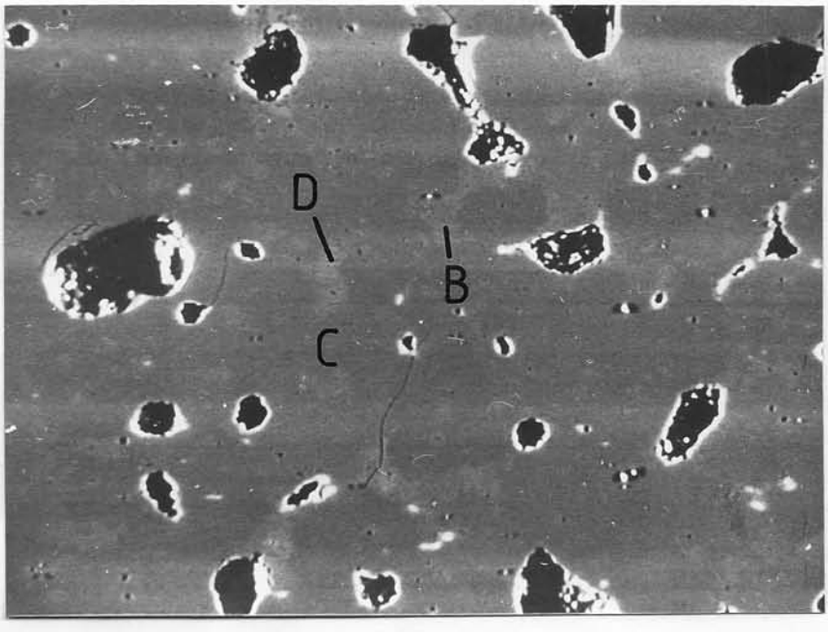

Fig. 7.42 Backscattered SEM micrograph of specimen SST at 1190°C, quenched and aged at 800°C for over 80 hours. (x 640).

grey phase (B) was a coherent 1:5-type phase, and the dark phase (D) was 2:17 hexagonal, thin platelets perpendicular to the c-axis.

The phases B, C and D were observed in the backscattered image of the sample S.S.T. at 1190°C (see fig. 7.42). The light phase (B) is more clearly seen and is distributed throughout the matrix phase, (C). The dark phase (D) is associated with the light phase and is slightly darker grey than the light phase (B) shown in fig. 7.42. The light regions around the pores is a topographical effect of the backscattered image.

7.11.2 The Samples Produced from Ball Milled Only Material and Pre-sintered at 1190°C and then S.S.T. at 1150°C-1190°C and then Aged at 800°C

The SEM micrographs of the samples that were sintered at 1190°C for one hour and then cooled to S.S.T. temperatures of 1150°C-1190°C and then quenched, and isothermally aged at 800°C are shown in figs. 7.43 to 7.46.

All the backscattered electron micrographs show the specimens to have approximately the same amount of porosity, which is expected since they were all sintered at 1190°C.

In the sample S.S.T. at 1150°C, three phases can be observed: a light phase (A); a dark phase (B) associated with the light phase and the matrix. The light regions are topographical effects.

In the sample S.S.T. at 1170°C, (shown in fig. 7.44), the same three phases were observed, but the light phase (A) appears more widely distributed and this may explain why the magnetic properties are rather lower

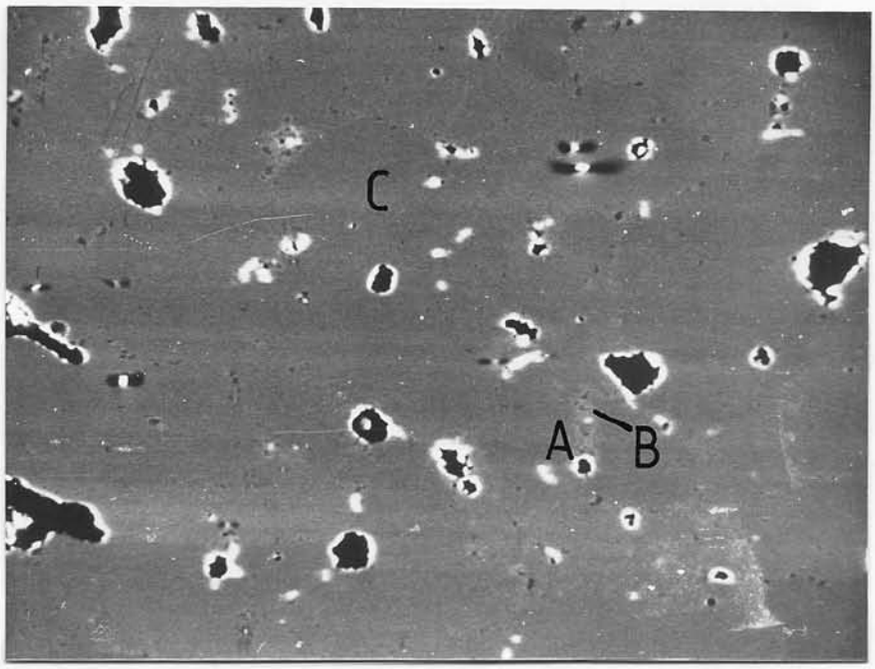

Fig. 7.43 Backscattered SEM micrograph of sample pre-sintered at 1190°C and then SST at 1150°C, quenched and aged at 800°C for over 80 hours. (x 640).

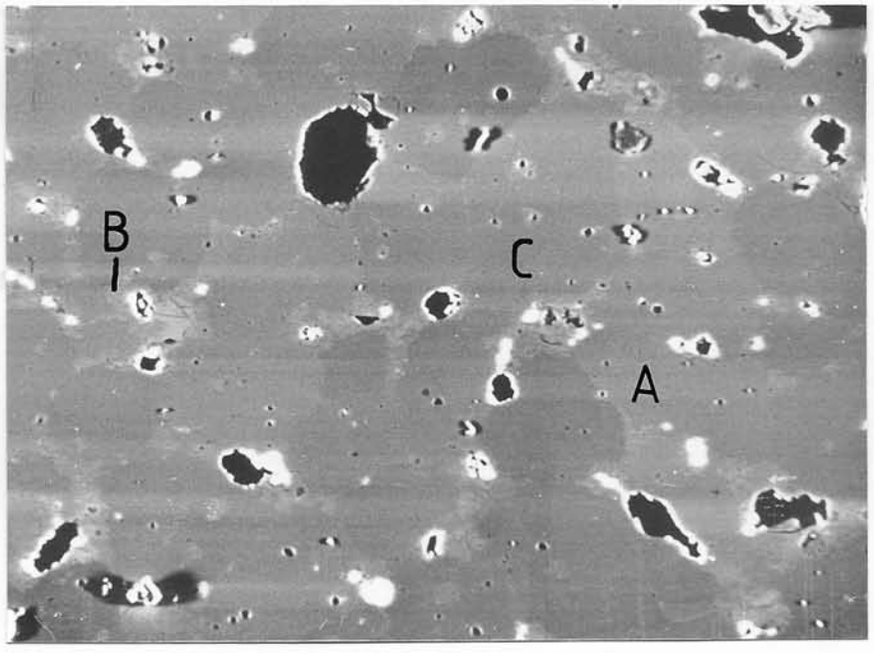

Fig. 7.44 Backscattered SEM micrograph of sample pre-sintered at 1190°C and then SST at 1170°C, quenched and aged at 800°C for over 80 hours. (x 640).

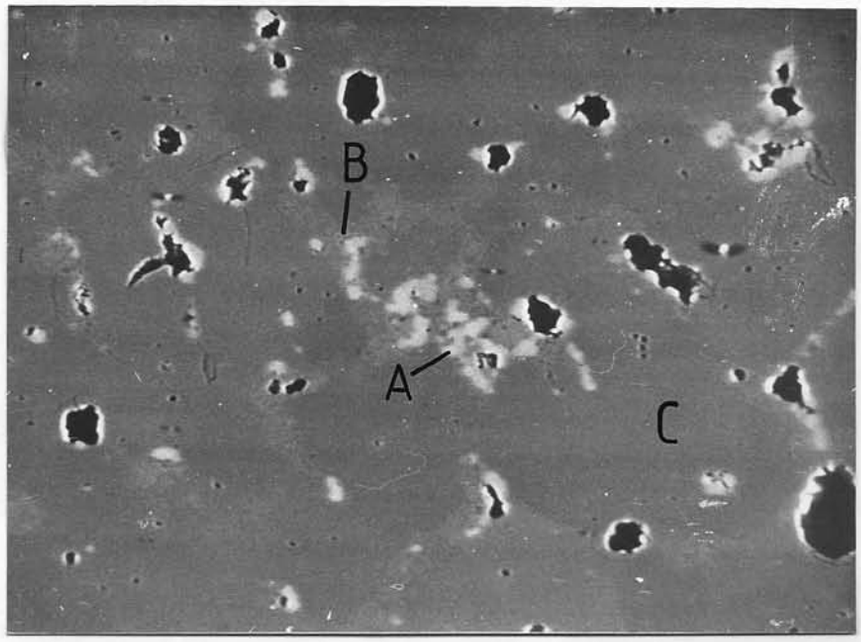

Fig. 7.45 Backscattered SEM micrograph of sample pre-sintered at 1190°C and then SST at 1180°C, quenched and aged at 800°C for over 80 hours. (x 640).

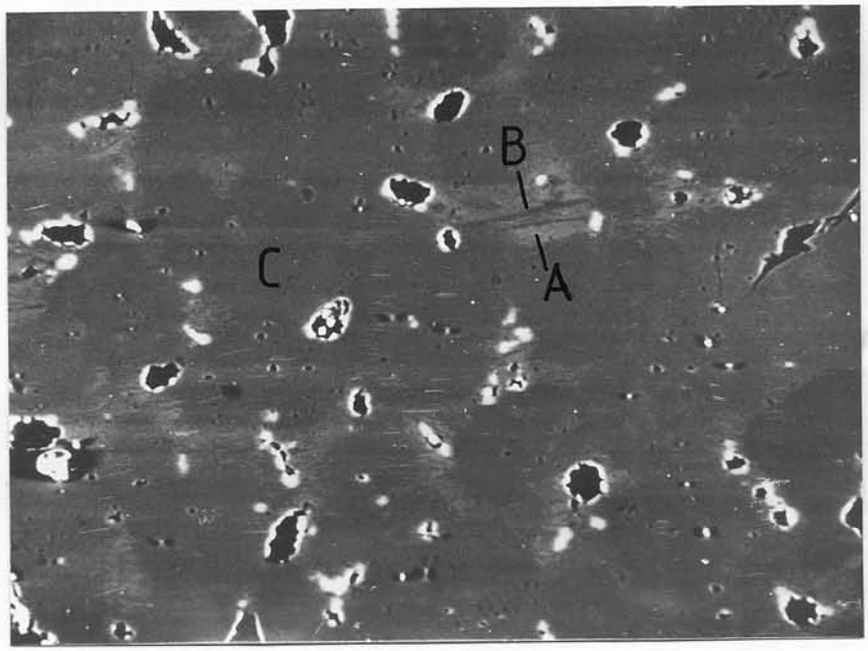

Fig. 7.46 Backscattered SEM micrograph of sample pre-sintered and S.S.T. at 1190°C, quenched and aged at 800°C for over 80 hours. (x 640).

than the sample S.S.T. at 1150°C. The light phase is a copper-rich phase (see X ray microanalysis results in next section), which is possibly incoherent in the sample S.S.T. at 1170°C, due to overageing so that the magnetic properties do not develop. This rapid transformation from coherent to incoherent precipitates may be a result of the S.S.T. temperature being too high to allow any homogenisation of the microstructure before ageing.

This tentative explanation is supported by the observation of the light phase in the sample S.S.T. at 1180°C (see fig. 7.45). The light phase (A), in the backscattered micrograph is lighter in some regions, suggesting an inhomogeneous microstructure after quenching from the S.S.T. temperature. This is illustrated further by the backscattered micrograph of the sample S.S.T. at 1190°C in fig. 7.46. In this specimen, the dark phase (B) is larger than in the other samples and more clearly defined, it is also associated with the light phase (A) which is distributed throughout the matrix (C).

7.11.3 The Samples Produced from HD Material and then Ball Milled and S.S.T. at 1150°C-1190°C and aged at 800°C

The SEM secondary electron micrographs of two specimens S.S.T. at 1170°C and 1190°C are shown in figs. 7.47 and 7.48 respectively. It can be seen that there is a large amount of porosity in these samples and this is supported by the low density values (see fig. 7.28). The sample S.S.T. at 1170°C (fig. 7.47) also has intergranular cracks (A). This is attributed to the hydrogenation process which produces very friable particles (ref. 103).

The densification of the HD specimens on S.S.T. is illustrated in fig. 7.48 for the sample S.S.T. at 1190°C. The small amounts of porosity have been removed and less numerous, large pores have resulted.

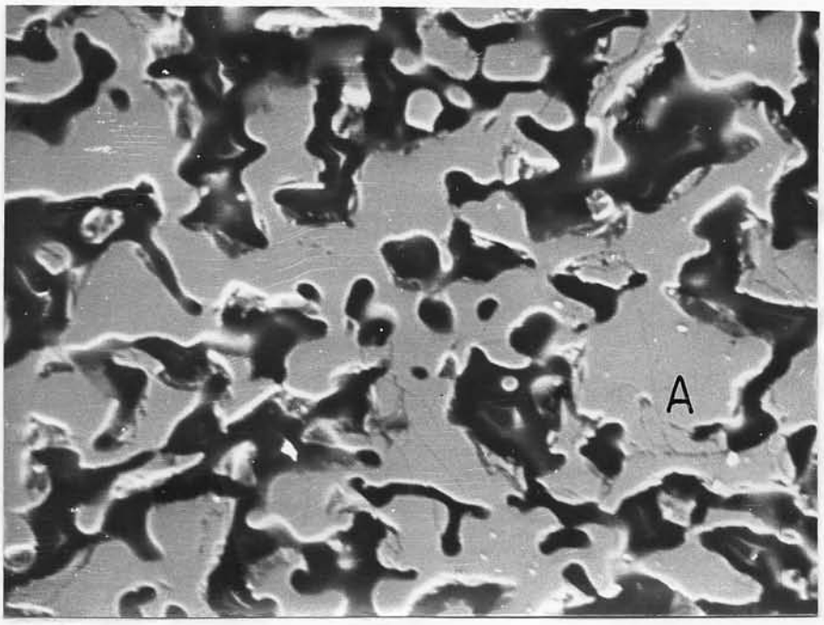

Fig. 7.47 Secondary SEM micrograph of HD sample SST at 1170°C, quenched and aged at 800°C for over 80 hours. (x 640).

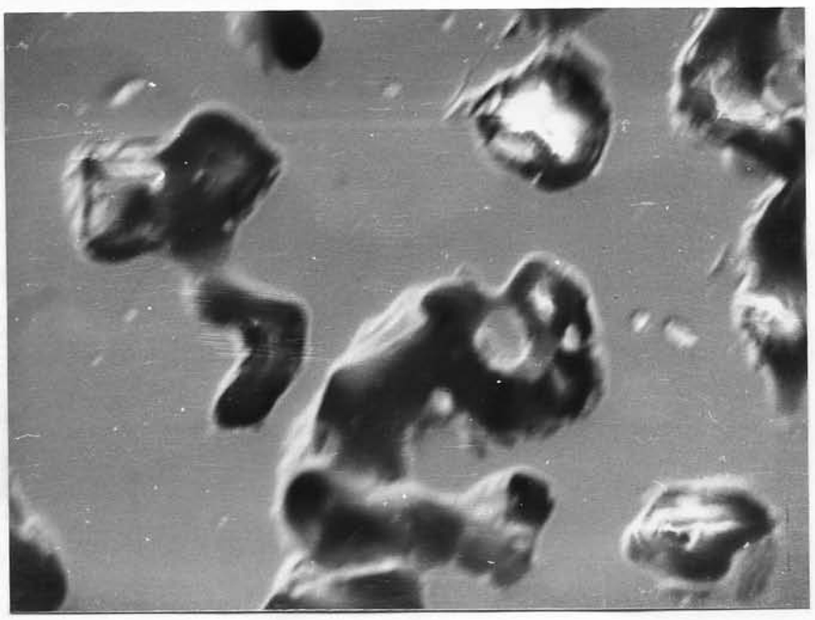

Fig. 7.48 Secondary SEM micrograph of HD sample SST at 1190°C, quenched and aged at 800°C for over 80 hours. (x 640).

7.12 X-ray Microanalyses of the Sintered Specimens

The X-ray microanalysis studies were undertaken to look at any chemical changes on the phases present in the microstructures. The results are discussed individually, and related to some of the SEM micrographs in figures 7.40 to 7.48.

7.12.1 Results of X-ray Microanalysis (EDAX) Studies on the Samples S.S.T. at 1150°C to 1200°C

The results of the EDAX studies for the samples S.S.T. at 1170°C, 1180°C and 1190°C are given in table 7.2. The described phases are related to the phases observed in figures 7.40, 7.41 and 7.42 respectively. The results are given as substitution compositions. Note that all the samples had been aged at 800°C for over 30 hours and were in an overaged condition.

The pore phase observed in the samples S.S.T. at 1170°C and 1180°C ((A) in fig. 7.41) is richer in Sm than the other phases (see table 7.2). This is possibly due to the melting of the material at the pores or solid solution treatment, or, due to the fact that the S.S.T. temperature did not remove all the homogeneities: this is supported by the fact that the pore phase is very sparsely distributed and does not occur at all the pores.

The other three phases observed have compositions that agree well with those discussed for the bulk specimen in section 7.2.2. The matrix phase is Co and Fe rich; the dark phase is Zr rich but not as depleted in Sm as the bulk sample and the light phase is Cu and Sm rich.

Table 7.2

EDAX studies of the Samples S.S.T. at 1170°C, 1180°C and 1190°C

Sample Treatment	Area details	Substitution Composition (± 0.03-0.05)
S.S.T. 1170°C, age 800°C 30 hours	Pore Phase (A)	$Sm(Co_{0.52}Cu_{0.001}Fe_{0.34}Zr_{0.01})_{4.69}$
" "	Light Phase (B)	$Sm(Co_{0.48}Cu_{0.38}Fe_{0.12}Zr_{0.03})_{6.43}$
" "	Matrix (C)	$Sm(Co_{0.72}Cu_{0.07}Fe_{0.19}Zr_{0.02})_{8.07}$
" "	Dark Phase (D)	$Sm(Co_{0.61}Cu_{0.06}Fe_{0.32}Zr_{0.01})_{26.7}$
	(see Fig. 7.40)	
S.S.T. 1180°C, age 800°C 30 hours	Pore Phase (A)	$Sm(Co_{0.64}Cu_{0.01}Fe_{0.35}Zr_{0.01})_{2.66}$
" "	Light Phase (B)	$Sm(Co_{0.45}Cu_{0.47}Fe_{0.08}Zr_{0.0004})_{5.09}$
" "	Matrix (C)	$Sm(Co_{0.69}Cu_{0.08}Fe_{0.22}Zr_{0.02})_{8.3}$
" "	Dark Phase (D)	$Sm(Co_{0.42}Cu_{0.16}Fe_{0.15}Zr_{0.13})_{4.44}$
	(see Fig. 7.41)	
S.S.T. 1190°C, age 800°C 30 hours	Light Phase (B)	$Sm(Co_{0.5}Cu_{0.37}Fe_{0.12}Zr_{0.01})_{5.62}$
" "	Matrix (C)	$Sm(Co_{0.63}Cu_{0.07}Fe_{0.23}Zr_{0.01})_{8.9}$
" "	Dark Phase (D)	$Sm(Co_{0.41}Cu_{0.49}Fe_{0.1}Zr_{0.005})_{7.1}$
" "	(see Fig. 7.42).	

With increasing S.S.T. temperature, the matrix phase is richer in Cu and the light phase is poorer in Cu. This is important in discussing the magnetic properties: at the optimum S.S.T. temperature the proportion of Cu in the light phase (the "1:5"-type phase) is at an optimum to give the highest coercivity. The amount of Zr in the dark phase varies to a large extent for the different SST temperatures. Only in the sample S.S.T. at 1180°C is the dark phase (D) evidently Zr rich and this observation is possibly concurrent with 1180°C being the optimum S.S.T. temperature. The composition of the dark phase in the sample S.S.T. at 1170°C and aged at 800°C is $Sm(Co_{0.61}Cu_{0.06}Fe_{0.32}Zr_{0.01})_{26.7}$ the compositions of the dark phases in the other two samples in table 7.2 are richer in Sm. This is an anomalous result due possibly to oxidation of Sm giving an apparent Sm poor phase.

For the samples pre-sintered at 1190°C and then S.S.T. at 1150°C-1190°C, the same phases were observed with a similar difference in the phase compositions and similar element concentrations in the phases. This is also true for the samples produced from HD powder.

7.12.2 Results of X-ray Microanalysis (EDAX) Studies on the Samples S.S.T. at 1170°C and then aged at 800°C-900°C

The results of the EDAX studies for the samples S.S.T. at 1170°C and then aged at 800°C, 830°C, 850°C and 900°C are shown in table 7.3. The sample aged at 800°C has been discussed in the previous section.

The EDAX studies show that the ageing temperature has little affect on the concentration of the elements in the matrix phase, however as the magnetic properties do change with increasing ageing temperature, then

Table 7.3

EDAX studies of the samples S.S.T. at 1170°C and then aged at 800°C-900°C

Sample Treatment	Area Details	Substitution Composition ($\pm$ 0.03-0.05)
S.S.T. 1170°C, age 800°C, 30 hours	Dark Phase	$Sm(Co_{0.61}Cu_{0.06}Fe_{0.32}Zr_{0.01})_{26.7}$
	Light Phase	$Sm(Co_{0.48}Cu_{0.38}Fe_{0.12}Zr_{0.03})_{6.43}$
	Matrix	$Sm(Co_{0.72}Cu_{0.07}Fe_{0.19}Zr_{0.02})_{8.07}$
S.S.T. 1170°C, age 830 C, 14 hours	Dark Phase	$Sm(Co_{0.43}Cu_{0.3}Fe_{0.12}Zr_{0.15})_{5.1}$
	Light Phase	$Sm(Co_{0.61}Cu_{0.12}Fe_{0.26}Zr_{0.01})_{6.32}$
	Matrix	$Sm(Co_{0.67}Cu_{0.07}Fe_{0.24}Zr_{0.02})_{8.39}$
S.S.T. 1170°C, age 850°c, 9 hours	Dark Phase	$Sm(Co_{0.5}Cu_{0.1}Fe_{0.17}Zr_{0.23})_{8.14}$
	Light Phase	$Sm(Co_{0.64}Cu_{0.14}Fe_{0.19}Zr_{0.03})_{7.11}$
	Matrix	$Sm(Co_{0.63}Cu_{0.14}Fe_{0.21}Zr_{0.02})_{6.93}$
S.S.T. 1170°C, age 900°C, 3 hours	Light Phase	$Sm(Co_{0.67}Cu_{0.09}Fe_{0.22}Zr_{0.02})_{8.15}$
	Matrix	$Sm(Co_{0.67}Cu_{0.09}Fe_{0.23}Zr_{0.02})_{8.0}$

there must be a more subtle phase effect occurring. The composition of the light phase is Cu and Sm rich through all the ageing temperatures. This phase has the richest Cu content at the ageing temperature of 800°C, but the ageing time for this specimen was over 30 hours. The other specimens were aged for much shorter times than this so the diffusion of Cu into the light phase may not be fully complete even though all the samples were in the overaged condition in terms of the magnetic properties.

The samples aged at 800°C, 830°C and 850°C all showed a similar peak value of intrinsic coercivity, but at lower ageing times with increasing ageing temperature. The sample aged at 900°C however, did not show any large development of the magnetic properties and referring to table 7.3, it can be seen that there is an absence of the dark phase observed in the other samples. Thus, the anomally in the variation of the magnetic properties for the sample aged at 900°C, seems to arise from the absence of the dark phase. Ray (ref. 104) has observed that on isothermal ageing, Zr is rejected by the 2:17 rhombohedral matrix to increase its degree of magnetic order and a Zr-rich 2:17 hexagonal phase forms. Thus at an ageing temperature of 900°C, it is possible that the Zr is retained in the 2:17 matrix due to an increased solubility at the higher temperatures and the magnetic properties are consequently poorer.

It has also been noted (ref. 104) that as the ageing temperature increases, the cellular microstructure increases, so that the 1:5 coherent precipitates are distributed on a less fine scale so that there is less affective pinning of domain walls, so that the intrinsic coercivity does not develop on ageing, which has been observed in this investigation.

7.13 Summary

The results discussed in the previous section can be briefly summarised as follows (a more detailed summary is given in the next chapter):

1. The bulk sample in the "as cast" form consists of three phases:
   a) a matrix phase (Co, Fe rich)
   b) a light phase (Sm, Cu rich)
   c) a dark phase (Zr rich and Sm depleted).

These phases occur also in the heat treated bulk alloy in differing proportions.

2. The BMO powder had the smallest particle size while the HD material had a larger particle size which subsequently affected the magnetic properties. The best magnetic properties occurring for the BMO material.

3. The optimum S.S.T. temperature was found to be 1180°C. If the samples were pre-sintered at 1190°C the optimum S.S.T. temperature was about 1150°C to 1160°C due to the more rapid phase transformation times at this temperature.

4. The ageing times required to attain the optimum magnetic properties varied with S.S.T. temperature due to the inhomogeneities present in the microstructures after quenching from the S.S.T. temperature.

5. The $_iH_c$, microhardness and electrical resistance variations with log ageing time for the samples aged at 800°C-900°C showed similar variations. However, the peak ageing times decreased with increasing ageing temperature. The sample aged at 900°C exhibited much lower values and this was attributed to the absence of a Zr-rich phase which was present in all the other aged samples.

6. Except for the sample aged at 900°C, three phases were observed in the sintered specimens:

a) a matrix phase (Co, Fe rich)

b) a light phase (Sm, Cu rich)

c) a dark phase (Zr-rich but not Sm depleted)

d) a Sm-rich "pore phase" arising from the presence of a liquid phase on S.S.T. This phase was not present at all the pores.